



**Politecnico
di Torino**



**MEDICAL UNIVERSITY
OF VIENNA**

Politecnico di Torino

Master's Degree in Mechanical Engineering

Department of Mechanical and Aerospace Engineering

**Characterization of Metal FDM process and
final mechanical performances evaluation**

Supervisors:

prof. Giorgio De Pasquale
prof. Francesco Moscato

Candidate:

Ferdinando Ursi S290596

Academic Year 2022/2023

Table of Contents

Abstract	4
Abbreviations	6
1. Introduction	9
2. Metal additive manufacturing (MAM)	15
2.1. Types of processes	15
2.1.1. Powder Bed Fusion	15
2.1.2. Direct Energy Deposition	17
2.1.3. Extrusion Additive Manufacturing	19
2.1.4. Binder Jetting	20
2.1.5. Laminated Object Manufacturing	21
2.2. Materials for MAM	21
2.2.1. Titanium Alloys	21
2.2.2. Aluminium Alloys	22
2.2.3. Iron- and Nickel- Based Alloys	22
2.3. Applications	22
2.3.1. Aerospace Industry	23
2.3.2. Automotive Industry	23
2.3.3. Tooling Industry	23
2.3.4. Healthcare Industry	24
2.3.5. Nanomanufacturing	24
3. Metal FDM	25
3.1. Process stages	25
3.1.1. Feedstock manufacturing	25
3.1.2. Shaping stage	31
3.1.3. Debinding stage	34
3.1.4. Sintering stage	37
3.2. History of the technology	38
3.3. Benefits	39
3.4. Drawbacks	39
4. Equipment and materials	41
4.1. Filaments	41

4.1.1.	<i>Acrylester-Styrol-Acrylnitril (ASA)</i>	41
4.1.2.	<i>ULTRAFUSE 316L</i>	42
4.1.3.	<i>Titanium 64-5 Filamet™</i>	43
4.1.4.	<i>High-Impact Polystyrene (HIPS)</i>	44
4.2.	Solvent agent	44
4.3.	Filament pre-heater	45
4.4.	Metal FDM printer	46
4.5.	Slicer software	48
4.6.	Tensile test machine	49
4.7.	CAD Software	50
4.8.	Measurement instruments	50
4.8.1.	<i>Calliper</i>	50
4.8.2.	<i>Micrometer</i>	51
4.8.3.	<i>Microscope</i>	51
4.9.	SLM printer	51
5.	Methods	54
5.1.	Preliminary activity	54
5.1.1.	<i>Mono-extrusion polymer practice</i>	54
5.1.2.	<i>Double-extrusion polymer practice</i>	56
5.1.3.	<i>Double-extrusion metal feedstock practice</i>	64
5.2.	Tensile test specimen design	66
5.2.1.	<i>Tensile test standard references</i>	67
5.2.2.	<i>Gripping area design</i>	68
5.2.3.	<i>Debinding shrinkage compensation</i>	69
5.2.4.	<i>Identification system</i>	70
5.2.5.	<i>Design of experiment</i>	72
5.2.6.	<i>Manufacture</i>	72
5.3.	Shrinkage sample	88
5.3.1.	<i>Shape of the sample</i>	88
5.3.2.	<i>Orientation and identification system</i>	89
5.3.3.	<i>Manufacture</i>	90
5.4.	Challenges encountered in the study	104
5.4.1.	<i>Adhesion of the first layer</i>	104
5.4.2.	<i>Print exposure to the solvent agent</i>	106
5.4.3.	<i>Pressure of the nozzle</i>	107
5.4.4.	<i>Equalization of nozzles position</i>	108

6. Economic characterization with a cost model.....	110
6.1. Cost of the material exploited in the deposition process	110
6.2. Cost due to the energy consumption	113
6.3. Cost of the solvent.....	115
6.4. Cost of the debinding and sintering process.....	116
7. Results.....	118
7.1. Dimensional characterization.....	118
7.1.1. <i>ULTRAFUSE 316L green part tensile test specimens</i>	118
7.1.2. <i>Filamet 64-5 green part shrinkage specimens</i>	120
7.2. Mechanical characterization	120
7.2.1. <i>Ti6Al4V (L-PBF) tensile test results</i>	120
7.3. Physical characterization	121
7.3.1. <i>Electrical characterization</i>	121
7.3.2. <i>Magnetic characterization</i>.....	121
7.4. Economic characterization	122
7.4.1. <i>Titanium 64-5 Filamet specimens</i>.....	122
7.4.2. <i>ULTRAFUSE 316L specimens</i>	123
8. Discussion	124
9. Conclusions	126
Appendix A - Statistical instruments	128
Arithmetic Mean Value.....	128
Standard Deviation of the Sample	128
Coefficient of Determination R^2	129
List of Tables.....	135
Bibliography.....	136
Aknowledgements.....	141

Abstract

Over the years, the Additive Manufacturing (AM) technologies are gaining more and more interest in the industrial and research field. So far, the Laser Powder Bed Fusion (L-PBF) technology is the most popular Metal Additive Manufacturing (MAM) technology.

Compared with the other MAM processes, the L-PBF process allows to achieve the best mechanical performances. However, the process results highly energy-consuming and require special safety devices when operating e.g., Titanium alloys or Aluminium alloys. In some cases, the costs associated with the process penalize other advantages. This makes L-PBF an out-of-price solution in certain fields, such as the manufacture of titanium medical implants.

An emerging alternative is the Metal Fused Deposition Modeling (Metal-FDM). This technology is an AM technology that has recently been worthy of interest. In the medical field, for example, researchers were able to print a maxillofacial implant.

In literature, studies about the printing of the titanium with the Metal FDM often use tailored materials, or “feedstock”. This trend makes it difficult to reproduce experiments and compare the results reported in those studies. Differently from other studies, in our case the Ti6Al4V filament feedstock will be externally purchased.

In this study, a detailed description of all stages of the Metal FDM is provided to help the reader to get familiar with the benefits and limits of this process. The aim of the study is the exploration of the printing parameters that play the most relevant roles in the success of the print and tackle the technical issues of the process. In response of the lack of knowledge about the debinding and sintering (D&S) processes of the Ti6Al4 feedstock, an assessment of shrinkage rate associated to the D&S of a commercial feedstock. In the end, the economic impact of the print is evaluated.

Given the lack of titanium feedstock, a preliminary activity was included to become familiar with the printer saving expensive material. During this activity some tensile specimens were printed with the ULTRAFUSE 316L, a steel feedstock.

Problems regarding the adhesion of the first layer, the manual bed calibration, the manual calibration of a double-extrusion were experienced and solved. The qualitative evaluation carried out about the conductivity and magnetic properties evaluation paves the way to alternative applications and studies. The shrinkage and the mechanical properties of the ULTRAFUSE 316L are not available because of logistic problems, proof of the fact that this technology needs intensive development. The economical evaluation confirms the criticality of the D&S because especially for the Ti6Al4 feedstock it's the most relevant cost contribution.

The current study is part of a larger project whose long-term goal is the economical and mechanical comparison between L-PBF and metal FDM to establish the applications in which metal FDM can be a low-cost alternative solution.

The study was possible thanks to the facilities offered by the Department of Mechanical and Aerospace Engineering of the Polytechnical University of Turin (Politecnico di Torino), Italy, and the Center for Physics and Bio-medical engineering of the Medical University of Vienna, Austria.

Key Words: *Additive Manufacturing, Metal FDM, AISI 316L, Ti6Al4V-5, HIPS, ASA, Tensile test, Debinding & Sintering.*

Abbreviations

AM	Additive Manufacturing
SLA	Stereolithography
FDM	Fused Deposition Modelling
BJ	Binder Jetting
DMLS	Direct Metal Laser Sintering
SLS	Selective Laser Sintering
SFF	Solid Freeform Fabrication
3DP	Three-Dimensional Printing
RP	Rapid Prototyping
CAD	Computer Aided Design
STL	Stereolithography
AMF	Additive Manufacturing File
Step	STandard for Exchange of Product model data
3MF	3D Manufacturing Format
JT	Jupiter Tessellation
VPP	Vat Photopolymerization
PBF	Powder Bed Fusion
EAM	Materia Extrusion AM
SDS	Shaping, Debinding and Sintering
BMD	Bound Metal Deposition
ADAM	Atomic Diffusion AM
FDMet	Fused Deposition of Metals
MF ³	Metal Fused Filament Fabrication
MIM	Metal Injection Molding
PIM	Powder Injection Molding
SLM	Selective Laser Melting
EBM	Electron Beam Melting
WAAM	Wire and Arc Additive Manufacturing
MBJT	Metal Binder Jetting

LOM	Laminated Object Manufacturing
DIW	Direct ink writing
3DGP	3D gel-printing
SSMED	Semi-solid metal extrusion and deposition
Metal-FDM	Metal Fusion Deposition Moulding
MAM	Metal Additive Manufacturing
L-PBF	Laser Powder Bed Fusion
EB-PBF	Electron Beam Powder Bed Fusion
L-DED	Laser direct energy deposition
EB-DED	Electron Beam Direct Energy Deposition
GMA-DED	Gas Metal Arc Direct Energy Deposition
GTA-DED	Gas Tungsten Arc Direct Energy Deposition
PA-DED	Plasma Arc Direct Energy Deposition
ASA	Acrylester-Styrol-Acrylnitril
HIPS	High Impact Polystyrene

Section 1

1. Introduction

AM is the term used to describe all the manufacturing methods in which the final shape of the object is achieved by adding material rather than removing it, as usual in traditional manufacturing processes. Frequently, it happens to refer to this group of technologies in different ways. Every definition highlights different features, for instance “Layer-Based Manufacturing” or “Solid Freeform Fabrication” (SFF) that underline the flexibility in manufacturing different and complex geometries, “Three-Dimensional Printing” (3DP) that is often used by the general public, and “Rapid Prototyping” (RP) that reminds the first implementation for which the AM was employed for [1].

The first common step of all AM technologies is the generation of the Computer Aided Design (CAD) file, the file that contains all the geometrical features of the object to be printed. The generation of such file can be achieved by creating it by means of one among many commercial software (SOLIDWORKS, AutoCAD, Fusion 360° and so on), by downloading it from apposite websites or through the acquisition by means of a 3D Scanner.

Geometrical features contained in the CAD file can't be manipulated as they are, thus they need to be discretized and converted in Standard Tessellation Language (STL) files or less frequently in Additive Manufacturing File (AMF) , Standard for the Exchange of Product Data (STEP) , Voxel, 3D Manufacturing Format (3MF) or Jupiter Tessellation (JT) files [2].

All existing AM technologies share the layer-by-layer shaping strategy. Given the targeted geometry contained in the CAD file, the shaping process of each layer requires a specific assignation of command to all components of the machine.

The translation of the CAD file is performed by the so called “slicer software”, a software that virtually slices the component and assign to each slice a list of command to be performed.

The slicer software and all the adjustable parameters depend on the adopted AM technology, since each AM technology exploits different working principles. The user is asked to provide to the slicer software all information about the process to help it in the definition of the printing strategy.

For example, in the FDM process are usually required the printing speed, the layer thickness, the fill rate, the nozzle, the bed temperature, and so on. Every material processed requires different settings, and some of them like the melting temperature of the material, the nozzle temperature, and the bed temperature are key parameters with important influence on the properties of the result. The slicer software plays a key role in determining the parameters because it can simulate the deposition process giving the possibility to predict the quality of the final result and fix possible mistakes.

The output obtained by the slicer software is the G-code file, the file that contains the list of commands to drive all the actuators (axes carriages, feeding system, shaping device and so on) in order to perform the shaping of the layers in a well-defined sequence [3]. The mentioned process is summed-up in the Figure 1.



Figure 1. Stages of the slicing process [3].

AM technologies are becoming more and more attractive both for the industrial and the academic research. One of the key reasons that justify this trend is the reduction of the extra expenditures involved during the product development stage [4].

A valuable feature for the biomedical field is the ability to 3D print little numbers of customised objects at a reasonable cost, where one-of-a-kind patient-specific goods are frequently required [4]. Furthermore, the interest of the AM in the medical industry has been piqued by the ability to generate an extensive diversity of medicinal transplants using computed tomography imaged tissue models.

Moreover, AM technologies are also sustainable technologies because, have better recyclability and reduced framework size constraints compared to molds [4], and minimises the need for international transit since when manufacturing locations are nearer to the ultimate target, all supply may be done utilising flee [4].

Finally, this pool of technologies perfectly meets the market demand because more and more objects marketed are more intricate, have smaller lifespan, quicker distribution periods, require more customization, and need less qualified personnel [4].

On the other hand, this kind of technologies are not suitable in all circumstances. Those limits are sometimes due to the recent spread and may be temporary because the AM has just lately become popular in a number of productions and patterns to final end products [4].

Some featural technical problems often remarked in literature are the lack of rigidity and strength in the manufactured components, very limited printing dimension, and the frequent needing for support structures to sustain overhang structures [4].

Compared to traditional manufacturing methods, in AM methods the material qualities exhibit a strong sensibility to the process parameters and often those parameters are tricky to manage [4].

In particular, depending on the type of AM process used, the end product may be influenced by a bunch of factors e.g. the material preparation, the layer formation technique, the stage variation occurrence, the material type, and the application requirements [4].

The AM was born with Hideo Kodama, that in 1980 developed the first AM technology consisting of an ultraviolet light to harden and create the solid part. Thus in 1990, Charles Hull developed the stereolithography process (SLA). In the early 1990s, Ely Sachs and co-workers developed the Binder Jetting process (BJ) employing metal materials. Next, Carl Deckard developed the Direct Metal Laser Sintering (DMLS) to focusing a substantial amount of energy in a limited spot and melt metal powder by means of a laser. This working principle is similar to the Selective Laser Sintering (SLS) technology that started to be developed for processing polymers in the late 1980's by Carl Deckard. Furthermore, in 1991, Scott Crump developed the Fused Deposition Modelling (FDM) to process some polymers, later widespread as the patent-free Fused Filament Fabrication (FFF) process [5].

The DMLS is currently the most popular Metal Additive Manufacturing (MAM) technology [6] employed for industrial applications, but it results significantly expensive [7], energy-consumption [8], safety measures and material procurement. The Extrusion-based Additive Manufacturing (EAM) may be an alternative choice because it results relatively low cost and straightforward to operate with the capacity to manufacture complicated geometrical components [9], as shown in Figure 2.

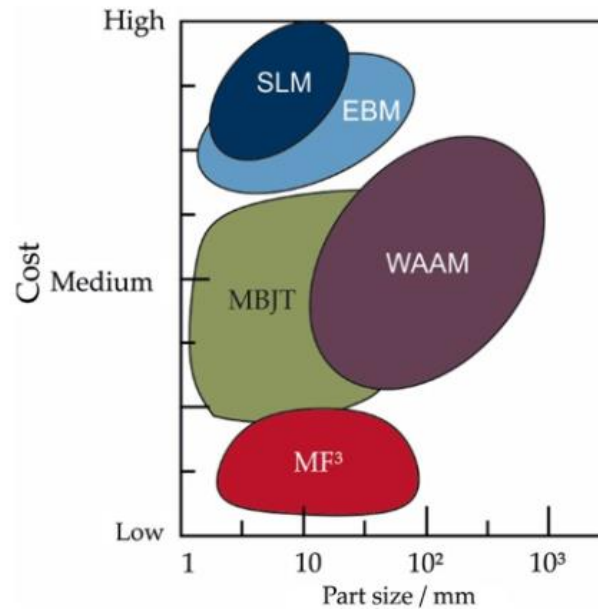


Figure 2. Comparison of key metal additive manufacturing methods in terms of part size and costs. SLM, EBM, WAAM, MBJT, and MF³ [10].

The reason of the competitiveness of EAM in terms of economy is due to the fact that the equipment is orders of magnitude cheaper than SLM machineries and powders with a great range of particle size distributions can be processed [1]. The Metal FDM is cheap EAM technology that can often be performed via ordinary and affordable FFF printers.

Depending on the assessed application, a feature may be a benefit or a limit, hence it's important to pick a particular application. The chosen application is the medical field, a field in which the price of the implants manufactured via DMLS may be not affordable.

The material adopted in the evaluation is the Ti6Al4V, a Titanium-based alloy widely employed in the medical field because of a set of properties like their lower modulus, superior biocompatibility and better corrosion resistance when compared to more conventional stainless and cobalt-based alloys [11].

Pure titanium and titanium alloys are widely used to replace hard tissue, shown in Figure 3 joints, and dental implants [11].

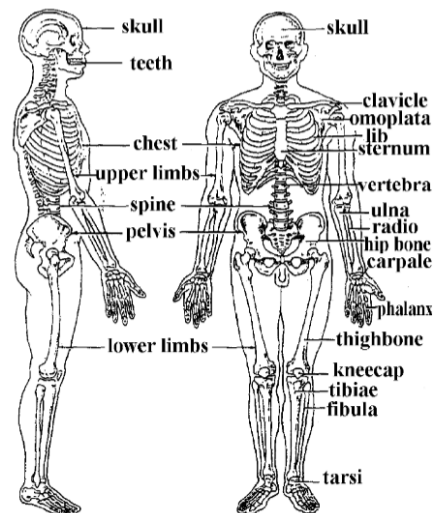


Figure 3. Schematic diagram of hard tissues in human body [11].

In short, the ideal materials or materials combination for hard tissue replacement prostheses should possess the following properties: a 'biocompatible' chemical composition to avoid adverse tissue reactions, an excellent resistance to degradation (corrosion) in the human body, acceptable strength to sustain the cyclic loading endured by the joint, a low modulus to minimize bone resorption, and a high wear resistance to minimize debris generation. Besides the above properties, bioactivity, which determines the osseointegratability of the implant, is very important to direct cementless anchoring of artificial bones, joints, and dental implants to bones. Thus, bad quality surfaces feature typical of metal FDM can result in a better osseointegrability since they can offer a larger surface.

Besides artificial bones, joints and dental implants, titanium and titanium alloys are often used in osteosynthesis, such as bone fracture-fixation.

Titanium and titanium alloys are common in cardiovascular implants because of their unique properties. Early application examples were prosthetic heart valves, protective cases in pacemakers [11].

Furthermore, rough surfaces and porous coatings have been shown to be good surfaces for osteointegration [11], a feature quite common of components made via additive manufacturing.

In literature, the Metal-FDM topic is up-to-date and could potentially be source of innovations but for the same reason there is a lack of scientific articles regarding this topic. Some studies on the applications and some aspect about the feasibility of metal FDM-made implants have been done.

P. Singh et al. [12] have assessed the printability of a tailored-made feedstock filament by using Ti-6Al-4V powder (Praxair Surface Technologies, Indianapolis, IN) through a tailored mixing process (Brabender CWB, Intelli-Torque Plasti-Corder) and then filament extruded (Gottfert Rheograph 20) before the deposition process.

Y. Zhang, S. Bai et al. [13] manufactured a Ti-6Al-4V filament by using a polyolefin-based binder system with the intention of assess the mechanical and microstructural properties of a metal FDM feedstock.

These mentioned studies adopt tailored filaments, an expensive condition that make it difficult to reproduce the consulted studies and compare the achieved results. In the current study, the printability study of the Ti6Al4V also aims to suggest a guideline to uniform the choice of the material. The chosen way to achieve this goal is the use of a commercially available material.

The reason why many studies adopt tailored Ti-6Al-4V feedstocks is that this material currently exhibits challenges along the manufacturing, the debinding and sintering process. Therefore, many suppliers do not invest in the process of this material or in few cases the material and the process are in development stage.

At the end of this study, a collection containing all the most important calibrations and precautions will be provided to guide other scientists that are beginning to engage with the Metal-FDM technology.

So far, the only suppliers that provide Ti6Al4V feedstock are Markforged, DesktopMetal and The Virtual Foundry. Contrary to DesktopMetal, that provides the feedstock in form of rod, Markforged and The Virtual Foundry provide the feedstock in form of filament, but Markforged hasn't make it available on its official website yet [14].

The long-term goal in which the current study is placed is the quantitative assessment mechanical properties and costs between the Metal FDM and the DMLS. The aim of this study is to gain technical expertise in the Metal-FDM and consolidate a procedure to perform tensile tests for specimens printed with this technology. Of course, since the titanium feedstock is extremely expensive, the understanding of the printer and the materials will be performed with cheaper materials such as polymers and steel feedstocks.

The titanium is also known as a "reactive metal" which means that if directly exposed to the oxygen, it reacts in a violent exothermic reaction and this problem influences the choice of the support material. The most popular support material normally employed is the Polyvinyl Alcohol (PVA) that is a water-dissoluble polymer. The oxygen contained in the water may react with the powder causing defects and problems in the D&S stage. Thus, the support material will be the High Impact Polystyrene (HIPS) that dissolves in an organic solvent.

As reported in the study of Y. Thompson et al. [15], the pore size plays a key role during the thermal debinding process. The study reports that during the thermal debinding, the presence of high heating rates and the pore sizes results in the blistering, shown in the Figure 4. The pore control will be thus an important aspect to consider in the optimization process.



Figure 4. Blistering effect on a specimen with a low pore control [15].

This condition made it necessary the design of a shrinkage test able to estimate the experimental shrinkage that we may expect from the D&S stage and become aware of possible unpredicted side effects.

The rest of this study is organized as following: Section 2 reviews all the existing Metal Additive Manufacturing (MAM). Section 3 describes all the stages of the Metal FDM process. In Section 4 all the equipment and materials are discussed. Section 5 defines the methods with which the activity was carried out. Section 6 provides a possible cost model for the Metal FDM process. In Section 7 are collected all the results of the study. Section 8 gives a critical discussion to the achieved results. Section 9 provides conclusions of the study.

Section 2

2. Metal additive manufacturing (MAM)

Referring to the EN ISO/ASTM 52921 (2015) standard, among the seven additive manufacturing processes groups categorised, four of these are nowadays utilized to build directly metal parts, respectively Powder Bed Fusion (PBF), Direct Energy Deposition (DED), Binder Jetting (BJ) and Sheet Lamination (SL). The other three categories, respectively Vat Photopolymerization (VPP), Material Jetting (MJ) and Material Extrusion (ME) are mainly used as indirect additive manufacturing [5].

Over the last three decades, many AM technologies were developed to produce polymeric, metal, and ceramic parts. Very often, new techniques are originally developed for the manufacturing of polymeric part and then, over the years, they are re-adapted and exploited for direct and indirect production of metal and ceramic parts, as happened in the case of VPP, PBF and EAM technologies [1].

2.1. Types of processes

Following, all technologies that can directly produce metal parts are discussed with some of the most relevant pros and cons.

2.1.1. Powder Bed Fusion

PBF-based processes can be classified in laser powder bed fusion (L-PBF), also known as Selective Laser Melting (SLM), and Electron Beam Powder Bed Fusion (EB-PBF), also called Electron Beam Melting (EBM). The PBF process can be employed to build complex prototypes and end-use metal parts with good resolution, reduced material wastage and efficient recycling of the un-melted powder [5].

The distinctive feature that characterizes different types of PBF is the source of thermal energy.

The **Laser Powder Bed Fusion (L-PBF)**, also known as Selective Laser Melting (SLM), is one of the oldest MAM processes developed, utilizes a thermal energy source provided by a laser beam to selectively melt and consolidate powder into solid shapes layer-upon-layer [5].

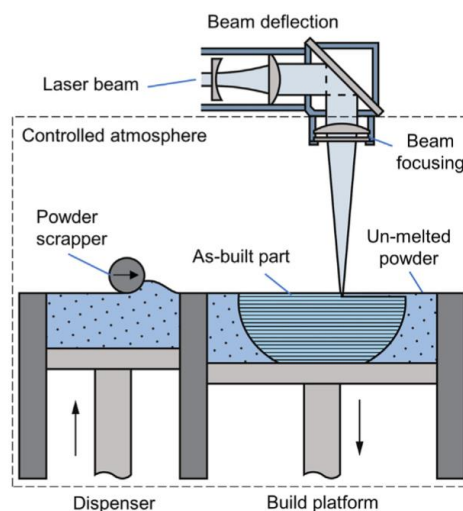


Figure 5. Scheme of the L-PBF process [5].

As depicted in the *Figure 5*, reflective mirrors are used to move the laser beam according to a predefined two-dimensional scanning path in controlled environment atmospheres of argon or nitrogen, depending on whether if the metal is reactive or not. L-PBF is a well-established MAM process that can process an extensive range of metal alloys whose properties has been widely assessed by researchers [5].

The widespread use of this process combined with the continuous evolution of printers by manufacturers allows results in deposition rates of up to 0.1 kg/h and surface roughness in the range of 10 – 20 μm . As a result, this constant progress explains the exponential growth of LPBF equipment sales in recent years [5].

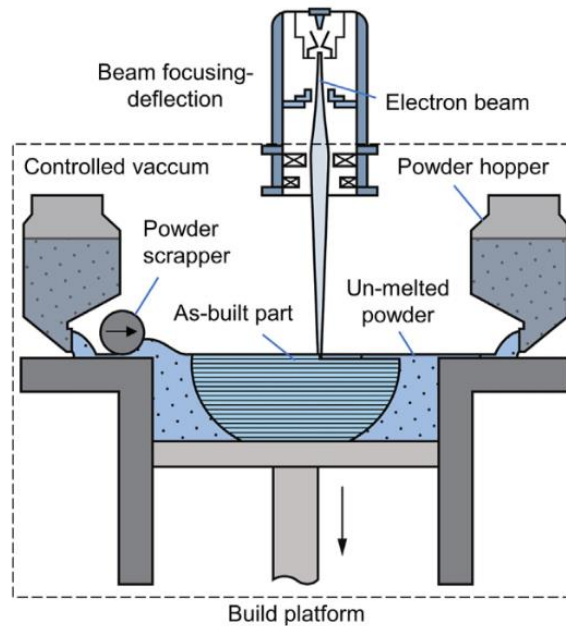


Figure 6. Scheme of the EB-PBF process [2].

The main working principle of **Electron Beam Powder Bed Fusion (EB-PBF)**, also called Electron Beam Melting (EBM), is similar to the one of L-PBF. The main difference between the two PBF systems is the source of thermal energy for melting the powder that in the case of the EB-PBF is an electron beam, depicted in *Figure 6*, instead of a laser beam.

The change in the source of thermal energy leads to several other modifications in the equipment because the electron beam works in controlled vacuum conditions and is focused and deflected by means of electromagnetic lenses, instead of mirrors. Moreover, the feedstock should be pre-heated to temperatures around 50 %- 60 % of its melting temperature to avoid powder spreading originated from electrostatic charging, the so-called ‘powder pushed-away phenomenon’ [5].

As a result of all the problems mentioned, EB-PBF is not as popular as L-PBF in research and industry. However, the EB-PBF has shown to be suitable in certain industrial applications, especially when it comes to handling difficult-to-process materials such as cobalt and nickel alloys, titanium aluminides, niobium, or even cellular materials [5].

On the other hand, the maximum deposition rates of EB-PBF are slightly higher than those of L-PBF and it’s capable of reaching values up to 0.2 kg/h with surface roughness in the range of 15–30 μm [5].

A common drawback of PBF technologies is that they are based on energy-intensive beams, which can result extremely expensive and highly energy-consuming. In addition, the powder must be free-flowing and, therefore, it requires a specific powder distribution, which adds to the price of the material [1].

2.1.2. Direct Energy Deposition

All DED-based processes share the focusing of the feedstock and a source of energy on a limited spot in order to ensure the deposition and melting at the same time.

The main difference between all DED-based processes are the source of thermal energy and the system adopted in the process. This technology is primarily adopted to repair metallic parts that are difficult to repair by other conventional methods [16].

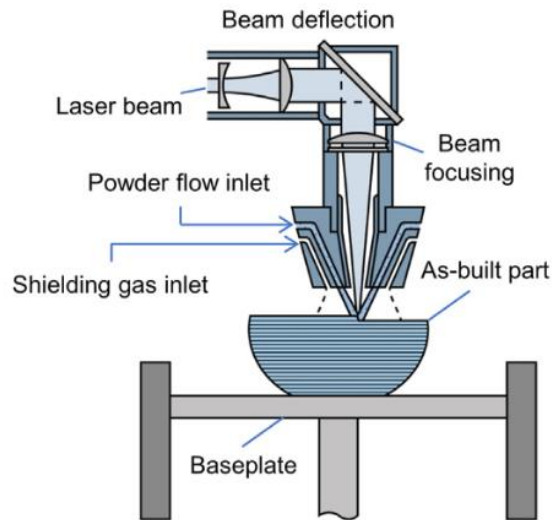


Figure 7. Scheme of the L-DED process [2].

Laser direct energy deposition (L-DED), whose scheme is shown in the *Figure 7*, relies on the working principles of laser cladding to build three-dimensional metal parts, layer-by-layer. The feedstock can be supplied as powder, resulting in feeding system through the laser head, whereas in case of wire, material is fed by means of an independent system, separated from the laser head.

The maximum deposition rates using wire feedstock can reach values up to 2 kg/h, and surface roughness is typically above 30 μm . Usually, shielding gases flows from the laser head to prevent the oxidation of the melting pool and act as carriers to help powder transfer to the melt pool [5].

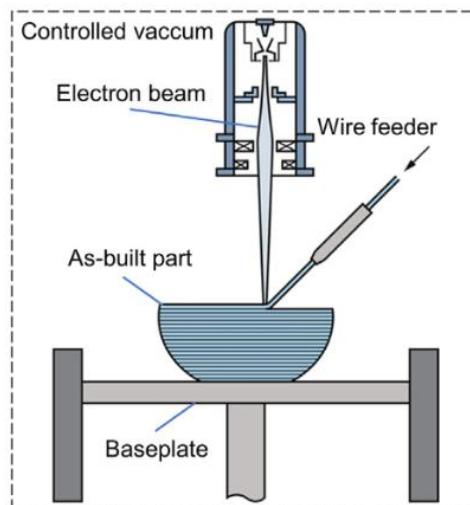


Figure 8. Scheme of the EB-DED process [2].

The working principle of **Electron Beam Direct Energy Deposition (EB-DED)**, shown in the *Figure 8*, is similar to that of L-DED except for the exploited source of energy that consists in an electron beam operating under controlled vacuum conditions.

Due to the use of a vacuum environment, the only form in which the feedstock can be supplied is as wire since the adoption of powder could compromise the final quality and accuracy of the parts. One of the key benefits of the EB-DED is the ability to manufacture large parts with deposition rates ranging from 3 to 10 kg/h, depending on the material and part features. A side effect of the high deposition rates combined with the development of large melt pools results in significant thermal stresses that requires adjunctive precautions. After the deposition process, the component needs a surface finishing in the coupling areas because the surface of the built parts is quite irregular [5].

WAAM (Wire Arc Additive Manufacturing) is a sub-category of technologies that gather all those processes using an electric arc as source of thermal energy and who share a similar working principle to the arc welding processes. WAAM-based processes show worst surface accuracy but better speed of process than L-DED, thanks to deposition rates that may reach 5 – 6 kg/h. Furthermore, they are also more efficient than L-DED because the energy conversion in the thermal energy saves more energy than the one needed to turn electrical energy into a laser beam. Compared to the EB-DED, we could state that deposition rate is higher, at the price of a worst accuracy. An aspect that makes WAAM-based processes attractive for research institutions and industry is the constructive simplicity of the machine and availability of materials.

In fact, welding equipment that are easily available can be converted in MAM system by purchasing the CNC mechanisms or by installing the equipment onto existing robots. Thus, this strategy allows to create a system capable of producing large size parts in a short time with an easy and inexpensive equipment.

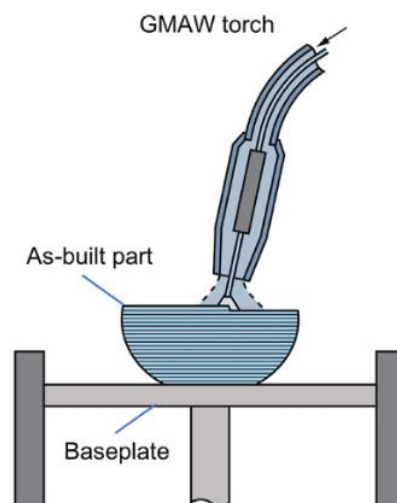


Figure 9. Scheme of the GMA-DED process [2].

The most relevant process included in the WAAM processes is the **Gas Metal Arc Direct Energy Deposition (GMA-DED)** [5]. The GMA-DED, also known as gas metal arc welding (GMAW), is a process in which an electric arc is established between the tip of a consumable wire (electrode), automatically fed through a nozzle into the weld pool, protected by inert or active shielding gases. The diffusion of the GMA-DED is due to the simplicity and cost-effectiveness of the process since it consists on an easy-to-implement direct wire-feeding, coaxial with the nozzle of the welding torch [5].

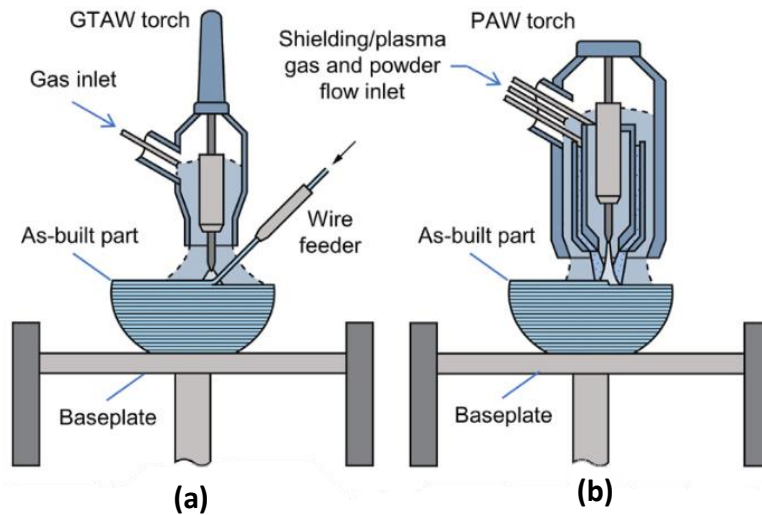


Figure 10. Scheme of the: (a) GTA-DED process; (b) PA-DED process [2].

The other two WAAM-based processes are the **Gas Tungsten Arc Direct Energy Deposition (GTA-DED)** and **Plasma Arc Direct Energy Deposition (PA-DED)**, respectively represented in the *Figure 10*.

They both use electric arcs that are formed between a non-consumable electrode (typically made of tungsten) and the metal adopted to build the component. The working principles of these two processes relies on Gas Tungsten Arc Welding (GTAW) and Plasma Arc Welding (PAW) equipment and so, differently from the case of the GMA-DED, the feedstock wire can't be supplied through the nozzle, but through an additional wire feeding unit. Compared to the GTA-DED, the PA-DED implies greater energy concentration resulting into better stability, less thermal distortion, and higher deposition rates. All those benefits explain the reason why PA-DED remains as the only electric arc-based MAM process which can be fed by powder feedstock [5].

2.1.3. Extrusion Additive Manufacturing

Metal Extrusion-based Additive Manufacturing (EAM) technologies exploit a mixture of metallic powder and a carrier matrix that is lately removed. The most popular EAM existing are mainly three and they all discussed in this paragraph.

Direct ink writing (DIW), also referred to as **robo-casting** or **3D gel-printing (3DGP)** is a metal extrusion-based method widely used to 3D print metallic components and recently employed to print porous titanium scaffolds[9]. This extruded material is supplied as a paste or ink (a mixture of binder and metallic powder) through a small nozzle. After the deposition of the ink is completed, the binder is removed by means of a sintering process. An overview of this process is presented in *Figure 11*.

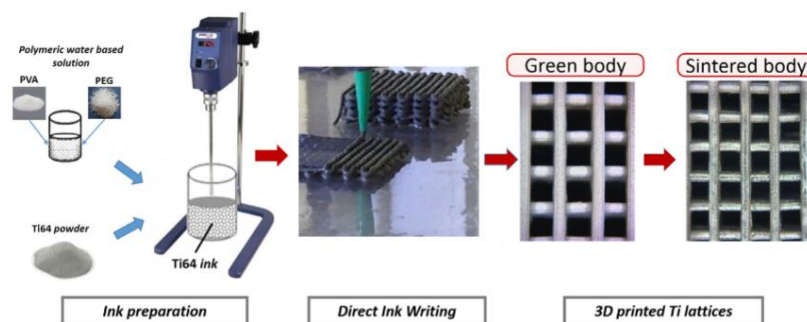


Figure 11. Schematic diagram of the DIWP process [17].

In the **Semi-solid metal extrusion and deposition (SSMED)** technique the material is supplied in form of a metallic wire. Thus, the component is printed according to the featural layer-by-layer building strategy. The wire needs to be heated to a mushy state becoming a semi-solid metal. At this stage, the mushy metal is solidly extruded on the platform by means of extruder like the one depicted in *Figure 12*.

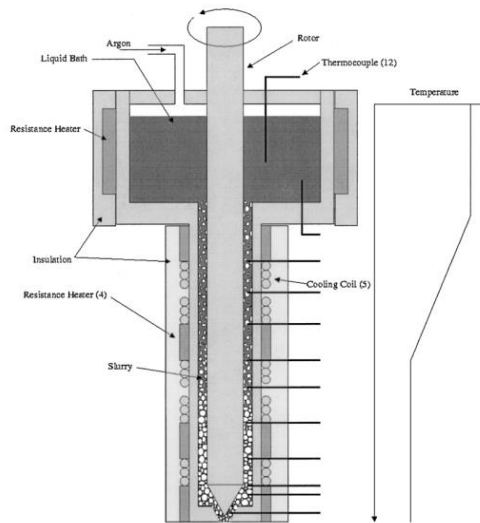


Figure 12. SSMED extrusion system [18].

The **Metal Fusion Deposition Moulding (Metal-FDM)** technique consists in the extrusion and deposition of a mixture of metal powder and a polymer binder. Next, the binder agent is removed, and, in the end, the mechanical strength is consolidated by means of a sintering process. The Metal-FDM is similar to the DIW process since they both share the extrusion of a mixture of powder and binder but contrary to the DIW process, in the Metal-FDM the material, the so called “feedstock”, is provided as a filament and extruded by means of a thermal softening.

This technique will be widely discussed in detail in the chapter “Metal FDM” (Page 25).

2.1.4. Binder Jetting

Binder jetting (BJ) process, whose deposition process is depicted in the *Figure 13*, consists of spraying a layer of powder on a build platform and following dripping an adhesive liquid agent through an inkjet style printer in order to selectively stick the powders together. Thus, once the cross-section of the layer is printing, the built platform is lowered to act the layer-by-layer strategy.

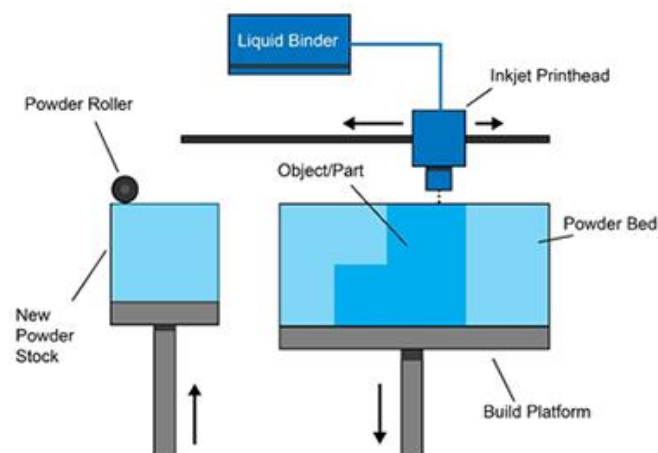


Figure 13. Scheme of the BJ process [19].

The end product is called 'green part', and exhibits low strength and approximately 60% relative density [16].

The green part is then heated in a controlled atmosphere to remove the adhesive agent and to sinter the individual particles into a 'fully dense' metal part. The main drawback of this process is that the gain of density achieved during the sintering is due to a vigorous shrinking that results in the loss of dimensional precision [16].

2.1.5. Laminated Object Manufacturing

Laminated Object Manufacturing (LOM), also named Sheet lamination is a technique, whose scheme is reported in Figure 14, that consists of joining thin metal sheets layer-upon-layer (via a system of feed rollers), to build a single piece. A post-process is usually performed to finish the surface through a milling machining to achieve a good surface quality. The single layer is cut with a milling or laser cutting and joined to the underneath layer by means of adhesive bonding, ultrasonic welding and friction stir welding [16].

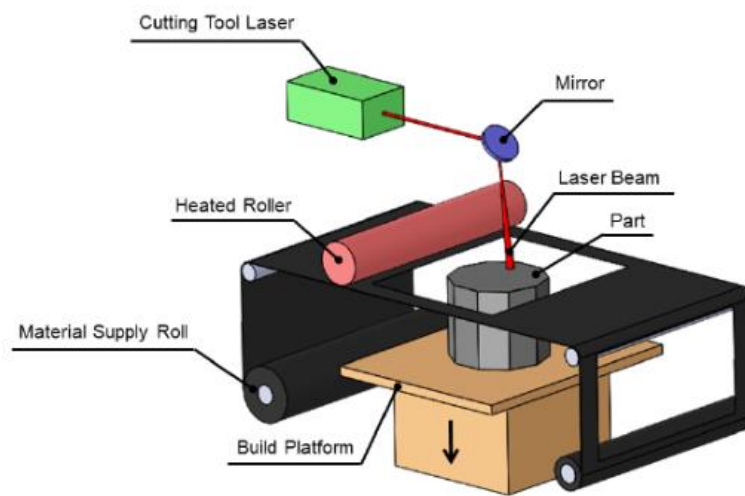


Figure 14. Scheme of the LOM process [20].

The sheet lamination is considered a high speed process as it is five to ten times faster than other AM processes, but on the other hand it is not able to achieve good geometric accuracy, surface finish and desired material properties [5].

2.2. Materials for MAM

In this paragraph we will discuss the most popular metals adopted in the AM with descriptions of some studies and applications.

2.2.1. Titanium Alloys

According to a review of M.Yakout et al. [16] many efforts have been focused in the evaluation of the characteristics of titanium TiAl6V4 produced by different AM processes for aerospace applications. The results of some studies underline that mechanical and fatigue behaviours of the SLM-printed TiAl6V4 parts suffer from internal voids and residual stresses resulting in a depression of the tensile strength and fatigue strength. Moreover, the microstructure of the SLM-printed TiAl6V4 components heavily influences the mechanical properties of these parts.

One aspect that make the SLM process difficult to manage is the high sensitivity of the end product to parameters such as scanning parameters, scanning strategies, and laser melting parameters. This strong

dependence results into a strong influence on the surface quality, voids characteristics, microstructure, and mechanical properties of TiAl6V4 parts.

Still according to M.Yakout et al. [16], some similar studies have been done using other AM processes such as DED and EBM leading to similar results and conclusions.

The excellent features of titanium-alloys justify studies and trials on the printability and application with some premature techniques. For instance, the titanium was adopted in the study of M.Shaik et al.[21] with the aim to develop a maxillofacial implant prototype via metal FDM.

2.2.2. Aluminium Alloys

Aluminium alloys are a key material in aerospace and automotive field because of his low density. However, so far, the use of this material is still associated to a number of challenges.

Many investigations focused on the AlSi10Mg alloy, aiming to find the process parameters required to maximize the density of components made via SLM. Furthermore, few other studies focused on investigating the mechanical strength of the aluminium parts produced by AM processes [16].

These studies highlighted how the microstructure of the SLM AlSi10Mg and AlSi12 parts significantly affects the mechanical properties such as fatigue behaviour, strength, elongation, etc. In turn, the microstructure of these parts is influenced by the imperfections formed during the process and to the post-processing procedures.

One of the weaknesses shown by AlSi10Mg is the fatigue strength, lower than that of a corresponding wrought material because internal voids and/or large internal precipitated particles serve as fatigue crack initiation sites [16].

A severe limit which cannot be solved concerns the anisotropic mechanical properties along the direction of the building, typical of components manufactured via AM. The direct consequence of this is the need for careful selection of the printing orientation of the component.

2.2.3. Iron- and Nickel- Based Alloys

Stainless steel 316L is the most popular steel material in powder-based AM processes. The end component exhibits a sensitivity rate to all details starting from the adopted raw material, which grain size influences the density and consequently the mechanical properties of the produced parts. In the DLMS technique some studies showed that point distance, exposure time, scan speed, layer thickness, and building direction have a strong influence on the quality of the parts produced. To achieve a reasonable surface finish and mechanical properties, mentioned parameters should be controlled during the fabrication process [16].

One of the benefits of AM technology is the opportunity to handle special alloys such as nickel-based alloys. Unfortunately, some studies showed that AM produced Inconel 718 parts contained small cracks that may affect mechanical properties in all directions especially in the building direction. The phase transition and the following formation of columnar dendrites during the melting process may result in cracks. Anyway, some studies demonstrated the potential of these alloys by finding the process parameters for fabricating dense parts from Invar 36 [16].

2.3. Applications

This paragraph looks at all the most relevant applications in which the combination of AM technologies and innovative materials has shown promising results.

2.3.1. Aerospace Industry

A key point for the aerospace industry is the production of lightweight and intricate geometries with good mechanical properties in small quantities. All of this makes AM a highly effective manufacturing process for aerospace applications.

The most common AM processes used in the aerospace industry are FDM, DED, DLMS, and EBM [16].

Components manufactured with these techniques are low-volume complex aerospace parts, aircraft wings. Furthermore, AM processes are used in the replacement of parts in the aerospace industry along with fabricating specialized parts, lightweight structures, parts with minimal waste, on-demand parts, and replacement parts to support long term space exploration.

Advanced materials such as aluminium alloys, titanium alloys, nickel super-alloys, and special steels have been manufactured in the aerospace industry using AM technologies.

Due to the high sensitivity of the final part to process parameters, AM technologies open the door for developing new materials and designs in the aerospace industry.

The main problem reported in the literature include mechanical anisotropy, microstructural inhomogeneity, residual stresses, dimensional accuracy, and poor surface finish [16].

2.3.2. Automotive Industry

Metal AM has significant implications on part design, the supply chains and also the inventory systems, which is particularly appealing for the automotive industry.

An important feature of using metal AM processes in the automotive sector is the opportunity to produce complex lightweight structures in order to reduce significantly the weight and still keeping the original strength of the original component. Plus, another important advantage provided by AM technologies is the in-house and on demand production of components, which reduces inventory needs, shipping costs, and material procurement costs.

Examples of automotive parts produced by AM involves structural composite components, engine valves, and turbocharger turbines [16].

Notwithstanding the capabilities of the AM processes in the automotive industry there are still many problem related to the production of components in large quantities e.g the dispersion of the mechanical strength achieved, the surface finish, and the dimensional accuracies. Most of these problems are caused by the great residual thermal stresses.

All these problems make it difficult to use AM components in mass production because it is difficult to guarantee a certain level of reliability.

In the end, the low processing speed is another problem that makes the AM technologies unsuited to mass production.

2.3.3. Tooling Industry

For the tooling industry, the AM can be a valuable solution because can speed up of the fabrication stages and reduce costs through the reduction of waste material, that in traditional subtractive manufacturing is tremendous.

A typical application of the AM technology is the production of customized molds with optimized cooling channels which can impart unique properties to parts and reduce production cycle time. In addition, AM

moulds manufactured with built-in conformal cooling also have a longer lifespan as they have a lower heat load associated with the work [16].

2.3.4. Healthcare Industry

The use of metal AM processes in the healthcare industry finds large application in the dental industry, in which AM processes are used for creating precise dental crowns, bridges, and implants. Indeed, features like the ability to perform complex, highly customized, and fully dense objects are crucial in dental applications and explain why the metal AM are so popular in this field, the SLM technique in particular.

The production of those implants involves the stages of scanning the dental impression of the patient's teeth, the extrapolation of the digital modelling of the part, and then SLM production.

The process has launched a new market for AM-manufactured dental implants. This new process is so efficient that it can compete with conventional manufacturing methods. Again, a similar process is used for the manufacturing of personalized prosthesis and supports for artificial teeth usually made of titanium or cobalt-chromium [16].

One of the greatest advantages offered by the application of AM metallic processes in the medical industry is the ability to quickly produce highly customized components. In fact, the technology is very useful in producing customized medical implants as well as surgical tools and fixtures for use in operation rooms with a better accuracy than the traditional methods.

The main benefit of AM in the medical industry is its ability to produce highly complex components with relatively low production costs.

2.3.5. Nanomanufacturing

A recent and interesting application of AM technologies has been found in nanotechnology for manufacturing parts with new nanocomposites.

The main benefit of using nanomaterials in an AM process is the enhancing of some properties of the fabricated parts e.g., better optical, thermal, electrochemical, and mechanical properties.

The most interesting applications of nanomaterials so far involves carbon nanotubes, nanowires, metal nanoparticles, nano-graphene, and quantum dots [16].

Additional applications can be found in the production of metal parts with nanopores, thus controlling the formation of pores and voids [16].

Section 3

3. Metal FDM

In the current chapter, the metal FDM process will be discussed. This technology consists in the deposition of a metal powder with the help of a binder, later removed after the shaping stage.

In the literature, this method has been referred to as Shaping-Debinding-Sintering (SDS) [22],[23], Bound Metal Deposition (BMD) [24], Atomic Diffusion Additive Manufacturing (ADAM) [25], Fused Deposition Modeling Metal (FDMet) [26],[15] and Metal Fusion Filament Fabrication (MF³) [27],[13]. The reason behind all these names is due to minor variations in the deposition techniques employed or it's due to corporations' monopoly on specific trademarks [9].

Metal FDM and BJ technologies share material combinations quite similar the one adopted in the Metal Injection Moulding (MIM) process, shown in *Figure 15*, often used in the manufacturing of small and high-geometrical accuracy needing components.

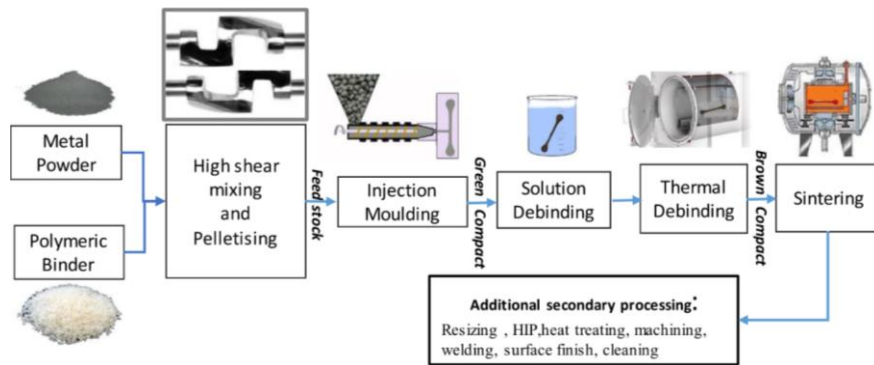


Figure 15. MIM process [28].

Hence, the knowledge of material and process developed so far in the Metal FDM is based on the knowledge gained with the MIM technology.

Of course, since the two technologies are slightly different, all parameters will be compensated, with particular care to the composition of the raw material, commonly named “feedstock”[29][9].

3.1. Process stages

In this section, we’ll discuss all stages standing between the generation of the G-code file and the achievement of a metal FDM-made object in order to better understand all challenges to face and all possible choices during the design of the manufacturing process.

3.1.1. Feedstock manufacturing

The source material is referred to as “feedstock”. Three steps must be considered throughout the feedstock preparation stage [9]:

1. Powder characterization

In order to use smaller nozzle diameters, fine powder is preferable because if the powder size is too big, large particles will potentially clog the nozzle, thereby terminating the fabrication process.

Another requirement regards the viscosity that should be low enough so that the compounded material can easily be pushed out of the nozzle. This requirement lead to prefer spherical powder [30].

A general overview of all possible techniques for evaluate the morphology, the chemistry and the microstructure of the powder is given in *Table 1*.

	Technique	Materials	Resolution	Particle size range	Advantages	Disadvantages
Particle morphology	Sieve analysis	Solids	Bin size dependent on the size of separation of sieves	20 µm–125 nm	Applicable to broad size range, minimal sample preparation, low cost	No insight into particle shape, longer measurement time, prone to blinding, particles with large aspect ratios can produce large uncertainties
	Microscopy	Dependent on microscope	$d = \frac{0.61 \lambda}{NA}$ d – resolution distance λ – light source wavelength NA – numerical aperture Dependent on instrument design and data analysis algorithm	Determined by system resolution	Allows qualitative and quantitative observation of particle shape, flexibility for particle size and shape analysis	Cost increase with decreasing particle size, SEM and TEM sample preparation require more effort than optical microscopy
Particle chemistry	Laser diffraction	Solids	Dependent on instrument design and data analysis algorithm	0.04–8000 µm	Short analysis time, does not require skilled labour, highly repeatable results	Errors can result from irregular particles, measurements dependent on instrument design, agglomeration detection is difficult
	XPS	Conductive solids	1 µm	Any conductive particles larger than the X-ray spot size	Determination of overall compositions and chemical bonding allows depth profiling	Sputtering through spherical particles can be difficult, requires a skilled user, cannot detect H
	AES	Conductive solids	0.5–2 µm	Any conductive particles larger than the electron beam size	Elemental analysis at a lower penetration depth compared to XPS	Destructive
	EDS	Conductive solids	2 µm	Any conductive particles larger than the electron beam size	Very fast, allows for point scans, line scans, and mapping elemental analysis	Semi-quantitative
	Fourier transform IR spectroscopy	Organic materials, some use with metals	>15 µm	Any conductive particles larger than the electron beam size	Able to determine the functional groups present in that material quickly and easily	Generally qualitative, must grind particles in order to allow transmittance of IR radiation
	Inductively coupled plasma – atomic emission spectroscopy	Primarily used for metals	20–50 µm	Particles must be completely dissolved in a liquid	Quantification of multiple elements at a wide concentration range	Destructive and expensive, unable to detect C, N, O, F, and H
	Inert gas fusion	Solids	Dependent on resolution of cells used to analyse H, N, and O	Any	Allows for detection of O, N, and H	Destructive
	XRD	Solids	Phases must have concentrations $\geq 5\%$	Best when powder particles are <150 µm	Able to determine crystal structures of phases	Only able to measure phases present >5%
	FIB	Conductive solids	1 µm	Any conductive particles larger than the ion beam spot size	Allows for direct visualisation of powder microstructure, aids in TEM sample preparation and cross-sections	Redeposition of milled material
	Transmission electron microscopy	Electron transparent conductive solids	Atoms	If particles are larger than 500 nm, they must be thinned	Offers imaging and diffraction capabilities	Difficult sample preparation, requires a skilled user
Thermal analysis	Solids and liquids	1–2°C	Any	Allows insight into the endo- and exothermic transitions associated with the sample	Destructive	

Table 1. Overview of powder characterisation techniques commonly used in AM [31].

Several research groups are investigating different materials such as 316 L steel, 17-4PH steel, Ti6Al4V, NdFeB, copper, zirconia, alumina, silicon nitride, lead zirconate titanate, fused silica, tricalcium phosphate, hard metals, cermets, and multi-material parts combining ceramics and metals [1].

2. **Compounding of powder and binder** A sinterable metal-and a polymeric-based binder are utilized in the feedstock of metal FDM [9].

During this stage high – shear mixers, and roll mills are used for batch compounding.

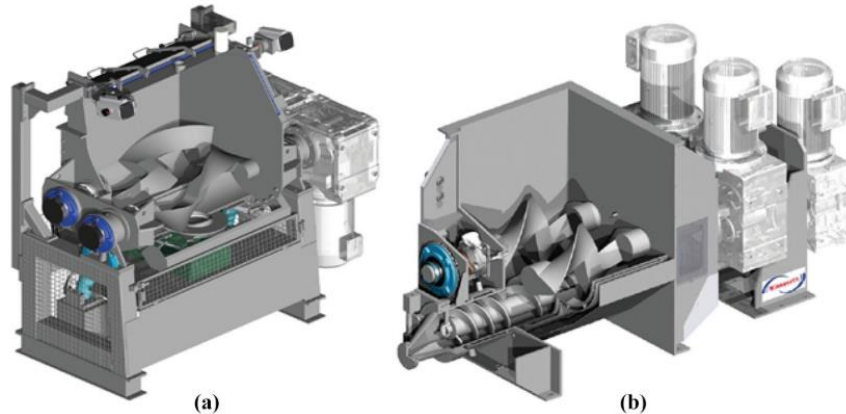


Figure 16. Mixer used to produce the feedstock: (a) z sigma blade mixer and (b) zx sigma mixer-extruder [32].

The compounding step is extremely important because the failure to deagglomerate and evenly distribute the powder at this stage will result in downline defects in both fabrication and post-processing operations. Various techniques, such as, measurement of mixing torque or energy, shear modulus, viscosity, etc. are used to assess the quality of mix and to ensure consistent and repeatable compounding from batch to batch [33].

Currently, binder system with only one polymeric material can be employed, but then the debinding step will be performed through only to thermal degradation, a very slow process compared to solvent or catalytic debinding.

In order to achieve the appropriate mechanical properties it's compulsory to use multi-component polymeric binder systems [1].

Generally, three main components that constitute the binder system can be identified as [34]:

- The **main binder** component is the component present in the largest amount and usually is removed in the first stage of the debinding step. The targeted composition of the total binder system is between 50 and 90 vol %.
- The **backbone** is the component used to give the print the stability of shape after the removal of the main binder during the first debinding stage and then be thermally decomposed prior to sintering. The amount of backbone usually varies between 0 and 50 vol% of the total binder system.
- **Additives** of different nature like dispersant agents, compatibilizers and stabilizers help to disperse the filler particles in the polymeric binder, preventing agglomeration and phase separation. Additives concentration varies between 0 to 10 vol % of the binder system.

The choice of binder component is a key point since the binder melting and degradation temperature are parameters that deeply affect the feedstock properties in each stage of the

process, indeed the feedstock mixing temperature should be higher than the maximum melting point but lower than the lowest degradation temperature of the binder components. It's easy to figure how both metal powder and binder affect the thermal conductivity, heat capacitance, as well as regulating the maximum shear rate and other printing factors besides more important features like the maximum powder content, the strength of the green part and properties of the final product after post-treatment.

The golden standard to succeed in the manufacturing of a binder are a low melting temperature, high capability to wet the powder particles, readily removed in post-treatment, be environmentally friendly are some of the properties of a suitable binder [9].

3. **Filament manufacturing** Once the metal powder is joined together with the binder, the feedstock can be manufactured in different shapes with respect to the feeding system which whom the printing machine is equipped with.

We can identify two main way to feed the printer [9]:

- **Discontinuous printing from rods**, fed by means of plungers like the one shown in *Figure 17* [9].

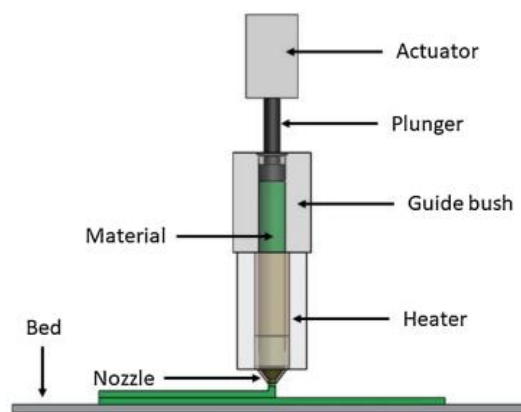


Figure 17. Material Extrusion with Plunger-based [3].

Desktop Metal Inc. currently offers metal FDM machines that use rods made up of metal powder and a thermoplastic binder. Desktop Metal calls their process. The rods are fit into cartridges and then softened in order to be extruded easily. The soft material is then stocked in a reservoir, later pushed by a plunger in a calibrated nozzle and eventually deposited onto the building platform in a layer-by-layer manner. Since this system is patented, it owns distinctive features, in particular an ultrasonic vibrator that ultrasonically bond an extruded building material onto the previously deposited layers.

Those designed systems are meant to be used in exclusive for metal FDM, thus the rods have a large amount of powder and the printed parts are sintered to obtain a dense part and designed rods use similar materials as used in the well-established process of PIM process [34]. The main drawback of those systems can only use a proprietary slicer software, hence parameters that the user can change are extremely limited.

By way of example, we report in *Table 2* some binder compositions regarding the PIM but easy to extend to the Plunger-based EAM.

Main Component (50–90 vol %)	Backbone (10–50 vol %)	Additives (1–10 vol %)
Carnauba wax	Polypropylene (PP)	Stearic acid
Paraffin wax	Ethylvinylacetate (EVA)	Stearic acid
Paraffin wax	High density polyethylene (HDPE)	Stearic acid
Paraffin wax	Polyethylene (PE), PP	Stearic acid
Paraffin wax	HDPE, PP, Polystyrene (PS)	Stearic acid
Paraffin wax	PE	Stearic acid, oleic acid
Polyethylene glycol (PEG)	Polymethyl methacrylate (PMMA)	Stearic acid
PEG	Polyvinylbutyral (PVB)	Stearic Acid
PEG	Polyethylene wax	Stearic acid
PEG	Polyimide diisocyanate	2, 6-di-tert-butyl-4-hydroxytoluene
Polyoxymethylene (POM)	Low density polyethylene (LDPE)	Stearic acid
POM	Polyolefins	Poly-1,3-dioxepane or poly-1,3-dioxolane or mixtures thereof
POM	PE	Butanediol formal
Agar (gel forming polysaccharide)	Glucose	Deionized water, calcium borate, methyl-p-hydroxybenzoate and propyl-p-hydroxybenzoate as biocides
PEG or polypropylene glycol or polyvinyl alcohol	PS and /or PE	Methylene chloride
Partially hydrolyzed cold water soluble polyvinyl alcohol	PE or PP	Glycerin, INT-33PA, steric acid, water

Table 2. Examples of binder system compositions used in PIM [34].

- **Filament-based printing**, commonly employed in commercial printers. The feedstock is shaped more commonly in filament, less commonly rods as well, and employed in systems like the one shown in *Figure 18*.

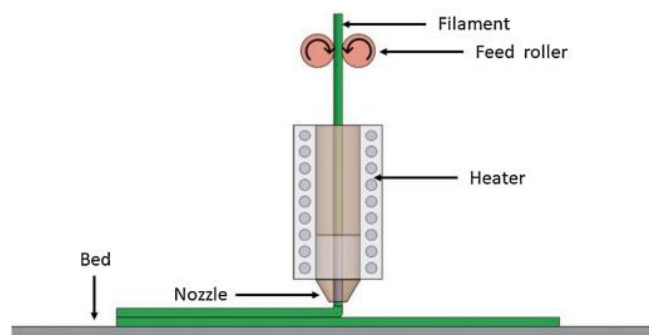


Figure 18. Material extrusion with filament-based [3].

The material extrusion of filaments was first patented by the company Stratasys and commercialized as fused deposition modelling or FDM™. Despite the application was considered as ram extruders, with the filament being the ram that pushes the softened material out of the printing head, the name of the commercialized system was very general and could also cover other feeding methods besides filaments or rods. Due to the vague meaning of the FDM term and due to the corporations' monopoly on specific trademarks,

an alternative terminology was introduced as fused filament fabrication (FFF) to underline the shape of feedstock material and bypass patent-related problems. In this process heated chamber and/or heated building platform can be used to promote adhesion to the printed bed and to reduce thermally induced stresses.

The common features required to the filaments are:

- Sufficient mechanical strength to retain its shape after being forced through the drive wheels to transfer the force into the liquefier.
- Enough friction between the wheel and the filament to transfer the force from the wheels to the filament.
- Enough strength to avoid to be cutted by the pinching force the wheels of the feeding system .
- The filament may buckle between the drive wheels and the entrance to the liquefier due to the force transferred from the feeding gear to the filament that should be efficiently transferred into the center of the liquefier in the direction of the melt flow, so that losses due to filament buckling and compression are minimized.
- Enough flexibility to be spooled, so that the storage of the filament can be and the feeding can be continuous [34].

A commercial example of printers designed on purpose for metal FDM and adopting filament-shape feedstock is given by the U.S. company, Markforged Inc. that patented the ADAM™ process by implementing a laser scanning displacement sensor on the printed head that acts as an in-process inspection tool to guarantee geometrical accuracy.

By way of example, we report in *Table 3* some binder compositions regarding filament-shaped feedstocks.

Main Component (50–90 vol %)	Backbone (0–50 vol %)	Additives (0–10 vol %)
Elastomer and wax	Polymer	Plasticizer, tackifier, oleyl alcohol
Amorphous polyolefin	Amorphous polyolefin	Tackifier, wax, plasticizer, surfactant
Microcrystalline wax	Ethylene Vinyl Acetate (EVA)	None
Thermoplastic elastomer (TPE)	Grafted polyolefin	Unspecified compatibilizer
4 hydroxybenzoic acid-behenylester solid, and 4 hydroxybenzoic acid-ethyhexylester	Co-polyamide (PA) 6/12	None
HDPE	None	Isopropyl tri(dioctyl)pyrophosphato titanate, tri(dioctyl)phosphato zirconate or mixtures thereof
POM	Polyolefin, and other polymer (polyether, polyurethane, polyepoxide, polyamide, etc)	None
PA	None	Undisclosed
Undisclosed	Undisclosed	Stearic acid
LDPE wax	LDPE	None
Polypropylene	Elastomer	Wax, tackifier, plasticizer

Table 3. Examples of binder system compositions used in filament shaped feedstocks [29][34].

- **Continuous printing from extruded granules**, low-cost system usually involved in research applications. The feedstock is shaped in pellets that can feed systems like the one shown in *Figure 19*.

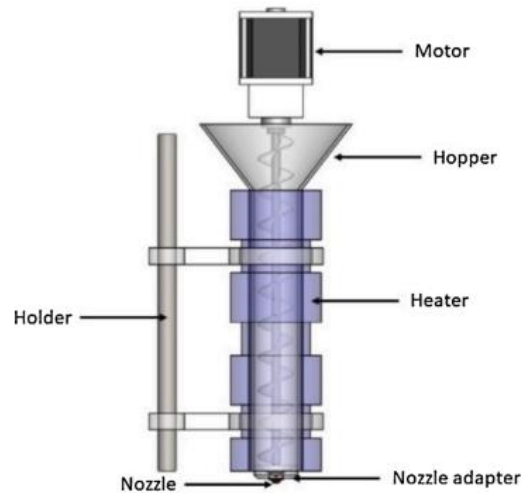


Figure 19. Material extrusion with screw-based [3].

The production of rods or filaments is quite demanding and requires a specific know-how of the process in order to achieve a material with strict geometrical and composition features, besides an adequate stiffness to resist mechanical stresses due to the feeding systems like rollers or plungers. Therefore, for research and development purposes it makes sense to skip the stage of optimization of all these technical aspects especially if we are interested in the assessment of material properties and not in the process optimization and the suitable solution is the adoption of pellets, easy to manufacture and manage, as feedstock material. The feedstock is hopped into the mouth of the feeding system and while it's moved to the nozzle unit thanks to the role of the screw, it's softened by means of several heaters and by the effect of the friction. In the vicinity of the nozzle, the action of the screw pump causes the melt feedstock to undergo high pressure and finally it's pushed through the nozzle to be then finally deposited.

However, controlling the flow of the extruder to deposit the material in a precise manner could be a more challenging task and requires other tools as compared to ram extrusion and furthermore, the size of the pellets should be controlled in order to obtain a uniform flow of the extruded material [29][34].

By way of example, we report in *Table 4* some binder compositions used in pellet feedstocks:

Main Component (50–100 vol %)	Backbone (0–50 vol %)	Additives (0–10 vol %)
PE wax, paraffin wax, PEG	PP	None
PEG	None	None
Paraffin wax	LDPE	SA

Table 4. Examples of binder system compositions used in pellet feedstocks [29] [34].

3.1.2. Shaping stage

Layer-wise deposition of the feedstock is accomplished using plunger-based, pinch feed, or screw-based mechanisms, respectively [9].

The usage of proper support and its requirements is complicated and must be done with care. Anyway, information regarding the support material and its removal in metal FDM are quite uncommon to find. However, in the commercial metal FDM 3D printers of Markforged and Desktop Metal incorporation, a ceramic layer between the raft/support and the main part is printed. This ceramic layer disintegrates during the sintering process, which facilitates raft/support removal [9].

There are two type of extrusion systems, namely, Bowden extruder and Direct extruder as shown in *Figure 20*. The difference between Direct and Bowden extruder is the distance from the motor drive gear to the heated liquefier. The Direct extruder's motor is mounted right on the top of the heated liquefier and can perform a reliable extrusion but in the other hand this lead to an higher weight to be drifted on the carriage system, while the Bowden's motor is placed away causing the lightening of the carriage at the cost of extrusion dynamics that depend on the stiffness of the filament [35][36].

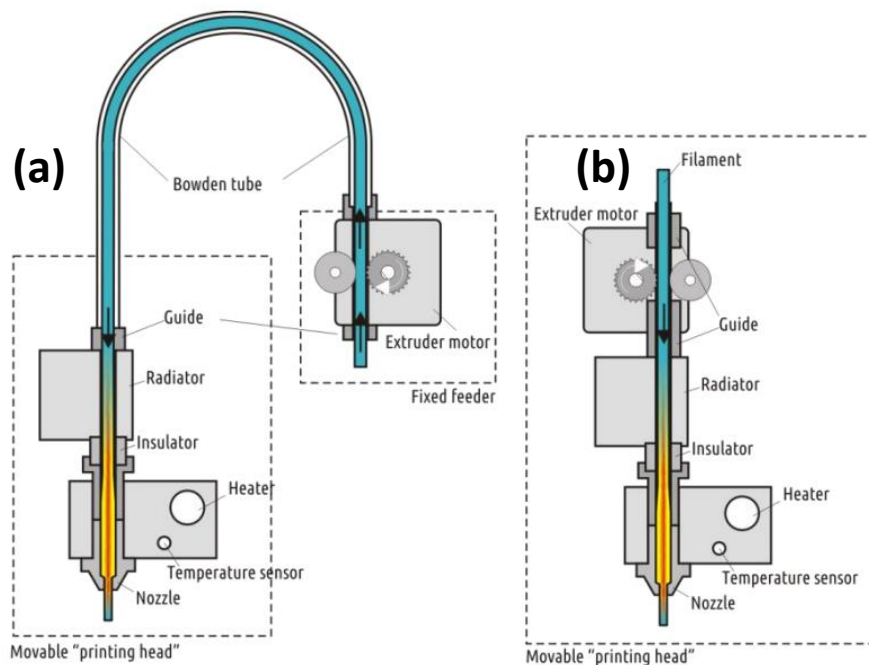


Figure 20. Extrusion systems: (a) Bowden extrusion; (b) Direct extrusion [28].

Since with the metal FDM it's not possible to perform overhang structures, during the slicing stage it's possible to include support structures. Single-nozzle printers can build this kind of structures with the "part material", the material employed to manufacture the main component. Because of the strong bonding between two layers of same materials, the removal stage of the support material is risky and delicate because the final component could be accidentally damaged during the operation [37]. To overcome this problem, some cutting edge printers are provided with double extruder in order to print the support structure with the "support material". The support material is designed to help and make easy the removal of the support structure by dissolution (detergents or water-dissolvent supports). Depending on the cost of

the support and the part material, it may happen to adopt the support material as interface between the part and the support structure, as depicted in *Figure 21*, to decrease the amount of material needed.

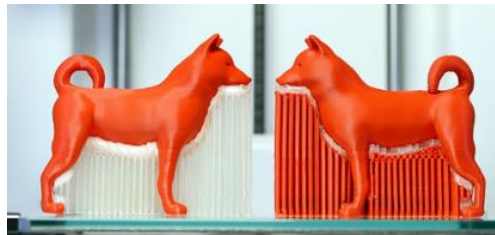


Figure 21. Different way to apply the support material [38].

In this stage all the complexity of the process is manifested since the print results strongly depends on all settings. Some of the most relevant parameters and whose effect is easily visible on the final result are all the setting related to the melt filament called in jargon raster, depicted and defined in *Figure 22*.

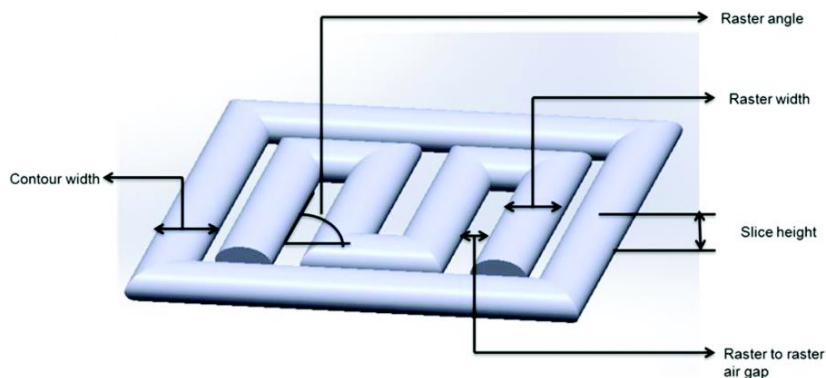
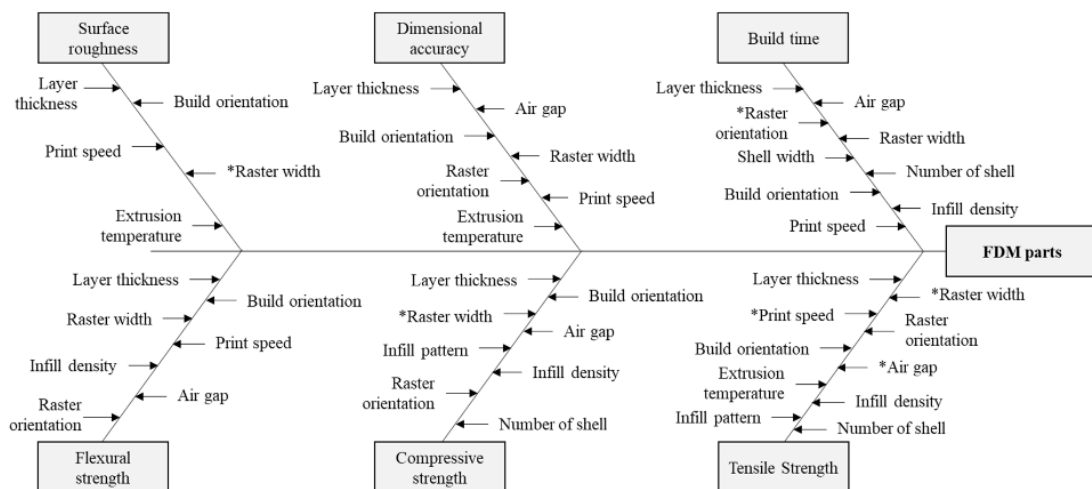


Figure 22. FDM parameters [39]

During the shaping stage, the choice of all parameters is expressed in surface quality, time of the print and density of the final product.

It's easily to suppose that all parameters that affect the quality of a print made via polymer FDM, shown in *Figure 23*, will also show some influence in the metal FDM products.



* Indicates still unknown whether a parameter is significant for a part characteristic or not

Figure 23. Influence parameter in the FDM process [40].

Of course, the metal FDM process is more articulated than the polymeric FDM process and hence every stage of the process with respective choice of parameters will also influence the mechanical performances of the final result, as depicted in *Table 5*.

Metal FDM steps	Parameters
Design	Dimensional design, part's shape complexity
Characterization of feedstock constitutes	Size, shape, and chemical composition of powder particles, powder drying conditions, granulometry of the powder, binder type and composition
Extrusion and feedstock preparation	Rotational speed, pressure and temperature of the extruder, extruder's nozzle temperature and diameter, granule viscosity, the volume fraction of the metal powder in feedstock, shear stress in preparation of the feedstock, bending and tensile strength of the filament
Print	Bed temperature, cooling rate after deposition, printing speed, build orientation, infill type, raster angle, adhesion of layers, layer's height and width, melting and degradation temperatures of the filament
Debinding and sintering	Cycle time and temperature, atmosphere, and pressure of furnace, residual carbon, toxic metal ions, nitrogen, or other elements of the sintered part, type and quality of equipment and furnaces

Table 5. Main parameters of influence in every step of the metal FDM process [9].

Eventually, the component obtained through the deposition process is referred to as “green part”.

3.1.3. *Debinding stage*

Debinding eliminates most of the binder material in the green part. This process is influenced by the thermal cycle of the debinding process and the kind of debinding or combination of these.

Thermal debinding: The thermal debinding, or polymer burnout, is a widespread process of polymer removal. The reason why the thermal debinding is the foremost method for polymer removal in industry can be attributed to the simplicity of the method and its applicability for mass production to combine with sintering operations. Anyway the process is noticeably complex even though the equipment used and the method is fairly simple. Polymer removal by burnout involves chemical mechanisms like the thermal degradation of polymer into volatile species and physical mechanisms like the diffusion mechanism of the degradation products to the surface of the component as well as evolutions in the polymer distribution within the green body. During this process, there's a dramatical drop in the mechanical strength of the component first due to thermal softening of the polymer and subsequently due to loss of the polymer. Simultaneously, stresses (thermal, gravitational, residual, and so on) act on the component that can generate cracks or distortion as the polymer degrades.

Like macroscopic defects, any microscopic defects caused during thermal debinding can dramatically affect result of the sintering process because contrary to general impressions, sintering does not heal debinding defects, but instead exacerbates those defects.

The explanation of that is because improper thermal debinding can result in carbonaceous residues that usually degrade the mechanical and physical properties of the sintered component.

The only way to decrease the magnitude of those effects is the common practice to employ extremely slow heating cycles at the cost of a worst productivity and higher expenses [41].

To prevent oxidation and other problems during debinding, the part must be isolated from the air and this may be done using a shielding gas or burying the part in a refractory such as aluminum oxide (Al_2O_3), activated charcoal, or talc powder, which is sometimes known as “wicking”. Care must be taken to avoid trapped gasses or areas of binder that were not completely degraded during the debinding, as these can cause severe defects in the part during sintering. This is especially an issue when debinding thick parts, so great care must be taken to ensure full penetration of the heat into the part to remove the binder [42].

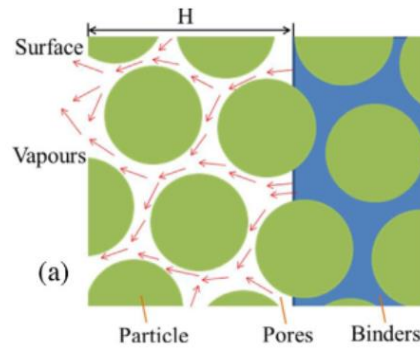


Figure 24. Process diagram for thermal debinding [42].

Thermal debinding is particularly suitable for green bodies with a small size [43].

Solvent debinding: Main benefits of solvent debinding includes a good process speed and highly effectiveness process at low cost. During the solvent debinding process, green bodies are impregnated in low-molecular solvents, accompanied by dissolving of the binders. As the binders and low-molecular solvents diffuse from bulk to the surface of the green bodies, resins will be removed from the green bodies [43].

The solvent debinding usually requires the part to be debinded in two steps, the first one to dissolve most of the binder and the second to thermally degrade the remaining polymers but in this case the heating step takes much less time compared to direct thermal debinding. The effectiveness of the solvent debinding compared to the thermal debinding depends on the composition of the binder since some complex binder compositions may require the use of solvent debinding, as thermal debinding would not be able to properly prepare the part for sintering. The solvent extraction rate depends on the dissolution and diffusion process. Therefore, it is dependent on the temperature, time, and characteristics of the particles such as the shape, size, and distribution of the powder.

After the soluble binder component is removed from the part, sometimes it must be heated to remove the backbone polymer while maintaining the geometry for sintering. This thermal step can be done in the sintering furnace with temperature between 200 °C and 600 °C for 2–4 h, which are high enough to degrade the polymer without damaging the powdered metal components [42].

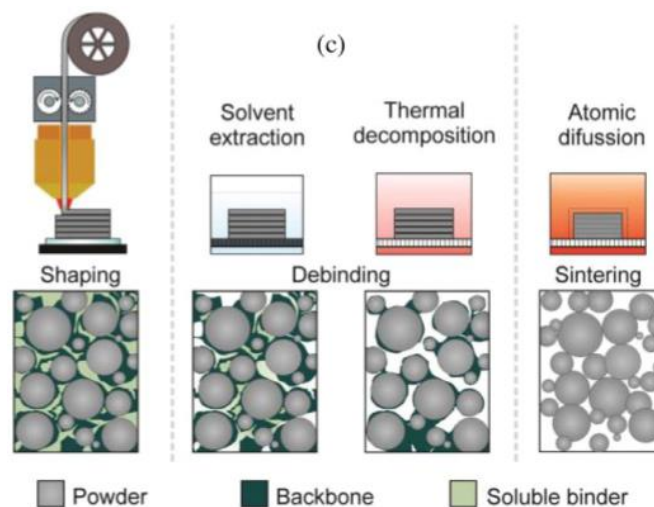


Figure 25. Solvent debinding process [42].

Water debinding is part of the group of solvent debinding. In particular, an aqueous solution is used to remove the binder instead of an organic one. Although its use is restricted to water-soluble binders, it is preferable to organic solvent debinding where applicable, as it is clearly safer and more environmentally sustainable, as well as being more effective for some binder polymers [42].

Catalytic debinding: Catalytic debinding is a fast-debinding process in which the binders rapidly decompose into volatile molecules in the catalyst atmosphere. Catalytic debinding systems utilize a combination of thermal and solvent debinding mechanisms, whereby the polymer chains of the primary binder are splitted into the monomer form with the help of a catalyst agent.

The catalytic debinding is based on solid-to-vapor catalytic degradation that helps the removal of the binder and improves the strength of the resulting brown parts, which is critical in the handling operations.

In this debinding, the main binder is removed by being attacked directly by a catalytic acid vapor. The binder mass is removed primarily by being converted into a vapor by the catalyst and then blown away, resulting into a polymer binder system removal faster than in the case of thermal and solvent methods. The main advantage coming from the catalytic debinding approach is that generally produces a well-interconnected porosity after a short time (about two or three hours depending on the size of the component) [43].

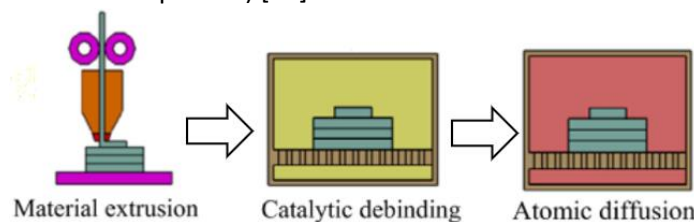


Figure 26. Catalytic debinding process [42].

Unlike the other two, which worked with a diverse range of different powders and binders, catalytic debinding has only been applied to stainless steel parts and some specific binders. This suggests that the catalytic debinding process has a limited application range, but it was found to be very fast and effective for the cases where it was used. Unlike the other debinding processes, the catalytic debinding is very effective for parts with a very high powder content. This feature is motivated by the fact that the gas penetrates more effectively into the pores of the part to reach the binder than what a fluid would do. In some cases, the speed of the reaction of the catalyst is so high that components can collapse if this is not controlled for. Thus, catalytic debinding results extremely suitable in applications with high powder density.

To maintain the component's form and minimize thermal stress and considerable weight reduction rates, the rate of temperature decline/increase in time must be slow enough.

The debinding is a delicate stage because the part material is extremely brittle and very sensitive to all stresses and occasionally it happens that even small residual stresses due to the shrinkage can lead to cracks or structural failures. Wall thickness variations and distortions caused by thermal processing should be considered, particularly in components with varying wall thicknesses. Numerical simulation softwares can aid in the prediction of these failures and possibly to reshape the component [44].

The thermal debinding method is the only case in which the binder system's constituents will be thermally removed in one step unlike other mentioned debinding manners [9]. Once the debinding stage is over, the component is called "brown part".

3.1.4. Sintering stage

During this stage, the part undergoes high temperature, however lower than the melting point of the metal, and mechanical resistance increases thanks to the necking process that decreases the residual porosity although residual micro-porosities will persist anyway.

The necking is due to up to six mass transfer mechanisms namely surface diffusion, lattice diffusion, grain boundary diffusion, evaporation-condensation, viscous flow, and plastic flow [3].

The ultimate outcomes of sintering depend on temperature, time, and furnace atmosphere.

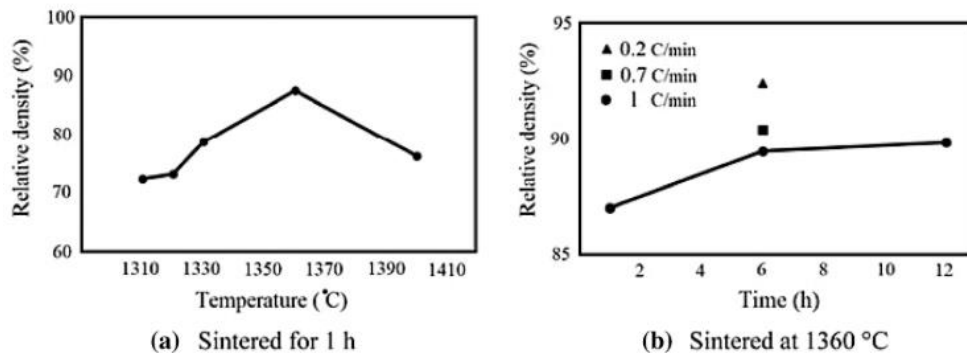


Figure 27. Relative density in function of: (a) Temperature; (b) Time [45].

As shown in *Figure 27* the temperature and time exposition affect the relative porosity of the component.

As in debinding, in sintering the thermal cycle is a thermal ramp in which after a transient the scheduled temperature is reached and kept constant, hence for a process simplification they're performed in sequence in the same furnace.

The temperature rate adopted to reach the thermal debind and sintering temperature is crucial because it can heavily affect the component properties, has depicted in *Figure 28* regarding the microstructure.

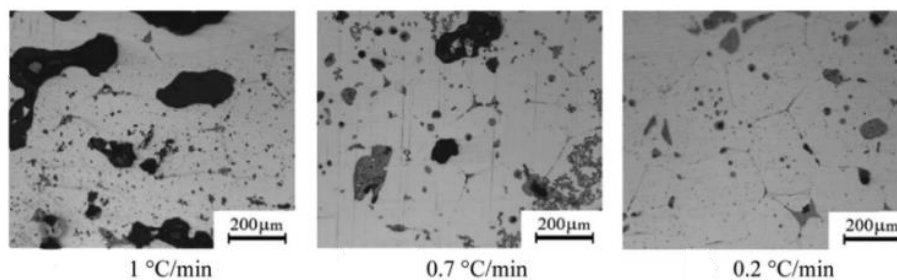


Figure 28. Effect of different debinding rates on SS 316 L samples sintered at 1360 °C for 6 h [45].

When the sintering temperature is achieved, the leftover binder is devolatilized and eliminated. After that, the metal particles fuse and the metallic microstructure develops from the part's outside to its inside. Moreover, residual stress at grain surfaces and stress between grains increase.

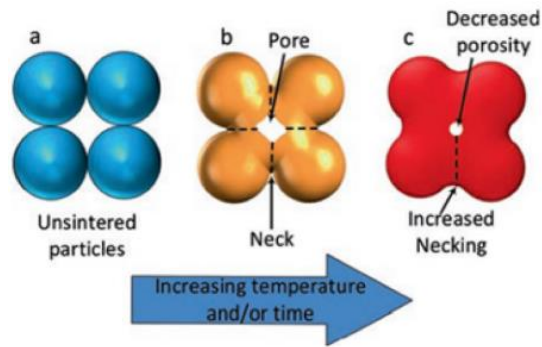


Figure 29. Necking process during the sintering [9].

As depicted in *Figure 29*, sintering involves the necking and as time and temperature rise, the more the necking will show, and the dimension of residual pores will decrease.

The sintering environment influences process productivity, costs and most important thing, the resulting microstructure i.e., by processing the component in a vacuum or inert gas furnace it can prevent thermal oxidation. Inert gases usually employed in this sintering process are argon, hydrogen, and nitrogen [3].

All effects discussed make it clear that the importance of adopting an homogeneous feedstock material is important and necessary in order to achieve a good quality [9].

3.2. History of the technology

This process was first introduced in the 1990s, based on the Stratasys™ technology [1]. Their FDM system had two extrusion heads and fed by two distinct spools of material in which one material was used to build the part and the second was used for the support material. Market entry of other companies as emerging competitors in this market was promoted by the expiration of Stratasys patents on the FDM process and by growing demand for customized products [34].

However, since developing appropriate binder systems for metal or ceramic powder is not a trivial task and the FFF process was protected by patents, this technology was neglected until recently. Lately, the interest in producing metallic or ceramic parts via MEAM was rejuvenated thanks to FFF machines which relies on an open-source technology accessible to almost everyone because very cheap [1].

Some limits in this process were found in the filament, often too straight, stiff, and not flexible enough to be spooled. A significant amount of porosity, printing defects, and delamination and cracking were also reported after debinding and sintering. Some later endeavours in the optimization of printing parameter optimization has been reported to decrease defects in the green parts. Although some understanding of the feedstock material properties for printing has been developed, the effect of processing and printing parameters on green part properties, sintered properties, and microstructure was absent in these earlier studies [27]

The most known metal FDM commercial machines currently available are supplied, as already mentioned, from Markforged (ADAM™) and Desktop Metal (BMD™) with a claimed capability to process 17-4PH, 316L, H13, A2, D2 tool steels, Cu, Inconel 625 alloy parts but since the deposition process is similar to the ordinary FFF, several small and medium companies are producing FFF machines such as German RepRap, MarkForged Inc., Hage Sondermaschinenbau GmbH & Co KG, Voxel8, Xery 3DRobox, Ultimaker, EVO-tech, Aleph Objects, MakerBot Systems, 3D Platform, Titan Robotics Ltd., Felix, Sharebot srl, 3D System Inc., BigRep GmbH, Printbot, Indmateg GmbH, Rokit Inc., Delta Micro Factory Corp., Prusa Printers, and Zortrax printers could potentially perform the metal FDM process [29] and furthermore, personal fabrication markets are being encouraged to create, upgrade and innovate with open source RepRap projects.

The scientific understanding of the materials and parameters at each step of the metal FDM process is still incomplete and not available in the open literature [27].

Since the metal FDM technology showed up in the 20th century, researchers have adopted different ways to improve the strength of parts but for a long time, research just focused all efforts on the process parameters like feed rate, speed, layer thickness, etc. regarding a single or few materials [2].

3.3. Benefits

Metal FDM can offer several advantages compared to existing metal AM processes in particular compared with the PBF processes and with traditional processes. The most remarkable benefit is given by the significantly lower capital costs [27]. Moreover, the absence of high rapid heating/cooling rates and directional heat extraction enables elimination of residual stresses, provide equiaxed grains and more isotropic microstructures and mechanical properties [27].

The powder used in the PBF technologies is difficult to handle but with the Metal FDM we have the elimination of handling loose powder during printing [27].

Since the binder is processed temperatures are lower than the temperatures employed in the PBF technology, it's possible to improved powder recyclability during net-shaping due to lower process temperatures at the green state [27]. At the beginning of this technology, first development of the D&S process were based on the prior knowledge of debinding and sintering knowledge from metal injection moulding [27].

Similarly to all the technologies that exploit powders, the Metal FDM offers the possibility to print non-weldable metals and brittle ceramics [27] and multi-material printing capability in one part [27].

Contrary to the popular PBF printers, the Metal FDM can potentially fabricate parts in space, where the use of other powder bed based AM processes poses serious powder and bed stability concerns [27].

In the end, the most relevant benefit that should encourage the spread of this technology is the technical simplicity and geometric accuracy offered by this technology[2].

3.4. Drawbacks

Here follows the limits of the metal FDM that somehow explain its limited diffusion and justify major enhancement and diffusion of the PBF technology.

The sintering process and environmental control of the process are crucial in the building of the effective microstructure, densification, no distortion, and required properties [27];

Again, the debinding process is remarkably challenging because affects the resulting microstructure. The presence of binder residues can severely prevent densification. Moreover, the shrinkage due to the D&S process is particularly challenging in parts that have high geometric complexity and plus, produced parts results dramatically brittle that the component could break during the handling [27].

The metal FDM micro-structure always exhibits voids and binder residuals that contribute to the vulnerability of the product resulting in lacks in mechanical properties [2].

The development of numerical simulation regarding the D&S process in metal FDM is insufficient. The development of specialized software for predicting the final component's size, residual stresses, and predicting ultimate mechanical characteristics for various metals would of course assist in the progress of metal FDM [9].

One way to encourage the diffusion of the technology would probably be by developing filaments, binders and powders easy to come by and cheap.

Main companies in this sector, such as Markforged and Desktop Metal, have not made adequate and significant development in this field because available information comes from the experience matured with metal injection moulding (MIM) dated back to about three decades ago [9]. Plus, binder composition should prevent the filament buckling associated to high viscosity in the hot end, which means that the achievement of high powder volume fractions is discouraged, but at the same time high powder loading enhances the chance of success and the microstructural quality of the final product [32].

Another problem is the poor promotion of this process in the applications such as the development of complicated forms, thin-walled components, and high-precision dimensions [9] that might bring in the spotlight this technology.

Section 4

4. Equipment and materials

In this chapter are introduced all the resources used in the study starting from the adopted spools up to the machineries used to perform tests and measurements.

4.1. Filaments

In this paragraph are introduced all spools of materials employed in the study with relative printing parameters and properties declared by the supplier companies.

4.1.1. Acrylester-Styrol-Acrylnitril (ASA)

The Acrylester-Styrol-Acrylnitril (ASA) filament manufactured by EVO tech, depicted in *Figure 30*, has been adopted as initial material to take confidence with the 3D Printer. According to the technical data sheet provided by EVO-tech, the ASA offers scratch-resistant surfaces and exhibits chemicals, weather and UV-light exposure resistant [46].



Figure 30. ASA filament spool by EVO-tech [46].

An important clarification to remark is that the filament was purchased in the 2017 and the possible ageing effect that could have affected the mechanical performance and adhesion of the material will be ignored.

The most relevant mechanical performances of the material, stated by the supplier company, are listed in the *Table 6*.

Properties	Test Condition	Test Method	Unit	Value
Tensile Strength	50mm/min	ASTM D638	kgf/cm ²	390
Tensile Elongation	50mm/min	ASTM D638	%	3,5
Flexural Modulus	1,3mm/min	ASTM D638	kgf/cm ²	18900
Flexural Strength	1,3mm/min	ASTM D638	kgf/cm ²	580
Izod Impact Strength	230C	ISO 180	kJ/m ²	25
Heat Distortion Temperature	1,82 Mpa	ISO 75-2	°C	74
Vicat Softening Temperature		ISO306	°C	100
Specific Gravity		ISO1183	g/cm ³	1,07
Shrinkage			%	0,5 - 0,7
MVR	2200C / 10.0 kg	ISO1133	g/10min	6

Table 6. Mechanical properties of ASA material by EVO-tech [46].

EVO-tech also supplies some printing parameters, listed in detail in Table 7.

<i>Parameter</i>	<i>Value recommended</i>
Nozzle Temperature	235 – 260 °C
Bed Temperature	90 – 100 °C
Print bed	EVO-tech Printbed
Length on Roll	290 m / 0,75 kg

Table 7. Recommended ASA print setting [46].

In the respective safety data sheet, the EVO tech declares that the filament extrusion has no hazardous effects on the human health and the environment [46].

4.1.2. ULTRAFUSE 316L

The 316L filament, depicted in Figure 31, is a 1.75 mm diameter filament. During the study, the filament was not dried, not subject to temperatures-controlled environments or moisture-controlled environments.



Figure 31. Ultrafuse 316L filament spool [47].

As stated by the BASF, in Table 8 some printing parameters recommended is listed.

<i>Parameter</i>	<i>Value recommended</i>
Nozzle Temperature	230 – 250 °C
Bed Temperature	90 – 120 °C
Nozzle Diameter Recommended	0,4 mm
Default Print Speed	35 mm/s
Extruder Multiplier	1,0 – 1,1
Extrusion Width	0,35 mm
Retraction Distance	5,0 mm
Retraction Speed	45 mm/s
Layer Height	0,15 mm
Outlines	1 – 2
Infill%	100
Infill Type	Grid rectangular
Outline Overlap %	100 %
Infill Extrusion Width	100 %
Cooling	No cooling

Table 8. Recommended 3D-Print processing parameters [48] [49].

Also according to the BASF, in *Table 9* a list of mechanical properties resulting from tensile tests conducted on the material according to the ISO 6892-1 (0,3 mm/min up to 2% and 10mm/min till the end of the test) and ISO 6507-1.

<i>Print direction</i>	<i>XY</i>	<i>ZX</i>
Tensile strength	561 MPa	521 MPa
Elongation at Break	53 %	36%
Yield Strength	251 MPa	234 MPa
Vickers Hardness HV10	128	128

Table 9. Mechanical properties of the ULTRAFUSE 316L [48].

Again, in *Table 9* it's evidenced the anisotropic behaviour of the material, a common feature in components manufactured via AM.

4.1.3. Titanium 64-5 Filamet™

The filament, shown in Figure 32, is 1.75 mm diameter wide. It has been manufactured by The Virtual Foundry, resold in Europe by the filament2print company.



Figure 32. Titanium 64-5 Filamet™ spool [50].

Since the diameter of the coil couldn't fit into the designed seat, it's been manually rewound on another coil with a smaller diameter able to fit inside the seat.

In *Table 10* are gathered the most important info supplied by The Virtual Foundry according to what they know so far.

<i>Parameter</i>	<i>Value recommended</i>
Nozzle Temperature	205 – 235 °C
Bed Temperature	40 – 50 °C
Nozzle Diameter	0,6 mm/Hardened Steel or stainless steel
Print Speed	60 mm/s
Sintering Temperature	1400 °C
Density	2,46 g/cm ³
Material Load by Mass	80%

Table 10. Printing and sintering parameters for Titanium 64-5 Filamet™ recommended by The Virtual Foundry [51].

According to the technical data sheet provided by the supplier company, mechanical properties are not available since the filament is still in development stage. In particular, the step regarding the sintering is critical because of the high chemical reactivity of the titanium with the oxygen, exacerbated by the temperature effect [52].

4.1.4. High-Impact Polystyrene (HIPS)

The spool of High Impact Polystyrene (HIPS) was supplied by the EVO tech. The HIPS is a polymer that dissolve in an organic solvent called d – Limonene or Orangeterpene. The filament was purchased in the 2017 and stored in a cardboard box.



Figure 33. HIPS spool by EVO-Tech [46].

HIPS filament is made of a polymer which has very similar properties of ABS, with regards to rigidity and impact resistance.

According to the EVO tech, the filament should be extruded at 210 – 240 °C on a heated bed at 90 – 100 °C [46].

4.2. Solvent agent

The solvent agent adopted to dissolve the HIPS support material is the d-Limonene, supplied by Vögele ingredients. The solvent, also known as +-limonene, r-+-limonene, +-4r-limonene, +-carvene, +-dipentene, citrene, +-p-mentha-1,8-diene, 4r-limonene, d-+-limonene [53] or Orangeterpene smells like orange and at room temperature is in liquid form. The liquid was purchased in 2017 and since the original plastic tank was warped, the liquid was moved into another carefully cleaned tank, as shown in *Figure 34*.

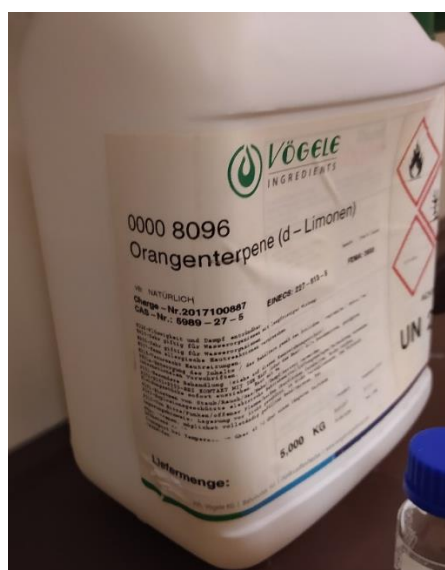


Figure 34. Replacement solvent tank.

The safety datasheet of the solvent was not provided by Vögele ingredients company. By means of the identification number of the chemical substance or Chemical Abstracts Service (CAS) number and European Inventory of Existing Chemical Substances (EINECS), respectively equal to 5989 – 27 – 5 and 227 – 813 – 5, an equivalent safety datasheet has been found by ThermoFisher Scientific.

The material is handled under hoof since the safety datasheet reports the following hazards:

- H226 - Flammable liquid and vapor.
- H315 - Causes skin irritation.
- H317 - May cause an allergic skin reaction.
- H410 - Very toxic to aquatic life with long lasting effects.
- H304 - May be fatal if swallowed and enters airways.

4.3. Filament pre-heater

As recommended by The Virtual Foundry, a pre-heater for the filament is needed to soften the filament since it's too brittle to pass through the Bowden tube. The device, depicted in *Figure 35*, is called "FilaWarmeris" and is designed to warm the filament up to 60 °C.



Figure 35. FilaWarmer [54].

With reference to the *Figure 36*, the FilaWarmer is placed nearby the output of the fixed feeder in order to soften it before passing through the Bowden tube.

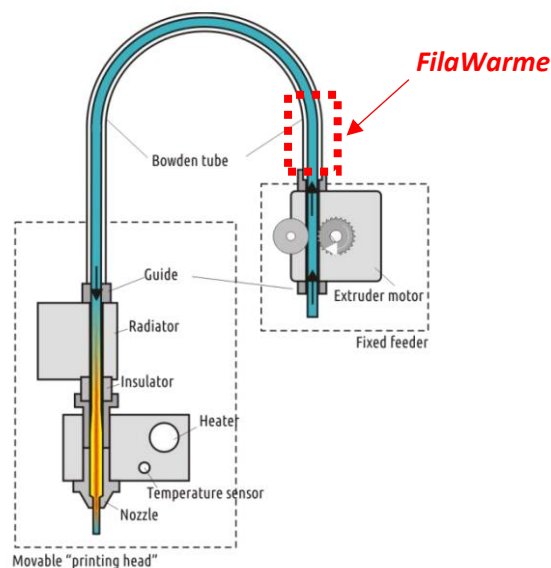


Figure 36. Setup of the FilaWarmer.

4.4. Metal FDM printer

The printer adopted in the study is an EVO-Lizer 11 model (*Center for Physics and Bio-medical engineering of the Medical University of Vienna*), provided by EVO-tech and shown in *Figure 37*.

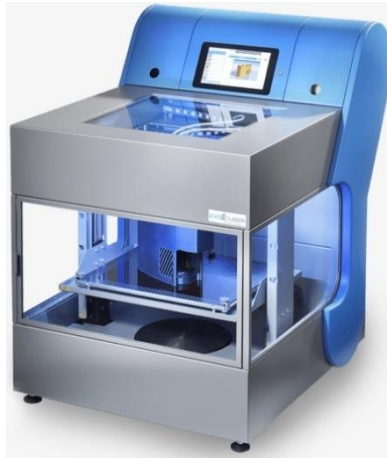


Figure 37. EVO-lizer 11 printer [55].

In the *Table 11* are listed all technical details of the printer model declared by the EVO-tech.

Feature	Value
Print area size (L x W x H)	270 x 195 x 205 mm
Minimum layer thickness	0,1 mm
Position accuracy	0,05 mm
Temperature range of the nozzle	160 – 260 °C High temperature 160 – 325 °C
Temperature range of the plate	30 – 100 °C
File formats	. STL – can be exported from any common CAD program
Average power consumption	250 W
Connection data	230 V AC; 50/60 Hz; 4 A
Average sound level	46 dbA

Table 11. Technical data of the EVO lizer 11 [56].

Since the building space is closed in a box, the heated bed can increase the room temperature in the box up to 50 °C when powered-on for long enough time.

The printer mounts a dual Bowden extrusion system. Moreover, the two extruders have fixed positions respect to the carriage system, as depicted in

Figure 38.



Figure 38. EVO-lizer 11 printer head with nozzles [57].

The support material is extruded through a 0,4 mm diameter brass nozzle while for the extrusion of the feedstocks we need to adopt a different material to reduce the abrasive effect of the metal powders, depicted in *Figure 39*.

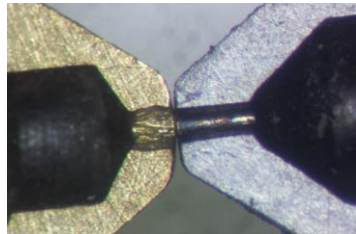


Figure 39. Comparison of wear resistance between a brass and a steel nozzle [58].

Hence, as recommended by the filament supplier company, a 0,4 mm diameter steel nozzle has been adopted to extrude ULTRAFUSE 316L and 0,6 mm diameter steel nozzle to process Ti6Al4V. All nozzles have been purchased by EVO-tech.

The only cooling device embedded in the printer is a fan underneath the heated bed to speed up the cool down time of the bed. All temperatures are controlled through a PID control.

The adopted plate is a 346 x 286 x 2 mm Carbon Fibre Reinforced Plastic (CFRP) panel. On the panel, is placed an adhesive film to enhance the adhesion of the material.

As depicted in *Figure 40*, in the left housing of the printer will be hosted the part material while the right housing will host the support material.

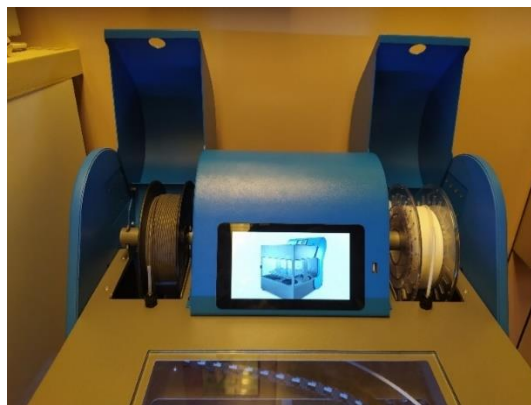


Figure 40. Housing for the filaments.

4.5. Slicer software

The slicer software adopted in the current study is Simplify3D V4 (Licence Version 4.1.2), a software responsible for the generation of a G-code suitable for FFF printers. The user interface, shown in the *Figure 41*, make it possible to have a close look to the virtual simulation of the working space and making it easier to set and adjust all parameters of the process.

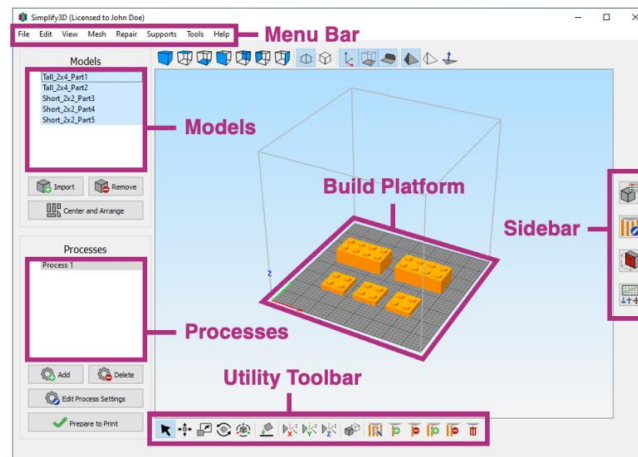


Figure 41. Simplify3D User Interface.

In the Models panel it is possible to insert objects in STL format and shift them, orient them on the building platform or reshape it by means of the Utility Toolbar.

All process settings and information regarding the printer hardware e.g. printer working space and type of kinematic motion are stored in the so called “Profiles”.

In Simplify3D it is possible to assign different Profiles to different object present on the Build Platform, but also assign distinct Profiles to certain regions of the same object. When a Profile is assigned to a certain object or region of object by defining the starting and finish height level, it's called “Process” and it appears in the Processes Panel shown in *Figure 41*.

Profiles can be imported or exported as FFF files. In the current study, the benchmark Profiles employed are “EL-11 Breakaway V1.2.fff” and “EL-11 Dual Soluble V1.2.fff” downloaded by the official EVO-Tech website [59].

The “EL-11 Breakaway V1.2” file contains parameters useful to manufacture the following materials with a single-extruder FFF process: ABS EVO-tech, ABS-ESD EVO-tech, ABS-FR EVO-tech, ASA EVO-tech, HIPS EVO-tech, SUPP EVO-tech, IGUS I180, IGUS I150, PETG EVO-tech, PPS EVO-tech, PLA EVO-tech, PC-ABS Evo-tech, PACF EVO-tech, TPE EVO-tech, FMP EVO-tech and BDP EVO-tech.

The “EL-11 Dual Soluble V1.2” file contains parameters to manufacture the following materials with a double-extruder FFF process: ABS EVO-tech, ABS-ESD EVO-tech, ABS-FR EVO-tech, ASA EVO-tech, HIPS EVO-tech, SUPP EVO-tech, IGUS I180, IGUS I150, PETG EVO-tech, PPS EVO-tech, PLA EVO-tech, PC-ABS Evo-tech, PACF EVO-tech, TPE EVO-tech, FMP EVO-tech and BDP EVO-tech.

Virtually, all set profiles should have been already optimized but actually they need to be adjusted anyway because the printer was stopped for a long time and some ageing effect on kinematic mechanisms may have happened.

Net of some parameters that during the activity have been changed frequently, we'll mention in next chapters all parameter adjusted during the experimental campaign in order to achieve the best result. All

non-mentioned parameters must be considered as the same contained in the “EL-11 Breakaway V1.2” Profile.

4.6. Tensile test machine

The machine adopted to perform the tensile test on the sintered samples is the Fatigue Testing System Instron 8801 (*Department of Mechanical and Aerospace Engineering of the Polytechnical University of Turin*), a general-purpose hydraulic fatigue depicted in *Figure 42*.



Figure 42. Instron 8801 system [60].

Main features of the testing machine are reported in *Table 12*.

Feature	Value
Load cell capacity	± 100 kN
Static load capacity	± 100 kN
Total actuator stroke	150 mm
Dynamic load capacity	± 50 kN
Hydraulic pressure supply	207 bar
Frame stiffness	390 kN/mm
Frame weight	625 kg

Table 12. Instron 8801 features [60].

The testing machine is equipped with the 2743-401 Universal Hydraulic Wedge Action Grips whose features are reported in Table 13.

Feature	Value
Dynamic load capacity	100 kN
Static load capacity	130 kN
Hydraulic pressure range	0 to 207 bar
Maximum gripping force	195 kN
Operating principle	Double acting piston, Wedge
Weight (Per grip, without Jaw Faces)	33 kg

Table 13. 2743-401 grips features [61].

The user interface software employed to monitoring and the acquisition of the force signal and the strain signal is Bluehill® Central.

4.7. CAD Software

All CAD shown in this study have been developed by means of SOLIDWORKS 2021 (Dassault Systemes, USA).

4.8. Measurement instruments

4.8.1. Calliper

The adopted calliper, shown in *Figure 43*, is a digital vernier calliper by Helios with a resolution of 0,01 mm with a measuring range of 0 – 150 mm and an accuracy of $\pm 0,02$ mm.



Figure 43. Front and back view of the digital calliper.

4.8.2. Micrometer

The adopted micrometer is a digital micrometer by Mitutoyo with a resolution of 0,001 mm and a measuring range of 0 – 25 mm.



Figure 44. Front and back view of the micrometer.

4.8.3. Microscope

The KEYENCE VR-5000, a non-contact 3D measurement system depicted in Figure 45, was adopted to measure geometrical features of shrinkage specimens and develop some in-depth considerations about the infill quality and lateral surface.



Figure 45. KEYENCE VR-5000 microscope [62].

4.9. SLM printer

All specimens printed to represent the L-PBF technology will be performed with the printer model SLM 125 by SLM Solutions and depicted in Figure 46.



Figure 46. L-PBF printer model SLM 125 by SLM Solutions [63].

Some features of this printer, declared by the SLM Solutions company, are listed in *Table 14*. It's important to see that the build volume is extremely reduced by the bulk of the plate. Compared to the declared build volume, the actual building volume (L x W x H) is around 80 x 80 x 80 mm.

Feature	Description
Build Envelope (L x W x H)	125 x 125 x 125 mm reduced by substrate plate thickness
Build Volume Reduction (L x W x H)	50 x 50 x 50 mm reduced by substrate plate thickness
3D Optics Configuration	Single (1x 400 W) IPG fiber laser
Real Build Rate	up to 25 cm ³ /h
Variable Layer Thickness	20 μm - 75 μm, more available on request
Minimum Feature Size	140 μm
Beam Focus Diameter	70 μm - 100 μm
Maximum Scan Speed	10 m/s
Average Inert Gas Consumption in Process	0.6 l/min (Argon)
Average Inert Gas Consumption in Purging	70 l/min (Argon)
E-Connection / Power Input	400 Volt 3NPE, 32 A, 50/60 Hz, 3 kW
Compressed Air Requirement	ISO 8573-1:2010 [1:4:1] 7 bar
Machine Dimensions (L x W x H)	1400 mm x 900 mm x 2460 mm

Table 14. Technical specifications of the SLM 125 printer [64].

According to the technical datasheet, this machine can process stainless steel, cobalt-chrome, nickel alloys, aluminum and titanium powders. Both reactive and non-reactive metals can be processed in the standard SLM®125 configuration [64].

Section 5

5. Methods

In this chapter, it will be discussed the roadmap followed to achieve the goal of printing the tensile test specimens of ULTRAFUSE 316L and the shrinkage specimens of the Titanium filament. All the preliminary activity is described, and all the tests made during the optimization of the process parameters will be shown and discussed. An accurate description about all geometrical details regarding the specimens is also included.

5.1. Preliminary activity

At the beginning of the study there were no previous experiences with this technique. Thus, it was decided to gain technical expertise. The starting point was the extrusion of the ASA with a simple mono-extrusion process, then the extrusion process of the ASA turned into a dual-extrusion with the HIPS as support material. In the end, the ULTRAFUSE 316L replaced the ASA in the role of part material. In this way, the required knowledge was achieved through a step-by-step approach. At the end of the section, all the most relevant challenges faced during the printing will be discussed.

5.1.1. Mono-extrusion polymer practice

Test 1-Practice test

The very first print performed is a little cross, whose sizes are reported in *Figure 47*.

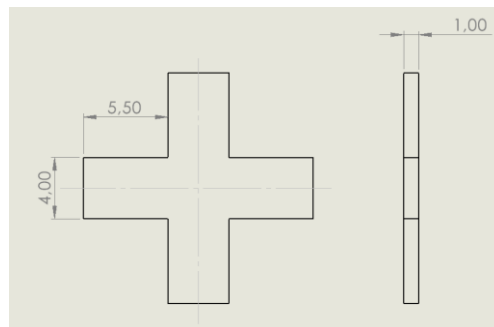


Figure 47. Geometrical features of the cross.

The reason of this print was the evaluation of possible malfunction of the printer. The shape of the cross can help to see how actuators behave when they have to perform short movements. All parameter settings are insert as default parameters contained in the Process “EL-11 Breakaway V1.2.fff”.

The slicer software allows to include additional rafts, and the brim structures, depicted in *Figure 48* and respectively coloured in pink and purple, are involved to help the adhesion of the first layer.

The raft is usually adopted to enhance the stability of the first layer in small prints while the brim aims to enhance the adhesion of the first layer, especially for large prints, by securing the perimeter of the print to the bed.

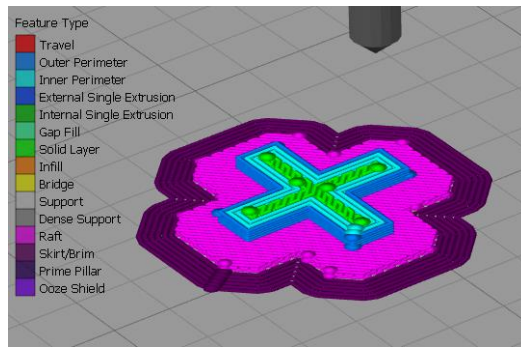


Figure 48. Preview of the print features of the cross.

The result of the print, shown in *Figure 49*, remarks a poor top layer quality.



Figure 49. The result of the print, whose brim and raft were removed, compared with a coin.

Test 2-Lateral surface test

After this trial, the next step is the printing of a 1 cm-sided cube to check the lateral surface quality and the geometrical accuracy. As in the first test, the printing parameters are set as default and the brim structure is adopted to enhance the adhesion of the first layer (*Figure 50*).

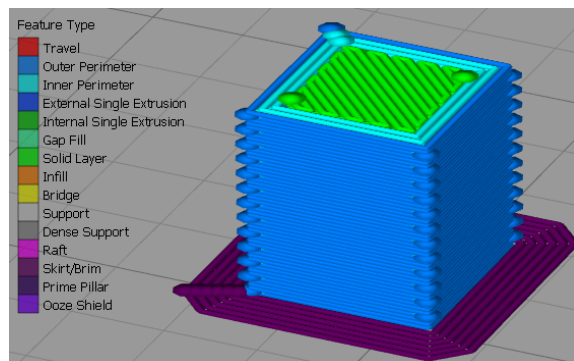


Figure 50. Preview of the print features of the cube.

The resulting lateral surface is quite satisfying, and the top layer, depicted in *Figure 51*, shows the same roughness seen in the cross. Anyway, the actual dimensions of the cube are equal to 10,3x10,2x10,1 mm (x, y, z).



Figure 51. The cube and cross compared with a coin.

The geometrical evaluation highlights that the thermal shrinkage has a minimum effect on the print since the sizes are slightly bigger than expected. This result could be justified by the settings of the flow rate that may have made the raster wider than expected or may be due to a bad placement of the measuring device during the acquisition.

Test 3-First layer test

Considering the importance of the first layer during the print of the cross and the cube, it was decided to perform a test aiming to enhance the adhesion of the first layer.

The test requires that two crosses provided with raft and brim are printed once at a time. The only parameter that will be changed is the gap between the nozzle tip and the bed in order to assess qualitatively the magnitude on the first layer quality. The result is depicted in *Figure 52*, and remarks that the specimen “-0,1” exhibits a better overlapping between the rasters compared with the “+0,1” specimen. Further discussion about this parameter is given in the *Gap between the nozzle tip and printing bed* at page 106.



Figure 52. First layer quality comparison and dimensional comparison with a coin.

5.1.2. Double-extrusion polymer practice

Test 1-Hotend Offset calibration

The combine use of multiple extruders is particularly challenging to manage because several measures shall be adopted to avoid print to fail. One of the possible sources of error is a bad setting of the hotend offset that is the distance between the nozzles. The most severe consequence of a bad setting of this parameter is the wrong positioning of the deposited material.

The detection of such problem is proposed by a pre-set gcode file able to prints a thin-walled structure, first with an extruder, then print the same structure on the top of the existing one, with the other extruder. The result of such print is depicted in Figure 53 and shows that the set hotend offset is not correct resulting in the mismatching of the prints.

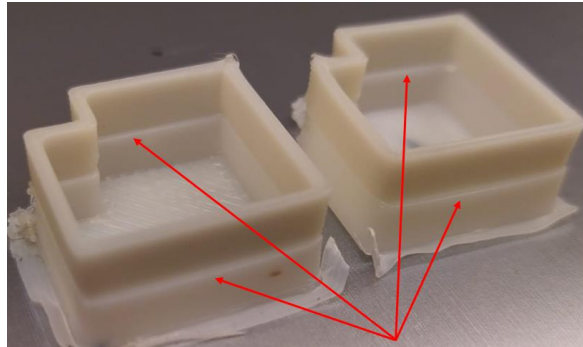


Figure 53. Result of the hotend offset calibration test with remarkable misalignment of the consecutive prints.

This parameter can be easily manipulated through the Web Interface. This page is accessible via PC, with a LAN or Wi-Fi connection with the printer, whose user interface is displayed in Figure 54 (a). The current hotend offset can be seen by entering the line “M218”.

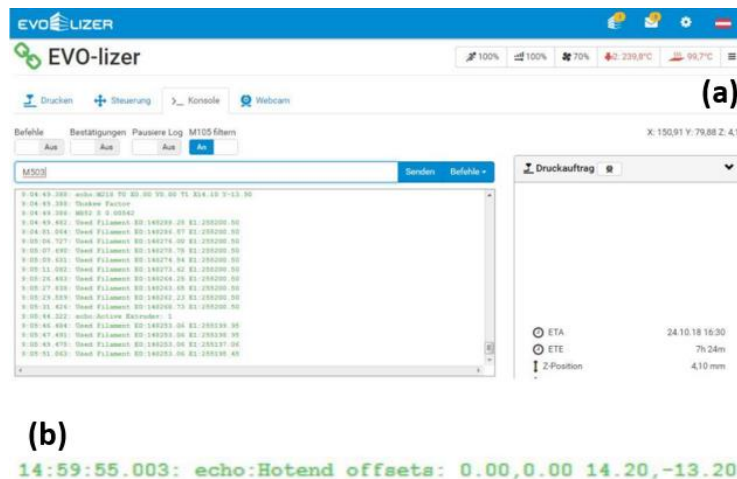


Figure 54. (a) Console in the web interface, (b) console response to the “M218” command.

The console will answer back with a line similar to that shown in Figure 54 (b) in which the 14.20 value means the Cartesian coordinate x of the shift of the second extruder from the first while the -13.20 value represents the one on the y axis.

The hotend offset can be fixed by entering the string line “M218 T1 X xx.xx Y yy.yy” where xx.xx and yy.yy are the new correct values.

After some trials, the misalignment was almost totally removed, as reported in the Figure 55.

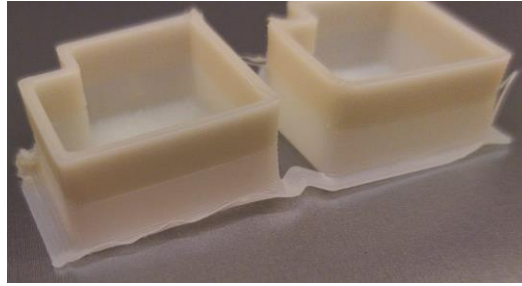


Figure 55. Result of the hotend offset adjustment with lower misalignment.

Test 2-Interaction test

Subsequently, a test was performed to evaluate the interaction between the ASA and the HIPS. The test, depicted in *Figure 56*, consists in the printing of a cube with 20 mm side made in ASA leaning on a raft structure made in HIPS.

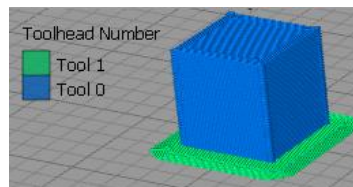


Figure 56. Preview of the adhesion test with a cube of 20 mm side.

The result, discussed in detail below, is depicted in *Figure 57* .

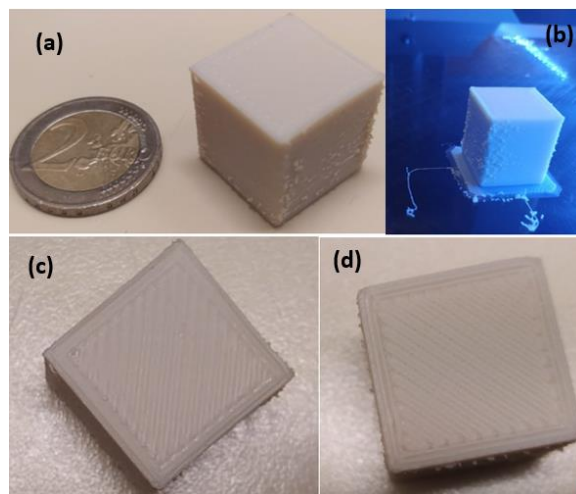


Figure 57. Adhesion test result: (a) dimensional comparison with a coin, (b) oozing defect on lateral surface, (c), top face, (d) bottom face.

The *Figure 57 (a)* and *Figure 57 (b)* show the “oozing”, an effect due to the dripping of the melt material from the extruder due to gravity and residual pressure. The top layer is fully dense and exhibits a satisfying quality, as shown in the *Figure 57 (c)*. The adhesion performed between the ASA and the HIPS is fine and make it is possible to easily peel off the raft made with HIPS without excessive effort. Contrary the top layer, the bottom layer shows visible raster gaps, remarking that the infill in the layer is not constant. This effect can be explained by the needing for a transient time to get into a steady pressure condition in the melting chamber of the hotend, necessary to achieve a homogeneous raster width. This observation leads to the conclusion that the parameters used for the bottom layer may possibly be different from the other in order to get the same infill in the bottom and in the top layers.

The dimensions of the cube recorded with the calliper are 20.14 x 20.05 x 19.94 mm (x,y,z). Contrary to the cube with a 1-mm side, in this case the height is shorter than the expected height while in the xy plane the actual dimensions are greater than the ideal ones.

Several solutions to this problem may be adopted e.g. the turning off of the support material extruder when the deposition of the raft is over. If it's needed that the support material run in combination with the part material extruder, then we can adopt the oozing shield, an additional structure that consists in a wall printed nearby and around the print that is able to stick all the blobs on the wall sparing the surface of the print.

Test 3-Stringing and raft test

The next test aims to spot possible “stringing effects”. The stringing is a kind of the defect that happens when during the deposition, the extruder is at rest for short time resulting in the production of a thin thread like a spider web. This effect can be detected with the well-known “Dual towers test”.



Figure 58. Dual towers test model [65].

Since the model is quite small, we take advantage of this test to understand the impact of the raft structure on a small print since this kind of additional structure is recommended for such conditions.

Thus, the print will be performed with and without the raft structure according to the models depicted in Figure 59.

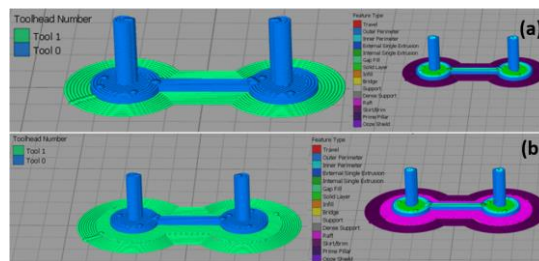


Figure 59. Dual towers test previews: (a) without raft structure, (b) with raft structure.

Both prints have been ran with the default parameters. The result, depicted in Figure 60 (a), shows that the raft has a remarkably beneficial effect on the bottom layer with a consequent repercussion on the overall quality of the print.

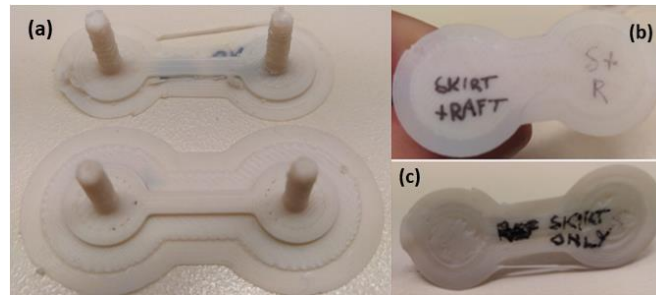


Figure 60. Results of the test: (a) comparison of the dual towers test, (b) first layer of the dual tower test with raft, (c) first layer of the dual tower raft without raft.

The comparison between the first layer quality of the two prints highlights the effectiveness of the raft structure. The raft structure used in Figure 60 (b), helped in achieve a smooth layer while the result achieved without raft, in the Figure 60 (c), shows warpages and bad infill of the bottom layer.

Test 4-Tensile specimens test

The last test will be a simulation of the print process of the tensile specimens. In Figure 61 are shown all sizes of the tensile specimen adopted which whom refer to the DIN 50125 E-type, the standard adopted in the technical datasheet of the ULTRAFUSE 316L filament.

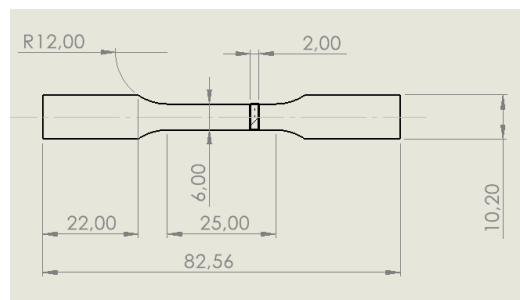


Figure 61. DIN 50125 E-type tensile specimen sizes.

The print of the tensile specimen was performed with default printing parameters. Consideration about previous test are putted in practice; thus, the tensile test specimen was printed with the adjunction of a raft structure and an oozing shield used as a functional skirt structure. The first trial, defined as “Trial 0”, is depicted in Figure 62.



Figure 62. Tensile test specimen with default parameters: (a) bottom view, (b) top view.

In particular, the bottom layer, depicted in the Figure 62 (a), shows pores on the interface between the peripheral rasters and the infill. On the other hand, the top view displayed in Figure 62 (b) shows a good quality free from pores and holes. The print underlines, together with the previous cube test, the needing to diversify the printing parameters adopted in the bottom layers and in the following layers to solve the presence of voids.

The optimization process of the bottom layer was performed through a trial-and-error approach with the goal to maximize the infill rate. Since the goal is to optimize the bottom layer, after the deposition of some bottom layers, the print was stopped. The optimization process took ten trials, displayed in Figure 63 (a), while in Figure 63 (b) is shown the final result achieved.

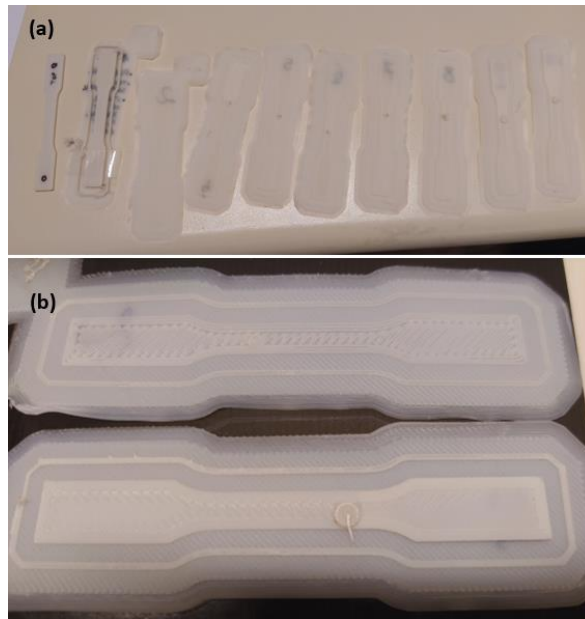


Figure 63. Bottom layer parameters optimization process: (a) all trials, (b) comparison between the first and last trial.

For simplicity, all intermediate steps in the optimization process will be neglected and a list containing all parameters who affected the bottom layer will be listed in Table 15.

Print parameter	Trial 0 (Default parameter)	Trial 10 (Maximized infill)	How it is involved
Nozzle diameter	0,4 mm	0,3 mm	The nozzle diameter, in combination with the default printing speed, influence the movement speed and the width of the raster since the slicer software assume a certain nozzle diameter even though it may be different from the actual one.
Extrusion Multiplier (T0)	1,00	1,50	It is a ratio referred to the nominal Flow rate, used to modify the amount of deposited material by changing the speed of the feeding stepper motor. This value changes the actual extrusion width value.
Extrusion Width	Auto	0,60 mm	It is the raster width assumed by the slicer software to evaluate the strategy of deposition; thus, it can affect the actual infill rate.
Retraction Distance	6,00 mm	5,00 mm	During the resting of the nozzle, the slicer software allows to retrieve the filament in order to reduce or cancel the oozing effect.
Extrusion Multiplier (T1)	1,00	0,98	
Primary Layer Height	0,2 mm	0,15 mm	This is the height of the layers that results in the movement of the z-axes actuators. In combination with

			the Extrusion width and the Extrusion multiplier, this parameter can affect the lateral surface quality.
Outline Direction	Inside-Out	Outside-In	The deposition strategy of the perimeter rafts can positively affect the surface quality or the overlapping between the perimeter and infill rasters.
Interior Fill Percentage	25 %	100%	This percentage, expressed in relation to the extrusion width, defined between 0 and 100, affects the raster air gap in the infill since with high percentage we can achieve a bulk component.
Outline Overlap	10 %	90 %	This parameter decides the magnitude of the overlaying of the infill on the outline perimeters.
Extruder 1 Temperature	250 °C	260 °C	The temperature affects on the viscosity of the melt filament and plays a role in the adhesion properties of the material. At the same time, high temperature results in higher risk of material degradation, oozing and possible warpages.

Table 15. Changed print parameters to maximization of the bottom layer infill.

After the bottom layer optimization, an attempt to print all the specimen with the process who maximizes the infill of the bottom layer was made but the result defined as “Trial 11” and shown in Figure 64 (a) remarks a bad surface quality and consequent poor geometrical accuracy of the thickness.



Figure 64. Print parameters optimization process: (a) top view of the trial 11, (b) top view of the trial 19.

The slicer software allows to assign a particular process for specific layers by using the “variable setting wizard”. Thus, the *Process* that enhance the bottom layer will be applied to the first layer and a new *Process* will be developed leading to the top surface depicted in Figure 64 (b). All parameter differing from the previous parameter settings are listed in Table 16.

Print parameter	Trial 11	Trial 19
Nozzle diameter	0,3 mm	0,4 mm
Extrusion Multiplier (T0)	1,50	1,00
Extrusion Width	0,60 mm	Auto
Retraction Distance	5,00 mm	6,00 mm
Outline Direction	Outside-In	Inside-Out
Outline Overlap	90 %	10 %

Table 16. Changed print parameters to maximization of the top layer quality surface.

The same kind of approach was adopted to optimize parameters with specimens aligned to the z-axes but, as displayed in Figure 65, the printing of slender structures is a difficult task with the ASA. Moreover, in

Figure 65 specimens marked as “9” and “10” were printed using the support material like a scaffold but the problem persisted.

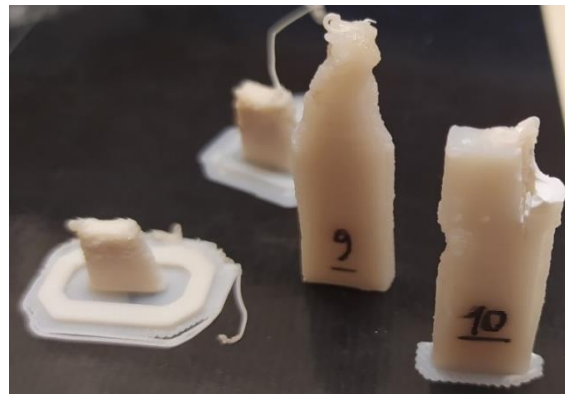


Figure 65. Failed trials in the parameter optimization process of specimens oriented on the z-axes.

The only successful test is the eleventh trial, shown in Figure 66. Thanks to the massive use of support material as a scaffold surrounding the structure, shown in the cross-section of Figure 66(a), it was possible to achieve the resulting print displayed in Figure 66(b). The main drawback of this strategy is the needing to dissolve the HIPS with a bath in the d-limonene for long time, given that the mechanical removal of the HIPS results difficult.

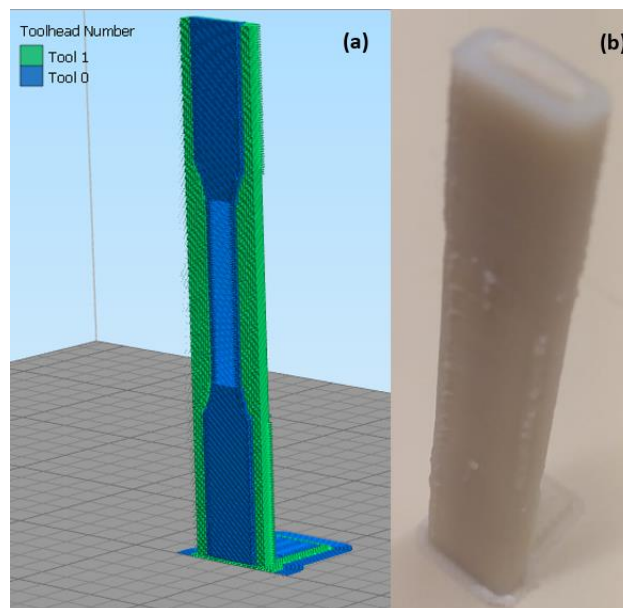


Figure 66. Eleventh trial: (a) cross-section of the preview of the print, (b) result of the print.

Anyway, after the support material removal by means of the d-limonene, the component was weak due to the delamination problems caused by the prolonged exposure to the solvent. This topic will be discussed later in the paragraph “Print exposure to the solvent (Page 106). A possible solution to this problem is the adoption of an ultrasonic cleaner, able to speed up the deterioration of the HIPS and so reducing the exposure to the solvent. Of course, the purchase of such device can be justified only if this issue occurs also in the metal feedstock prints.

5.1.3. Double-extrusion metal feedstock practice

In this subparagraph, the part material used will be the ULTRAFUSE 316L. The first trial is performed with all default parameters, plus the modifications recommended by the BASF company previously reported in *Table 8*.

Test 1-Temperature test

The first test aims to investigate the temperature effect in order to set the most suitable temperature to adopt in the deposition of the bottom layer. The temperature range chosen in the evaluation is the one recommended in the technical datasheet of the steel feedstock. The test setup is explained in the *Figure 67* and it is performed by printing all the crosses once at a time with a “object-to-object” strategy.

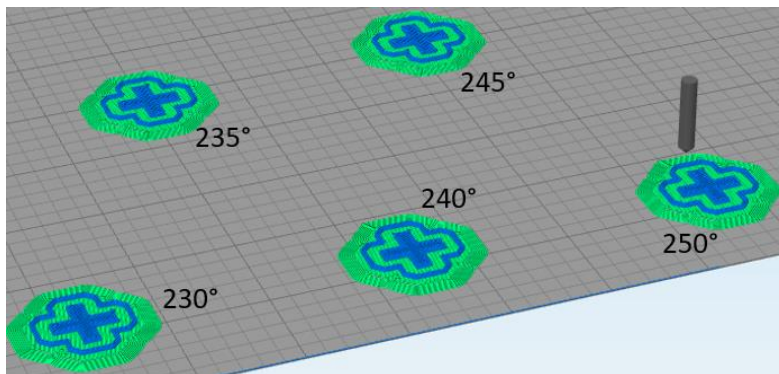


Figure 67. Bottom layer temperature test layout.

The result of the print, shown in *Figure 68*, is misleading because the best bottom quality is associated with the specimen printed with 235° and 245°, while in the case of the specimens printed with 230°, 240° and 250° there are visible air gaps. The two prints that show the best quality were in the inner part of the heated bed and this may have had an influence on the end result.

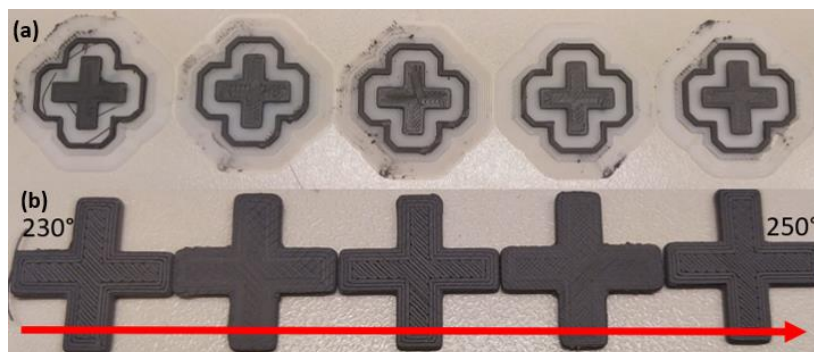


Figure 68. Result of the first print.

After the re-adjustment of the heated bed, the test was run again (*Figure 69*) and the result was more homogeneous, but some sign of the misalignment was still evident.



Figure 69. Second attempt of the temperature bottom layer calibration.

This experiment confirms that so far it was not possible to adjust the bed. The choice of the best printing temperature didn't succeed, so the temperature effect will be assessed in a different way.

In the next attempt, the temperature effect will be assessed with a new pattern. Contrary to the cross, the cube model gives supplementary information on the expected surface quality.

Given that the bed is not perfectly aligned, all cubes will be printed once at a time in the centre of the bed.

Figure 70 (a) shows that all prints exhibit periodical stripes, no matter the temperature.

Again, in Figure 70 (a) and mostly in Figure 70 (b) it's shown that temperature higher than 240° leads to the loss in the quality of the surface of the print. However, the best performance is detected in specimens at 230° and 235°.

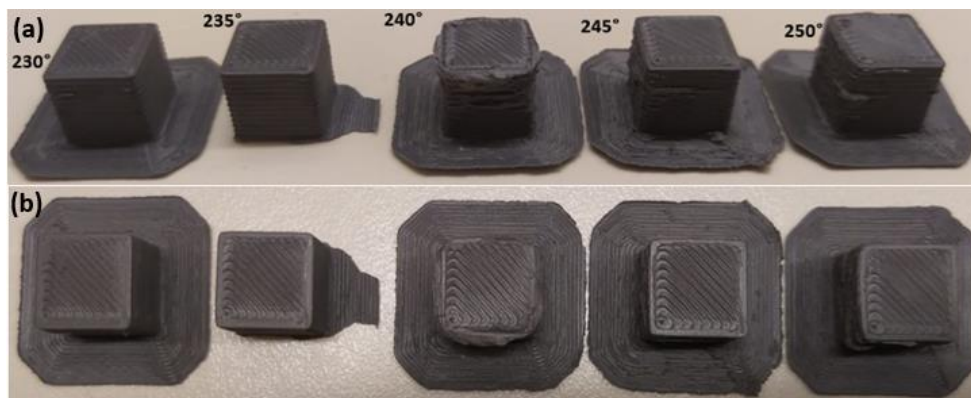


Figure 70. Temperature calibration with cube models: (a) lateral view; (b) top view.

In order to be able to obtain a print free of stripe marks, the next test will investigate the influence of the layer height on the presence of stripes.

Test 2-Layer height test

The new test consists in a tower test in which the layer height is progressively increased as displayed in Figure 71 (a).

In the tower test is exploited a thumb rule that wants the layer height to be ranging from the 25% up to the 75% of the nozzle diameter [66]. The result of the print, shown in Figure 71 (b), underlines that the maximum layer height usable is 0,2 mm and remarks that the layer height doesn't affect the presence of stripes.

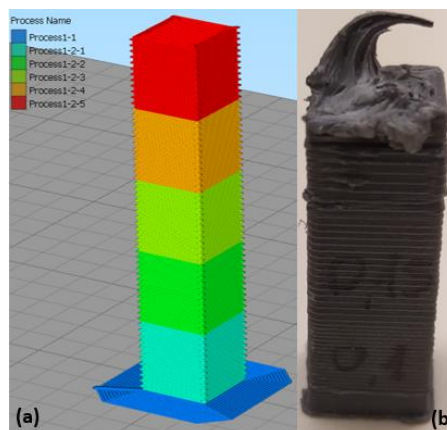


Figure 71. Tower test: (a) preview with all processes marked; (b) print result.

From a detailed analysis about all parameters configured, it was possible to see that the nozzle diameter was wrongly set as 0,3 mm while the actual nozzle diameter is 0,4 mm.

Test 3-Flow rate test

The last test performed will aim to detect the influence of the Extruder Multiplier and the Outline Direction.

The Extruder Multiplier is a parameter expressed as the ratio between the performed extrusion flow rate and the nominal flow rate. Practically speaking, this parameter increases or decreases the number of steps per minute provided by the stepper motor in the feeding system.

The Outline Direction is meant as the sequence adopted to print the perimeter loops. By selecting the “Outside – Inside” strategy, the first loop printed at all is the external loop, sequent all the internal perimeter loops and at the end the infill. In the end, with the “Inside – Outside” strategy, the external loop is the last perimeter loop printed before the print of the infill.

The *Figure 72* shows that the Outline Direction has no effects on the surface quality of the print. Nevertheless, the Extruder Multiplier results to have a strong impact on the surface quality. During the deposition process, it has been observed that with low Extruder Multiplier values the raster air gap was more marked. In conclusion, even though the quality surface with the 0,9 is the best, the adopted Extruder Multiplier will be 0,95 since it is more effective at filling voids.

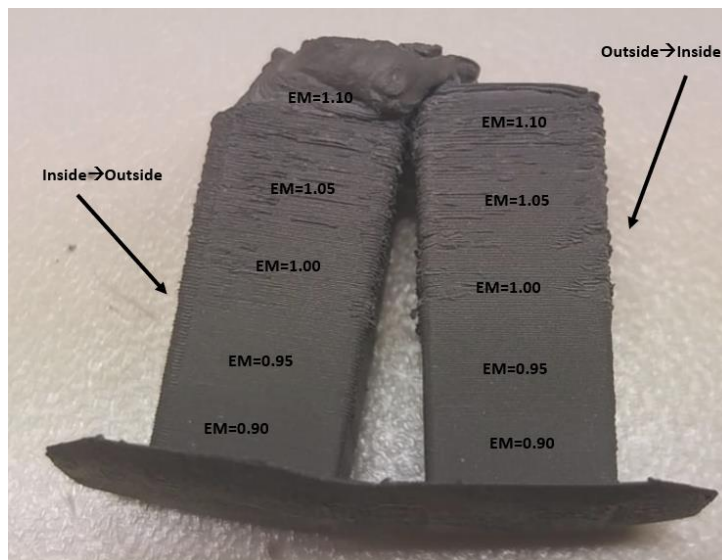


Figure 72. Dual tower test print result.

5.2. Tensile test specimen design

In this paragraph, all the features concerning the design and the manufacturing of the tensile test specimen will be discussed.

In order to get familiar with the tensile tests regarding this technology, the tensile test will be performed on specimens oriented in three different directions. The assesment of the tensile strengths on different orientation will be useful to provide us information on the magnitude of the anisotropy of the material, an information that may be spent in the computing of FEM simulation software for future applications.

5.2.1. Tensile test standard references

In literature and in technical datasheet of feedstocks, the tensile test standard adopted is not unique. Anyway, the most usual standards adopted detected are the ISO and the ASTM normative which rely on standards developed for materials machined with traditional techniques.

Mentioned standards don't indicate a unique geometry but they give some recommendation about maximum or minimum limits about geometrical features. Thus, to pursue the goal of making a sample comparable with more datasheet and scientific papers as possible, a superposition of constraints of the two regulations has been done to produce a sample with geometrical features adequate for both the standards.

The dog-bone shape is adopted because it's easier to perform the print on all axes without overhanging-related problems.

The first comparison of the manufactured specimens will be done with tensile test specimens manufactured via SLM and here comes the first constraint. The maximum length allowed for the specimen that can't exceed 115 mm since the volume of the working space of the SLM machine is 115 x 115 x 115 mm³, hence the maximum size must be less than 115 mm.

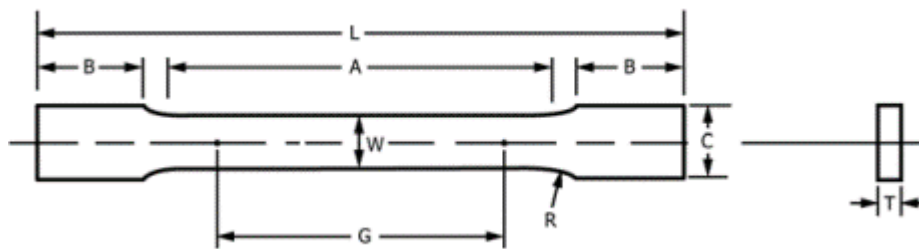


Figure 73. Geometrical dimensions of tensile test specimen identified by letters [67].

By referring to the geometrical features defined in *Figure 73*, in *Table 17* are collected all the constraint found in the ASTM E8/E8M-22 [67] regarding the rectangular tension test sub-sized specimens.

Constraint	Kind of constraint	Value [mm]
T – Thickness	≤	6
R – Radius of fillet	≥	6
C – Width of grip section	≈	10
A – Length of reduced parallel section	≥	32
G – Gauge length	=	25
W – Width	=	6
L – Overall length	≥	100
B - Length of grip section	≥	30

Table 17. ASTM E8/E8M-22 constraints.

In *Table 18* are shown, again referring to *Figure 73*, all constraints concerning non-proportional test pieces stated in the ISO 6892-1:2019(E) Annex B [68] that deals with sheets, strips, and flats between 0,1 mm and 3 mm thick.

Constraint	Kind of constraint	Value [mm]
-------------------	---------------------------	-------------------

T – Thickness	≤	3
R – Radius	≥	20
C – Ends width	≥	1,2·W
A – Parallel length	≥	G+2W

Table 18. ISO 6892-1 Annex B constraints.

The ISO 6892-1 shows some widely geometries exploited but, as done in the study of P.Morais et al. [69], it's possible to adopt smaller geometries than the one recommended by paying attention to maintaining the ratio between G and W as near to 4 as possible.

In the end, by fitting all constraints as done in *Table 19*, it's possible to get all constraints that the specimen should respect.

Constraint	Kind of constraint	Value [mm]	Dominant constraint
T – Thickness	≤	3	ISO 6892-1:2019(E)
R – Radius of fillet	≥	20	ISO 6892-1:2019(E)
C – Width of grip section	≈	10	ASTM E8/E8M-22
A – Length of reduced parallel section	≥	37	ISO 6892-1:2019(E)
G – Gauge length	=	25	ASTM E8/E8M-22
W – Width	=	6	ASTM E8/E8M-22
L – Overall length	between	[110,115]	ASTM E8/E8M-22 & SLM working space
B - Length of grip section	≥	30	ASTM E8/E8M-22

Table 19. List of all considered constraints.

The definitive geometry with respective sizes is depicted in *Figure 74*.

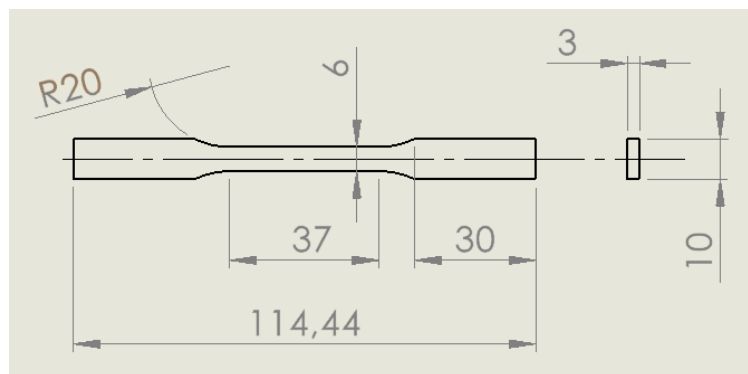


Figure 74. Geometrical features of the tensile test specimen.

5.2.2. Gripping area design

The debinding and sintering process is extremely complex and expensive and is convenient only with batches. Every effort during the design of the geometry must be done to avoid wasting material and repeating it.

During the tensile test, it may happen that the specimen slips between the clamps because the gripping area is not sufficient. Given the low availability of the material, if we consider the case of the print of tensile

specimens made via Metal FDM, this scenario is unacceptable. This concern led to the evaluation of the possible adjoint of supplementary area to the existing gripping area of the tensile specimen.

The solution to actuate this evaluation consists in printing some tensile specimens with the L-PBF technology. Two specimens will be printed with the nominal gripping area and other two with the modified gripping area. The base idea is that mechanical strength of components made via L-PBF as build is higher than the one manufactured via Metal FDM. Thus, if the specimens with the nominal gripping area don't slip, we can proceed and print tensile specimens with the Metal FDM.

To enhance the gripping area, the width of the gripping area was increased by paying attention that fillet radius should remain the same, otherwise it would change the stress distribution with consequent alteration of the test condition.

Practically, the enhancement was performed by extending the fitting radius to reach a width of the gripping area of 20 mm, shown in *Figure 75*.

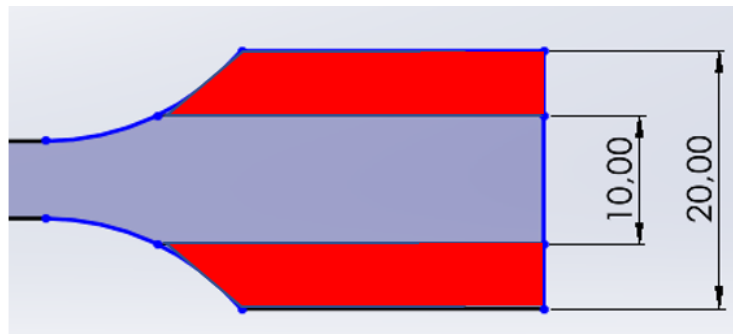


Figure 75. Increase of gripping area highlighted in red.

For logistic problems related to the printability of the samples with the L-PBF printer, only two specimens with the enhanced gripping area were printed.

5.2.3. *Debinding shrinkage compensation*

During the debinding, the component experiences a severe shrinkage due to the removal of the polymer binder. The shrinkage, mathematical defined in the Eq. (1), should be kept in account in the design of the gcode file by increasing the actual dimensions of the component.

$$S = 1 - \frac{L_s}{L_g}$$

(1)

With:

- $S \equiv$ Shrinkage [%]
- $L_s \equiv$ Length of the sintered part [mm]
- $L_g \equiv$ Length of the green part [mm]

The technical datasheet of the ULTRAFUSE 316L filament estimates a shrinkage of 16 % on the x-y plane while the z-axis shrinkage is 20 % [58]. It should be stressed that the mentioned reference system is the reference system of the component during the debinding process but not necessarily the reference system adopted during the printing process is the same.

The debinding will be performed in a manner that matches both the reference systems, with exception of the Z-oriented specimens (see **Design of experiment** ,page 72). The Z-oriented specimens will be placed in the oven in the same position of X-oriented and Y-oriented samples because the size of the debinding room does not allow otherwise.

The management of the rescale of the component is difficult with the shrinkage value. Slicer software like Simplify3D works with the Oversizing factor, defined according to the Eq. (2).

$$OSF = \frac{L_g}{L_s} \quad (2)$$

With:

- $OSF \equiv$ Oversizing factor [%]
- $L_s \equiv$ Length of the sintered part [mm]
- $L_g \equiv$ Length of the green part [mm]

In the case of the ULTRAFUSE 316L, the print will be rescaled with an OSF_{xy} equal to 1,20 and an OSF_z equal to 1,26.

5.2.4. Identification system

Usually, the identification of the specimen is done with a ink mark. In this case, this approach is not possible because, during the D&S, the high temperature and aggressive atmospheres would erase it. For this reason, all samples will be provided with an identification system that can distinguish them after the D&S process.

The designed identification system consists in adding several pins at the corner of the gripping area that represent the identification number in form of a binary digits. This manner allows to print always the same geometry making it possible to print more than one component in a single job. After the printing, the assignation of the number is performed by breaking certain pins.

We can assume that a broken pin means the 0 value while for the unbroken pin, we can assume it as the 1 value.

The design of this kind of system should also involve a reference system in order to avoid misconception of the assigned number. As assumption, we will place a pin on the corner to hint a unique way to read the digit by left to right.

The Design of Experiment, discussed in detail in **Design of experiment** (page 72), stipulates that thirty samples have to be identified, thus we need to use five pins to represent such number, plus one reference pin that will help to spot the line of reading. At the beginning, the shape of pins was the one shown in *Figure 76*.

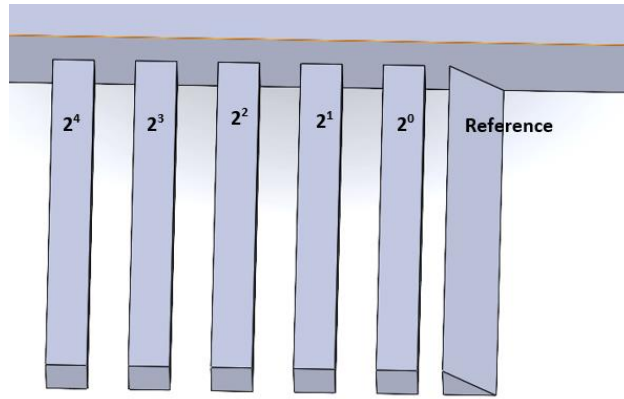


Figure 76. First identification pin system.

These pins were quite slender and often made the print challenging. After some prints, the design was enhanced. The meaning of the pins of the new pin system is provided in Figure 77.

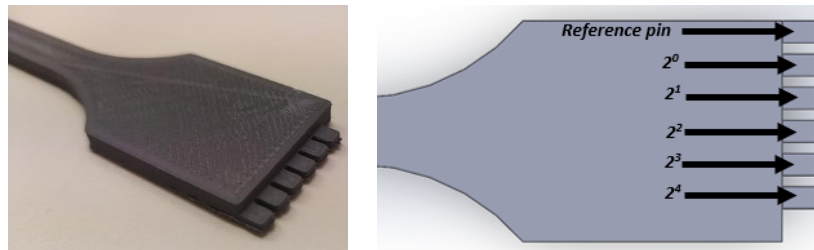


Figure 77. Identification system in tensile test samples: (a) a view of the identification system, (b) meaning of each pin.

Just to better understand the working principle of the system, if we want a sample to be assigned the number 1, equivalent to the number 00001 then we'll break the pins in the way depicted in Figure 78.

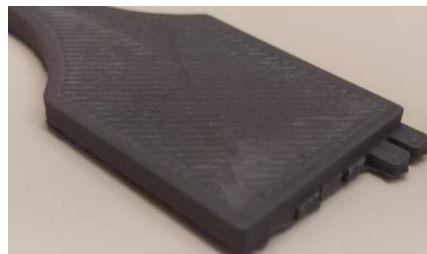


Figure 78. Example of identity assignment.

In the *Table 20*, the whole identification system is presented and summarized.

<i>ID number</i>	<i>Binary digit</i>	<i>Direction of the component</i>	<i>ID number</i>	<i>Binary digit</i>	<i>Direction of the component</i>	<i>ID number</i>	<i>Binary digit</i>	<i>Direction of the component</i>
1	1	X1	11	1011	Y1	21	10101	Z1
2	10	X2	12	1100	Y2	22	10110	Z2
3	11	X3	13	1101	Y3	23	10111	Z3
4	100	X4	14	1110	Y4	24	11000	Z4
5	101	X5	15	1111	Y5	25	11001	Z5
6	110	X6	16	10000	Y6	26	11010	Z6
7	111	X7	17	10001	Y7	27	11011	Z7
8	1000	X8	18	10010	Y8	28	11100	Z8
9	1001	X9	19	10011	Y9	29	11101	Z9

10	1010	X10	20	10100	Y10	30	11110	Z10
-----------	------	-----	-----------	-------	-----	-----------	-------	-----

Table 20. Identification of all ULTRAFUSE 316L samples.

5.2.5. Design of experiment

The assessment of the ULTRAFUSE 316L will involve three orientations, reported, and named in the *Figure 79*.

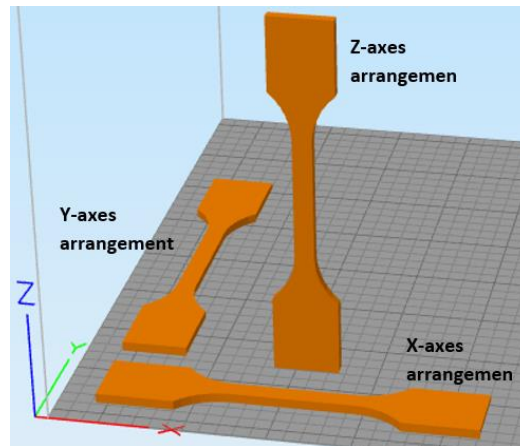


Figure 79. Orientation examined during the tensile test.

The goal of the X-axis and Y-axis orientations is to examine if in the movement system of the extruder there is some factor that causes some difference. The comparison with the Z-axis orientation is useful to quantify the drop of mechanical properties, information extremely important to modelling component printed via metal FDM with some FEA software.

All mentioned orientations will be replicated ten times in order to reach a consensus between a reasonable statistical validity and the limited amount of material and time.

5.2.6. Manufacture

In this subsection will be presented all the trials ran during the optimization process, the adjunctive precautions used in the printing of the batch and finally the post-process employed.

5.2.6.1. Optimization process

The optimization process is organized in two separated parts. In the first part of this optimization process, the tensile specimens will be printed with the original geometry and no re-shaping, aiming to detect possible technical problems without large waste of material. The second part will take care of the printing of the specimen geometry with enhanced gripping area and re-shaping to balance the shrinkage expected in the D&S process.

Trial 1-5

The first part of the optimization, whose all tests are presented in *Figure 80*, was very quick.



Figure 80. Optimization trials of the non-rescaled geometry.

The main problem to face during the optimization was the adhesion of the first layer. The lifting of the first layer due to the thermal shrinkage leads to buckle of the layers. During the deposition process, the buckling reduced the actual gap between the nozzle and the following layer inducing the specular effect of the overflow. The final result of this problem is the worsening of the lateral surface quality, shown in *Figure 81*.



Figure 81. Lateral surface of the fourth trial with visible stripes due to the deadhesion of the first layer.

The second problem experienced in the optimization process was the damaging of the filament caused by the feeding motor's gear, underlined in the *Figure 82*.



Figure 82. Damage on the filament caused by the feeding system gear.

This issue was due to the mismatch between the extrusion speed too high and low temperature extrusion, resulting in incompatible values of viscosity. On the other hand, the increasing of the temperature may not be the most proper solution to reduce the viscosity since this could exacerbate the thermal shrinkage on the print with consequent detachment of the first layer.

However, it's important to remark that this optimization was achieved with the help of some glue stick to enhance the adhesion of the first layer. Anyway, the whole process was done without the help of the support material.

The modified parameters resulting from the optimization process are listed in *Table 21*.

Parameter	Trial 1	Trial 5
Skirt Layers	1	4
Primary Layer Height	0,1 mm	Bottom Process 0,2 mm Following Process 0,1 mm
First Layer Speed	100%	60%
Skirt outlines	8	14

Table 21. Parameters involved in the optimization process of the non-rescaled geometry.

The parameter set found in the xy-orientation was adopted in the printing of the z-oriented specimen. The result, as shown in *Figure 83*, was surprising because contrary to the ASA, the ULTRAFUSE 316L was able to perform a slender structures and overhanging structures without supports. In the end, the quality of the surface achieved is quite smooth, compared to typical surfaces achieved with the Metal FDM technology.



Figure 83. Result of the print of the Z-oriented specimen.

Trial 6.1

Since the parameter optimization was achieved for the original geometry, the first printing trial with the modified geometry, provided with the pin system, is performed in a batch of five components to check the print quality in different locations of the bed. It is to be noted that also in this case. In the *Figure 84*, is shown the result of the trial failed. The reason of the failure of the print was due to the bad calibration of the heated bed resulting in the consequent change in adhesion properties depending on position on the plate.

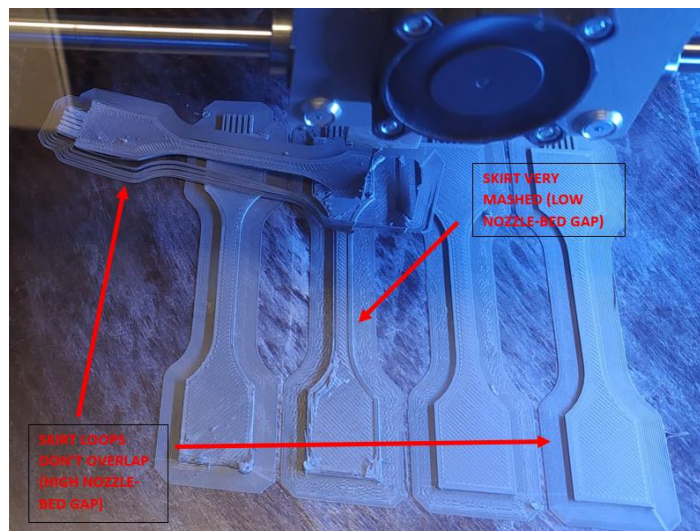


Figure 84. Failed print due to the bad planarity calibration.

This test shows that the performed calibration of the planarity of the bed was not accurate. This effect results in a very changeable overlapping between rasters as exhibited by the quality of the texture of the brim structures depicted in *Figure 85*.

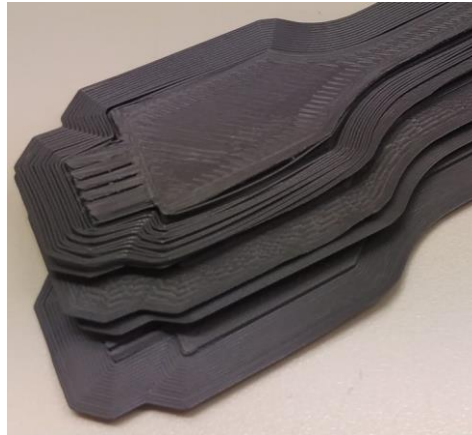


Figure 85. Changeable texture of the brim structures due to the bad planarity calibration of the bed.

The conclusion of this test is that the printer urges a recalibration of the planarity of the bed to ensure a constant nozzle-bed gap.

Trial 6.2

After a new calibration of the bed, the test is re-run with the same parameters. The result shown in the *Figure 86 (a)* remarks how the batch was successful printed.

At the same time, again in the *Figure 86 (a)*, it's easy to see that the accuracy and the quality achieved is barely sufficient. In the end, the *Figure 86 (b)* showing the test pieces stacked, remark how they are buckled. The buckling effect is probably due to the thermal shrinkage that leads to the detachment and the buckling of one of the two grips of the specimens.



Figure 86. Print result after the planarity calibration: (a) lateral surface view; (b) warping effect due to the thermal shrinkage.

The success of this print allows to add a new difficult level, the rescaling of the component through the proper function in the slicer software.

Trial 6.3

The rescaling of the specimen has an enormous influence on the end result. In fact, as shown in the *Figure 87 (a)*, the lateral surface is worse than the one seen in *Figure 86 (a)*. In the *Figure 87 (b)* it's remarked the

warping is due to the thermal shrinkage. Last but not least, it's possible to notice that the quality of the lateral surface in the grips, where the thermal shrinkage is more accentuated because of the presence of more material, is less accurate.

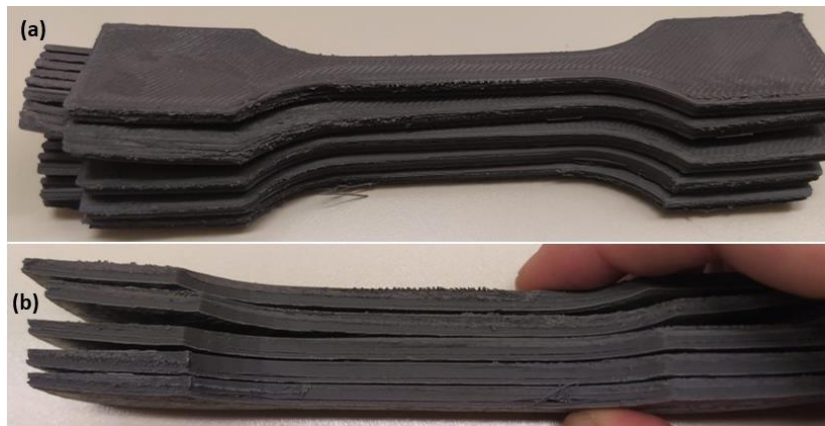


Figure 87. Print result after the rescaling of the geometry: (a) lateral surface view; (b) warping effect due to the thermal shrinkage.

This test highlights that the temperature provided by the heated bed is not effective enough to ensure an acceptable adhesion of the print. In conclusion, the solution proposed in the next test is the removal of the glue to assess if this may enhance the adhesion force.

Trial 6.4

The result of the print is shown in the *Figure 88*. The *Figure 88 (a)* shows how the achieved lateral surface is still not perfect but is however better than the result of the previous prints.

The lateral surface, shown in the *Figure 88*, presents again the warpage typically due to the thermal shrinkage.



Figure 88. Print result after the removal of the glue from the bed: (a) lateral surface view; (b) warping effect due to the thermal shrinkage.

It as to be said that in this case the magnitude of the warping is very lower, compared to the previous prints.

The conclusion following to this observation is that the removal of the glue affected positively the quality of the print. Plus, this test confirmed that the part material can't provide sufficient adhesion to prevent the first layer detachment. Thus, in the next attempt, we'll evaluate the effect the raft structure made in HIPS has on the quality of the adhesion of the print.

Trial 7.1

This is the first print in which we adopt the double extrusion process to print a large component. In the *Figure 89* it is depicted the raft structure designed to enhance the adhesion of the first layer.

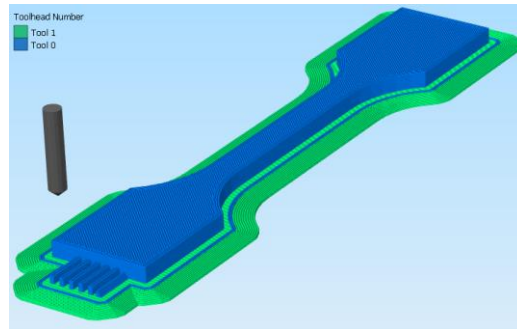


Figure 89. Preview of the print with demarcation of material deposited.

The print was stopped during the deposition of the first layer of part material because, as shown in *Figure 90*, the support material nozzle was keeping colliding with the raft structure risking to remove it.

Moreover, it's possible to see that the raster air gap was too accentuated, hence in the next print we will try to solve this problem by changing the parameter "Separation Offset from Part" from 0,14 mm to 0,00 mm. This will force the nozzle to mash the material against the raft. The presence of an excessive raster air gap is to be avoid because it can lead to a weak adhesion with the raft structure and consequent detachment or displacement due to the thermal shrinkage.

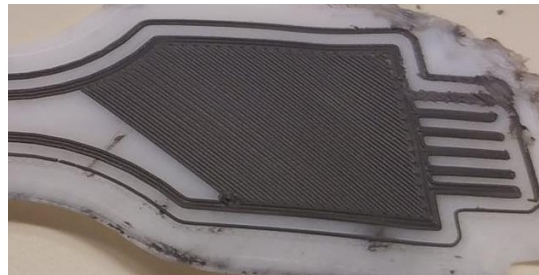


Figure 90. First layer with remarked raster air gaps.

The alinement procedure of the two nozzle is described in the paragraph "Equalization of nozzles position"(Page 108).

Trial 7.2

After the re-alinement, a new attempt is done with the new parameter configuration. In this case, we will come back to assess again the result obtained with the batch printing.

The result of the print is revealed in *Figure 91*. The batch is homogeneous, and the top view shows regular surfaces free of evident defect or pores.



Figure 91. Resulting print of the batch of tensile test specimens with the raft structure.

In the *Figure 92 (a)* it's shown that all top surfaces are regular but next to the fillet zones, some blobs due to the oozing effect are visible. Compared to the previous attempts, in the *Figure 92 (b)* it is remarked that in this case the warping is almost completely contained on wide-scale even though the thermal shrinkage keeps manifesting in the form of stripes visible in the lateral surface of the grips.



Figure 92. View of the result of the print: (a) top and lateral surfaces; (b) piled specimens.

The retained presence of thermal warpage is also confirmed by the deformation of the raft, shown in *Figure 93*. The shape of the warping highlights that the shrinkage is more severe on the grips and particularly on the edge of the specimen while the narrow part is not interested from this effect because the entity of the shrinkage is smaller. This problem means that new ideas must be explored to tightly hold the specimen during the deposition process.



Figure 93. Warping effect of the raft structure due to the thermal shrinkage of the part material.

Another problem to be noted is the presence of the marks on the bottom surface of the grips, denoted in the Figure 94. Those scars result from the scratching of the hot part-material nozzle on the layer of the raft structure under construction.

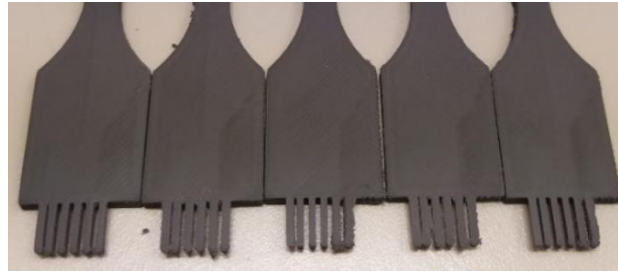


Figure 94. View of the bottom surface of the specimens with scars on the grips due to the part material nozzle.

In conclusion, in the next attempt the raft will be developed in a different way to enhance the holding force that the support can exert on the component during the deposition.

Trial 8

The solution proposed to solve the problem is the addition of a lateral wall that enhances the holding force thanks to its clamping effect.

The described wall is performed by means of the oozing shield. The new method to stabilize the pressure in the part material nozzle is the printing of a “Prime Pillar”, a tower nearby the print. The Prime Pillar is usually adopted in tall prints to keep pressurized the nozzle melt material when the two extruder works alternatively. In this case, since we just need to pressurize the nozzle in the starting stage, the pillar will be performed only in the first layers with a square large enough.

All the observations mentioned are summarized in the Preview Mode of the print, shown in the Figure 95.

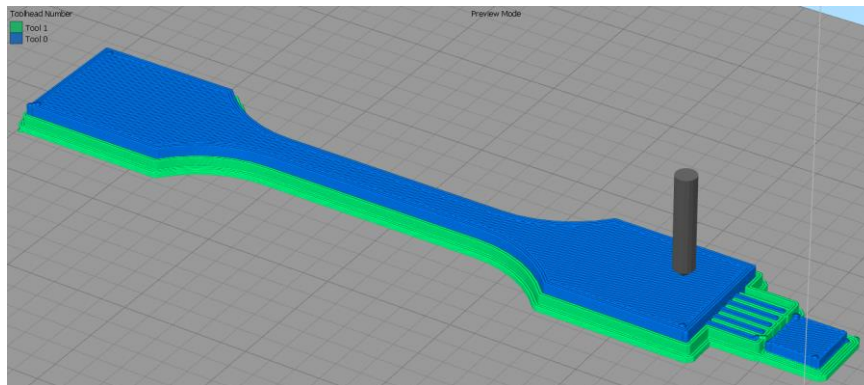


Figure 95. Preview of the print with the implementation of the lateral holder structures.

The result of the print, shown in the Figure 96, unveils that the presence of the lateral support changes the size of the lateral surface since it compresses the part-material. Nevertheless, the interaction between the two materials makes it hard to remove the support structure and this impact on the economical balance of the print because make it necessary the use of the solvent.



Figure 96. Result of the print with lateral support structures.

Given the failure of such type of support, in the new attempt the raft adopted in the Trial 6 will be re-employed. This time, to make sure that the raft won't warp, the number of layers of the raft will be enhanced. As a new strategy to save support material, the Prime Pillar will be used again instead of using the oozing shield to print a loop surrounding the component.

Trial 9

In the new attempt, the pin system is changed because the current pins are too slender and this increase the quantity of support-material required by the raft and, as direct consequence of this, the magnitude of the thermal shrinkage rises.

Compared to the Trial 7, in this case the number of layers of the raster structure will be raised from four to five and the number of brim loops will be decreased from ten to four. This choice aims to make the raft structure more compact and less prone to large thermal shrinkages.

The new pin system is discussed in detail in the paragraph "Identification system" (Page 70). The look of the new design is shown in the *Figure 97*.

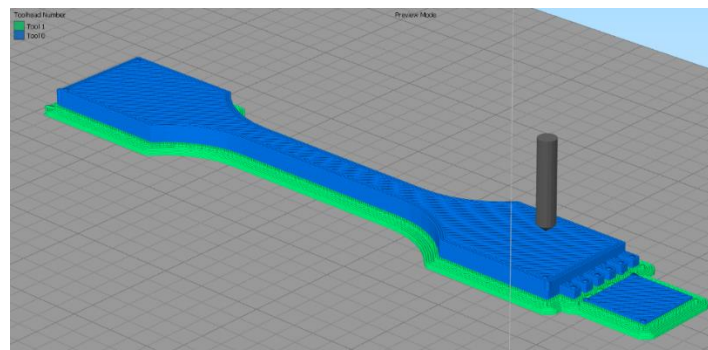


Figure 97. Preview of the printing of the "Trial 9" specimen.

The quality of the result of the print, displayed in the *Figure 98*, is quite good. Again, in this case, the warping of the raft structure suggests that the thermal shrinkage was out of control.



Figure 98. Result of the printing of the "Trial 9" specimen.

Another observation that can explain the reason of the bad quality associated to the clamps of the specimen is the point in the layer from where the deposition starts. This point can be chosen in a way that optimize the time of the printing, as starting always from the same point on any layer or as random point.

So far, this parameter was set on the optimization of the time of the print. In the *Figure 99* are shown all the points where the deposition process starts. Usually, the beginning of the deposition is associated with the “retraction”. During this operation the filament is pulled up of a certain length when the extruder is at rests to prevent the oozing of the material, and later it pushes down the filament of the same length when the deposition starts back.

Again, in the *Figure 99 (b)* is visible that the surface “A” is quite smooth while the surface “B” is irregular since is the starting line in the deposition of every layer. This means that at the beginning of the deposition of the layer, the quantity extruded is greater than the ideal amount required and then gradually stabilizes.

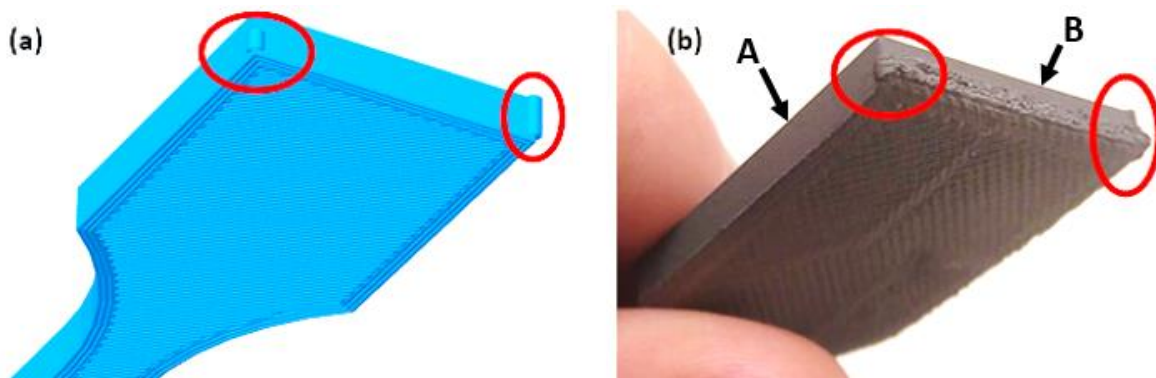


Figure 99. Retraction effect on the print: (a) retraction points in the preview mode; (b) retraction effect on the print.

The assessment of the retraction is now under exam because if we find a correlation between it and the bad quality of the lateral surface, this could downsize the supposed influence of the thermal shrinkage on the end result.

In conclusion, the next attempt will assess the effect of the retraction on the lateral surface quality.

Trial 10

In this attempt, the interface between the specimen and the raft is improved to enhance the adhesion and so avoid the thermal shrinkage. The improvement consists in the adjoint of an eight-loop brim structure. Moreover, to see the effect of the retraction point, the deposition of all the layers will always start from the same starting point, positioned in the same corner and circled in red in the *Figure 100*.

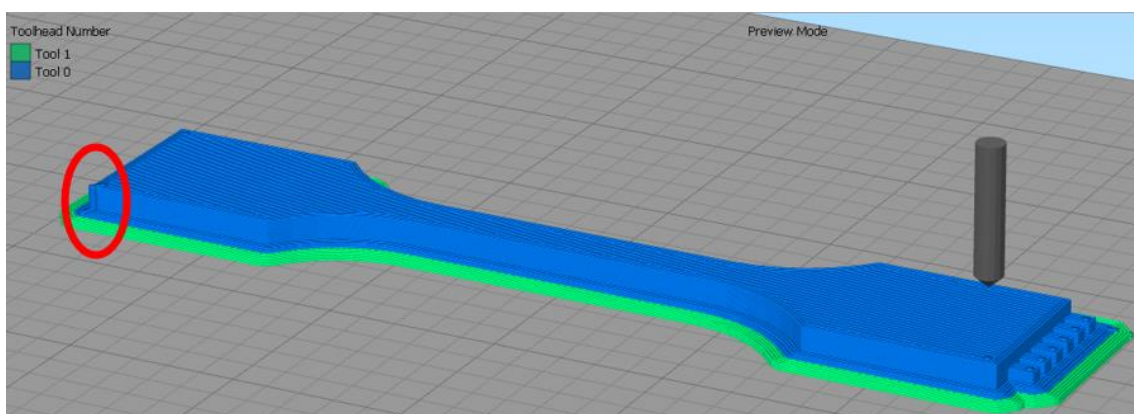


Figure 100. Preview of the "Trial 10" specimen whose the starting points of each layer are circled in red.

The specimen has been successful printed, and the result is depicted in *Figure 101*.



Figure 101. Result of the printing of the "Trial 10" specimen.

In the *Figure 102*, the effect of the retraction is remarked. The lateral surface shown in *Figure 102 (a)* exhibits an irregular surface. This happens because at the beginning of the deposition of the layer, the path followed is always the same and probably the material dropped is excessive.

This explanation is confirmed by the *Figure 102 (b)* in which it's visible that the last section deposited shows a good quality. In other words, the hypothesis that attributes to the thermal shrinkage the bad quality is to be reject because in that case, also the last section deposited shown in *Figure 102 (b)* should have exhibited the same irregular surface.

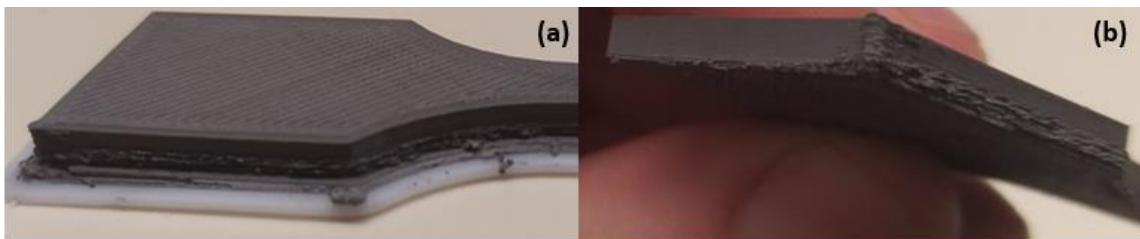


Figure 102. Bad quality caused by the retraction: (a) lateral edge of the grip; (b) corner of the grip.

The main problem related to the bad quality caused by the retraction is that some stripes reach the narrow part of the specimen and this could potentially compromise the stress distribution during the tensile test or disturb the acquisition of the cross section.

At a proper distance from the starting point, as revealed in the *Figure 103*, the quality of the surface is excellent because the pressure in the nozzle is stabilized resulting in regular surfaces. This confirms that the set printing parameters, except for the retraction distance, are correct.



Figure 103. Lateral view of the "Trial 10" specimen.

The solution to be verified in the next trial is the reduction of the retraction distance from 5 mm to 3 mm to see how strongly the retraction can affect the quality of the print.

Trial 11

The result of the print is surprising because, as remarked in the *Figure 104*, the marks due to the retraction are less visible.



Figure 104. Grip of the "Trial 11" specimen with focus on the lateral surface.

This confirms a strong effect of the retraction distance on the quality of the print, but the further reduction of the retraction distance is discouraged because with low values the oozing becomes a serious problem to face.

Given that the quality of the surface obtained is good and the stripe-scars only interest the grips area, it is not needed to go deeper in the optimization of the retraction distance. The last enhancement left to do for the surface is possible by moving the starting point so that the first section and the stripe-scars are further from the narrow part of the specimen.

Trial 12

In this trial, the starting points are moved to the position indicated in the *Figure 105*, remembering that all the perimeter loops keep being deposited in the counter clockwise direction.

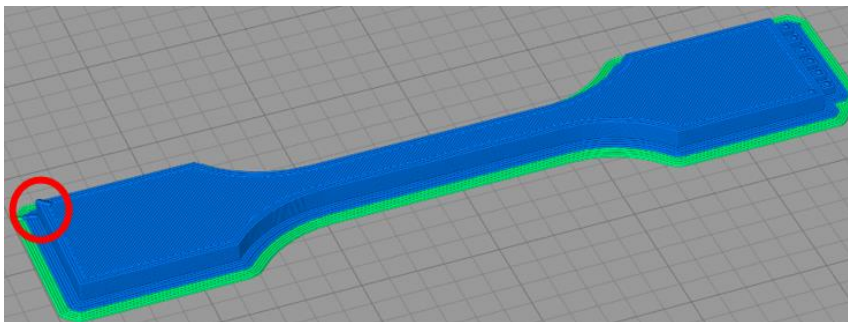


Figure 105. Preview of the "Trial 12" specimen whose the starting points of each layer are circled in red.

The result of the print is displayed in the *Figure 106* and, as the previous prints, printing quality is all in all good.



Figure 106. Top view of the "Trial 12" specimen.

The worsening of the lateral surfaces in the *Figure 107* may be caused by the change of the starting point or might have been favoured by the visible damaging of the raft caused by the part-material nozzle during the deposition of the HIPS.

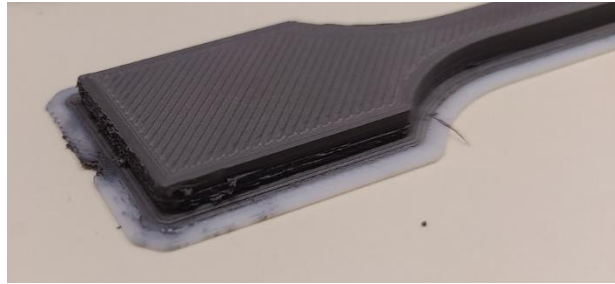


Figure 107. Detail view of the clamp of the specimen "Trial 12".

The proposed solution to solve this condition consists of the reinforcement and protection of the raft structure, especially during the deposition of the HIPS.

Trial 13

The adopted strategy that will prevent the damaging of the raft structure requires that the part-material nozzle is at rest during the deposition of the raft structure. Then, the part-material nozzle should be gradually warmed up just before the deposition of the part-material is about to begin.

The reinforcement of the raft, depicted in the *Figure 108*, is performed by means of the increasing the number of layers of the raft structure from three to five layers.

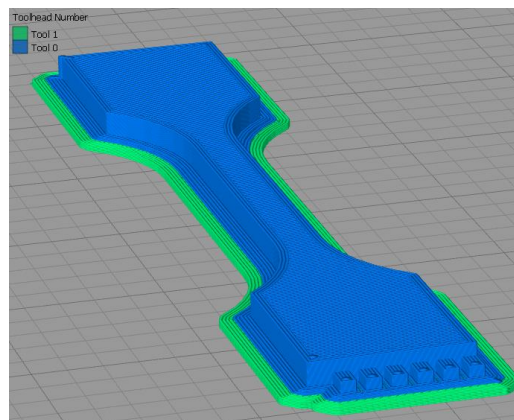


Figure 108. Preview of the "Trial 13" specimen.

In the *Figure 109*, are reported two component successful printed with this parameter set.



Figure 109. Top view of the "Trial 12" specimen.

The disappearance of defects on the lateral surfaces confirms that the proposed solution was effective, as remarked in the *Figure 110*.

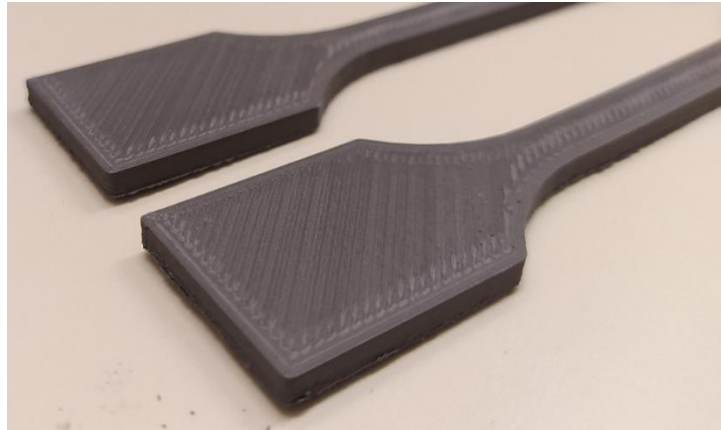


Figure 110. Detail view of the clamp of the specimen "Trial 13".

This trial ends the optimization process regarding the tensile test specimens. Those printing parameters are the same that will be used for the printing of the z-oriented specimens because, as seen in the previous attempts, the print of specimens with such orientation were easy to manage.

5.2.6.2. Batch printing

Even when the print of a specimen success, the print of the component in large quantity might not result a trivial task. This problem is due to the strategy to be adopted in the print of all components because the interaction of two prints can result in the alteration of the predicted print strategy and this may affect the result leading to further research of additional parameter to change.

The factors whose influence was evidenced in the printing of the batch are collected here:

1. The distance between objects

The distance between two components in the same job can be a decisive factor. In Simplify 3D it's possible to get an automatic arrangement of the components, but this command doesn't consider the number of brim loops. If two components are too close, like the example depicted in *Figure 111(a)*, the brim structures are in contact. As displayed in *Figure 111(b)*, in the definition of the new deposition path, the slicer software merges the two-brim structure, and the new formed inner perimeter is ignored.

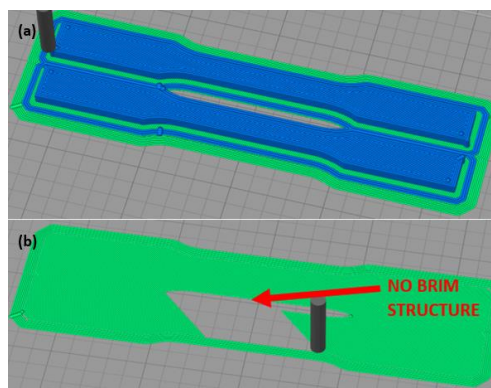


Figure 111. Spacing of components: (a) preview of the print of two components too close; (b) ineffective brim structure.

As result of this, the inner perimeter is not provided with brims that anchor it on the bed and when it starts to shrinks thermally, it is free to warp leading to the failure of the whole print.

Moreover, in the *Figure 112*, the print failed because all components shared the same bed layer. In this case, the failure of the shared layer caused the fail of the whole job. This situation is unnecessarily risky probability because the probability that this could happens is higher since larger layers lead to greater thermal shrinkages.

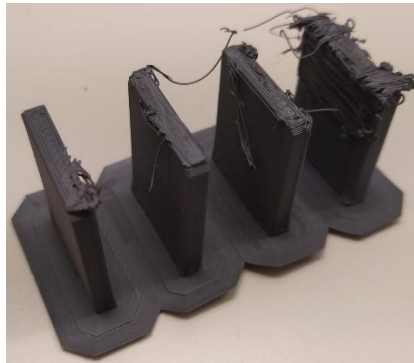


Figure 112. *Print failure due to the setting a shared bed layer.*

Thus, it's recommended to ensure a minimum distance between all components in the job to avoid that the detachment of a single component will lead to the total failure of the job.

2. Sequence of the print

The sequence with whom the layer of different objects will be printed depends on when the associated *Process* was created. In particular, as shown in *Figure 113*, if we assign the same *Process* to all objects the slicer software will command to the extruder to print at first the brim structure of all objects of the job and then to turn back and print the infill.

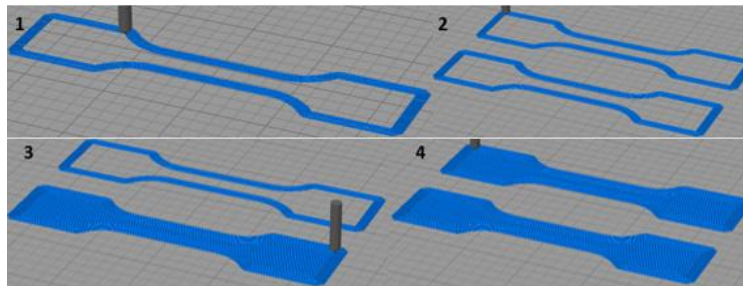


Figure 113. *Mono-process printing strategy sequence.*

This kind of strategy can bring to the detachment of the just-deposited brim structure with possible failure of the print.

Another strategy, depicted in *Figure 114*, consists in assigning independent *Processes* to each object. In this way the layer of all components is printed all in one time and it's possible to sort them so that a priority ranking is given in order to avoid accidental collisions.

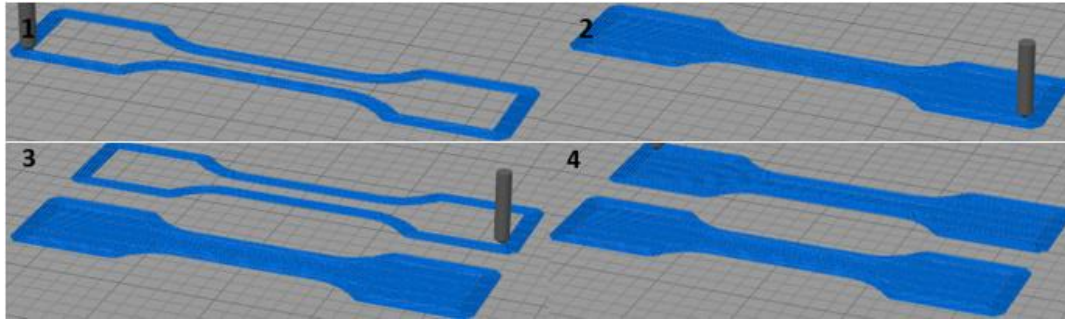


Figure 114. *Independent processes strategy sequence.*

The recommended strategy is the second one because it makes easy to manage the whole *Processes* but on the other hand, if we mean to print a large number of objects in a single job it may be difficult to handle this procedure.

5.2.6.3. *Post- process*

The following procedure is the same for all specimens but in this paragraph, we'll just take as reference the procedure used for the X-Y oriented specimens since it was the more delicate and time-consuming.

The first step of the polishing process is the peeling of the support material bed layer. The layer is easy to come out and this is why the layer is removed manually, as depicted in *Figure 115*.



Figure 115. *Bed layer peeling: (a) during the procedure; (b) after the procedure.*

Following this, the retained brim structure is removed manually just by mending it with the fingers leaving a defined edge, as done in the *Figure 116*.



Figure 116. *Brim removal process.*

The final step is the identification of the specimen by means of a unique pin combination. This operation was ran with a pincer as explained in the *Figure 117*.

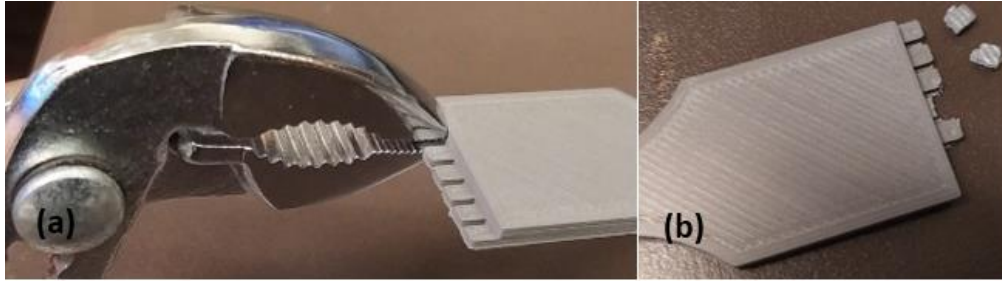


Figure 117. Identification assignment process: (a) during the removal of pins; (b) after the process.

5.3. Shrinkage sample

The D&S process is a very delicate stage in the Metal FDM process. The high temperatures and time of exposure make it an expensive and critical stage that may conclude with the destruction of the component. Thus, it's important to give a close look to this process before the actual print of titanium tensile specimens.

The supplier company of the titanium feedstock states that the shrinkage associated to the D&S process is highly dependent to the exposure time and it may vary from 7 %– 10 %, with a final density of 80 % – 85 %, up to a shrinkage of 20 % with 90 % of density in case of intensive D&S process [70].

This means that it's difficult to estimate the actual shrinkage because it depends on the available sintering process. An important constraint to consider in the decision of the sample to be adopted is the quantity of available feedstock since it was possible to buy just one 0,5 Kg spool.

5.3.1. Shape of the sample

Initial shrinkage model considered consisted in cubes with 10-, 20- and 30-mm side. In this design of experiment (DoE), the quantity of material required increases truthfully with the increase of the side of the cubes.

A convenient design should perform different sides in the three directions, but maintaining the same volume.

Each specimen type is designed to be printed in batches of 10 pieces whose dimensions are reported in *Table 22*.

<i>Specimen name</i>	<i>X – dimension [mm]</i>	<i>Y – dimension [mm]</i>	<i>Z – dimension [mm]</i>	<i>Sketch</i>
A	5	15	10	
B	10	5	15	
C	15	10	5	

Table 22. Geometrical features of shrinkage specimens.

Even though, compared with the adopted DoE, the one that involves cubic shape can provide more information about the size effect and the effect of the D&S in a bulk object, as highlighted in *Table 23*, it is not sustainable with the current amount of material owned. By using the geometries described in the *Table 22* we can save half of the material required in the cubes DoE.

<i>DoE</i>	<i>Cubes Volume [mm³/ piece]</i>	<i>Batch volume (10 pieces) [mm³]</i>	<i>Parallelepipeds [mm³/piece]</i>	<i>Batch volume (10 pieces) [mm³]</i>
<i>Sample type A or 5 mm side cube</i>	125	1250	750	7500
<i>Sample type B or 10 mm side cube</i>	1000	10000	750	7500
<i>Sample type C or 15 mm side cube</i>	3375	33750	750	7500
<i>Total volume required [mm³]</i>	45000		22500	

Table 23. Comparison of material required with different DoE.

5.3.2. Orientation and identification system

The identification of the orientation or the univocal identification of the sample is usually a task made with the ink marks.

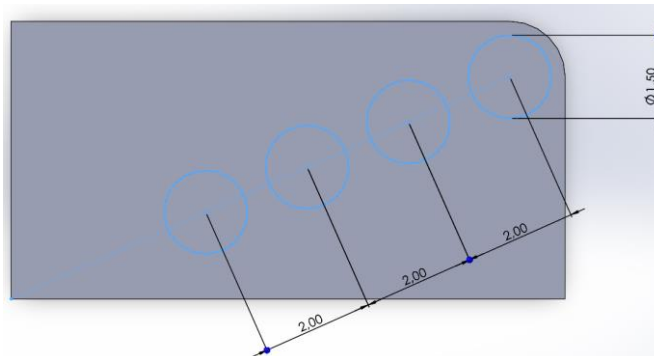
In this case, the ink is no longer usable because it's not capable of resisting the temperatures of the D&S process. This means that an alternative method should be designed to identify univocally all the specimen.

The univocal orientation on the x-y plane can be achieved by rounding the top-right edge of the specimen with a 1 mm – radius fillet. The strategy mentioned to orient the component doesn't provide information on the identification of the bottom and the top surface, thus we will place some pins on the top surface during the deposition process.

The pins will also work as an identification system working as bits of binary digit. Particularly, they will be meant as zero-value when broken and one-value if they are intact.

We will alternatively change the height of the pins to make it simpler to identify the true meaning of the pin without using a reference pin. The purpose of the reference pin is to dictate the line of reading, because the identification of the position of the pin could be a difficult task, leading to a misunderstanding of the real identification number.

In this case we don't need to identify univocally the sample in the total number of all specimens printed but just identify it among the other samples of the same type, hence we will need a binary system that goes up to 10 and not to 30 (total number of all specimens). Thus, we will adopt a 4-pins system aligned along the diagonal of the chosen surface and whose geometrical features are reported in *Figure 118*.



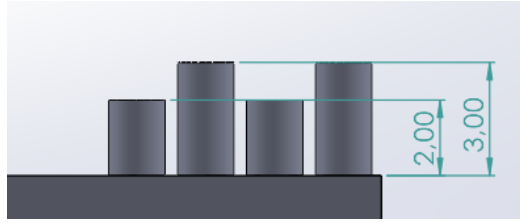


Figure 118. Geometrical features of the identification system of the Specimen Type B.

In this design, the reference pin will coincide with the 2^0 pin and will be the only one placed on the rounded edge. The definition of all pins is unfolded in detail in the Figure 119.

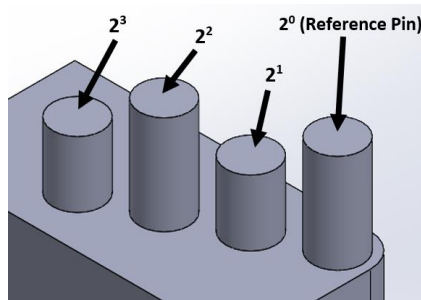


Figure 119. Value associated to every pins.

As arbitrary choice, we'll take care that the deposition orientation, shown in Figure 120, will be the same adopted during the D&S process. In this way we'll see how the sizes changes on the three axes considering the dimensional errors due to the deposition process and the changes of the geometry due to the D&S. The data collected after the D&S process will be useful to build a compensation model able to achieve more accurate end products.

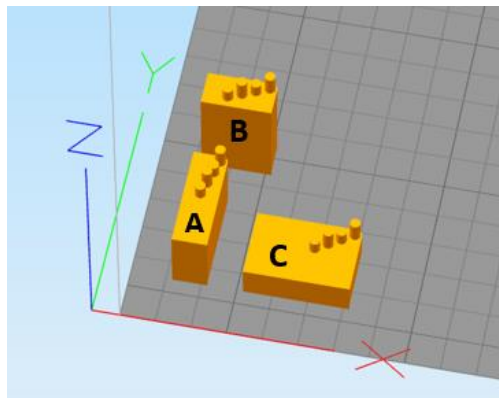


Figure 120. Layout of specimens on the printing bed.

5.3.3. Manufacture

In this subsection will be presenting all the trials ran during the optimization process, the adjunctive precautions used in the printing of the batch and finally the post-process employed.

5.3.3.1. Optimization process

In this case, the raft structure made in HIPS is useful. The main benefits offered by the raft are the compensation of slight misalignment of the bed and the insurance of a good adhesion. Once consolidated

the correct parameters for the raft, whose list is reminded in Table 24, the adhesion of the first layer is no longer a problem no matter the size of the print.

Parameter	How it is involved
Raft Extruder	Extruder appointed to print the raft structure: Extruder 1 (part material) or Extruder 2 (support material)
Raft Top Layers	Layer with a customizable infill rate
Raft Base Layers	Layers with low infill rate to make the component-removal easy.
Raft Offset from Part [mm]	Additional height, referred to the nominal layer height, given to the first layer laid on the raft on the raft.
Separation Distance [mm]	Increase the width of the raft to avoid the edge defects and warpages to affect the quality of the first layer laying on the raft.
Raft Top Infill [%]	Decide the infill rate of the top layers, in our case it affect the quality surface of the bottom layer.
Above Raft Speed [%]	Deposition speed of the first layer deposited on the raft, related as percentage of the nominal printing speed.

Table 24. Raft settings.

The first layer of part material laid on the raft will result defected if no strategy is planned to stabilize the pressure of the material in the extruder. In the *Figure 121*, is remarked that finding the right strategy to provide an adequate pressure at the beginning of the print is an hard task because the software is not able to handle brims/skirts combined with rafts in the way we expect.

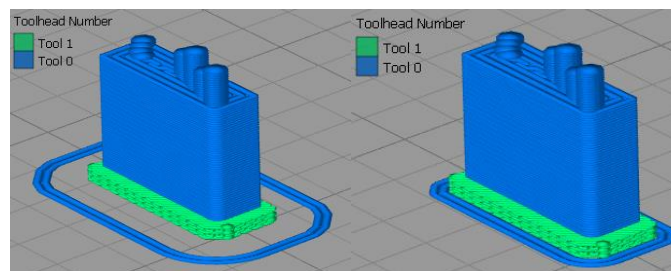


Figure 121. Ineffective use of the skirt (a) and brim (b).

Indeed, they're performed in the very bottom layer while we wish it to be printed just before the print of the first layer of part material.

The solution to this problem involves the "oozing shield", another additional structure consisting in a wall surrounding the structure. When the extruder is at rest, the material may drips (or ooze) because of the residual pressure in the extruder. The oozes often stick to the surface leading to a bad quality but when the oozing shield is employed, the oozing material sticks to the wall and not to the lateral surface of the print.

This solution implies another problem because if we add the oozing shield next to the print, this will change the real sizes of the specimen, as depicted in the *Figure 122*.

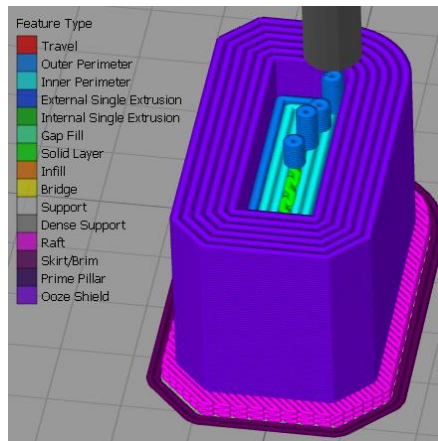


Figure 122. Effect of the oozing shield on the print by setting a single Process.

Hence, the employed *Process* will be split in two, as depicted in *Figure 123*, so that the *Process* named “Bottom” will perform the oozing shield as a structure similar to a brim. Moreover, the presence of two *Processes* can help to provide an adequate flow rate to pressurize the part material more efficiently, and the other *Process* is dedicated to sequent layers.

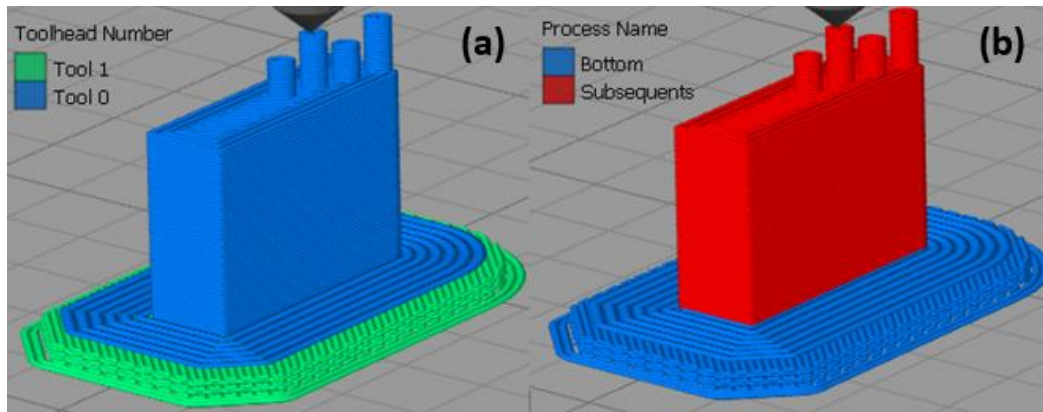


Figure 123. Preview Mode: (a) Materials of competence; (b) Processes of competence.

The result obtained in the *Figure 123* shows the configuration from which we will start for the optimization process.

Trial 1 (Type-A)

The print of the first trial failed, as depicted in *Figure 124*, because some problem related to the under extrusion occurred. The quality of the first layer was barely sufficient and this affected the success of the second layer.



Figure 124. First trial of optimization of the A-type specimen.

The part material nozzle was designed to start to warm up during the deposition of the fifth layer of the raft structure and starting from the sixth layer it was supposed to start the deposition of the feedstock.

As it is suspected that this contributed to the failure, the countermeasure adopted consists in anticipate the warming process during the deposition of the fourth layer rather than the fifth.

Trial 2 (Type-A)

The measures proposed were not enough. The print was stopped because there was not contiguity between the loops of the layer, as shown in *Figure 125*. The consistency of the raster remarks that the material deposited in the previous test was a mixture of the titanium feedstock and the steel feedstock previously used in the extruder. It's possible to see that the titanium powder owns a different colour and a different adhesion with the HIPS-made raft.



Figure 125. Second trial of optimization of the A-type specimen.

During the deposition process, another criticality emerged is that the infill material was printed twice per layer, and this played a key role in the fail of the print. Thus, the following changes in the *Process* were pursued:

- The tick for the parameter “Print every infill angle on each layer” was removed.
- The internal Fill Pattern was changed from Grid to Rectilinear.

Trial 3 (Type-A)

In this case, every layer was successful printed showing that the corrections were proper. Anyway, in the *Figure 126* are easily visible some pores and bad overlaps between the loops. Furthermore, there are visible pores also inside the raster pointing that the combination of temperature and printing speed should be adjusted.



Figure 126. Third trial of optimization of the A-type specimen.

Since the actual extrusion temperature (230°) is near to the degradation temperature of the binder(235°-240°), the next move will be the evaluation of the decrease of the temperature. The regime extrusion temperature will be changed from 230° to 220°.

Trial 4 (Type-A)

The result of the extrusion temperature, reported in *Figure 127*, shows a sensible enhance of the quality of the raft and of the actual infill performed. The problem related to the overlapping between the loops is again present.



Figure 127. Fourth trial of optimization of the A-type specimen.

The attempt to solve the excessive air gap will consists in reducing the distance that the software estimates in the definition of the deposition path. This solution can be acted by changing the Extrusion Width

parameter. When set to Auto, the Extrusion Width is assumed as 0,72 mm, thus the value will be entered manually and set on 0,65 mm.

A practical example to explain the effect of this setting is explained in *Figure 128*. The influence of the Extrusion Width is easy to grasp if we compare the look of the Auto Extrusion Width value with a very low extrusion width value, for instance equal to 0,3 mm.

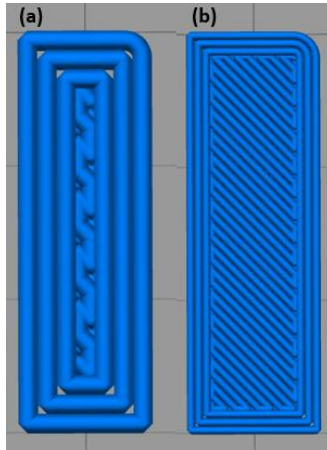


Figure 128. Extrusion width effect: (a) Auto width; (b) 0,3 mm manual setting.

Trial 5 (Type-A)

The result of the print, displayed in *Figure 129*, shows that the change of the Extrusion Width has been beneficial. The most relevant benefit of the Extrusion Width is the reduction of the air gaps, although their presence is still visible.



Figure 129. Fifth trial of optimization of the A-type specimen.

The presence of some retained air gap means that the optimal Extrusion Width is shorter than the set value. Hence, in the next attempt the Extrusion Width will be entered as 0,6 mm. At the same time, the Extrusion temperature is raised to 225° in order to attempt to achieve a raster free from internal pores.

Trial 6 (Type-A)

The top view of the result, shown in *Figure 130(a)*, highlights that the overlapping between the perimetral loops and the infill is slightly enhanced but at the same time the infill exhibits remarkable voids. The lateral view of the specimens depicted in *Figure 130(b)* underlines that the quality of the raster needs further enhancement because there are discontinuities in the deposition process.

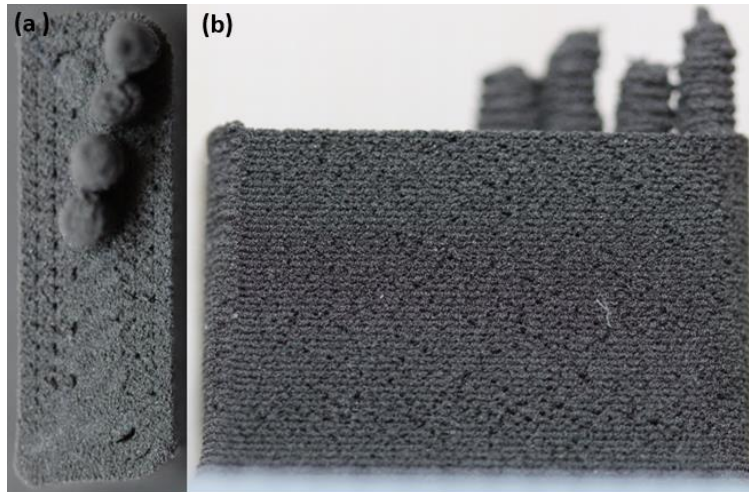


Figure 130. Sixth trial of optimization of the A-type specimen: (a) Top View; (b) Lateral View.

The deposited material looks stretched, thus in the next attempt the deposition speed will be reduced from 15 mm/s to 12 mm/s.

Trial 7 (Type-A)

The result of the print, presented in *Figure 131*, confirms that the printing speed affects the quality of the deposition process. The top view depicted in *Figure 131(a)* exhibits some well visible pores. By comparing the lateral surface with the one seen in the previous test, the current result shows fewer voids and pores as depicted in *Figure 131(b)*.

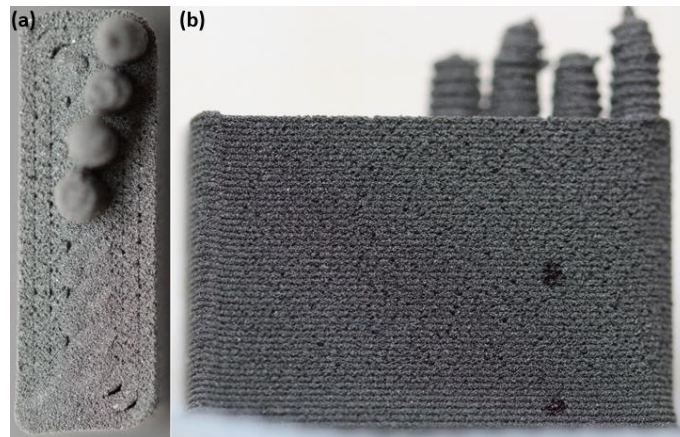


Figure 131. Seventh trial of optimization of the A-type specimen: (a) Top View; (b) Lateral View.

Again, in *Figure 131(b)* two ink-marked points made on the surface point out that that, in the lower layers, no voids are exhibited while in the following layers the presence of pores becomes more accentuated.

For now, the most critical problem to face is the presence of evident pores by looking the print in the top view. With respect to the pores located in the raster, the voids present on the top surface are more critical because probably that kind of pores form channels in the deep of the print and can start the formation of a crack.

The strategy pursued to fix this problem is to decrease once more the Extrusion width in order to force loops to overlap with each other. This time the extrusion width will be reduced to 0,55 mm.

Trial 8 (Type-A)

The result of the test, depicted in Figure 132, is still not satisfying because some voids are still clearly visible in the top view. Anyway, in this case the overlapping between all perimetral loops seems to be very regular.



Figure 132. Eighth trial of optimization of the A-type specimen.

Since this result is still not enough, the extrusion width value will be reduced once again down to 0,5 mm.

Trial 9 (Type-A)

The result of the ninth attempt, in Figure 133, still exhibits problems related to the visible voids. Since the reduction of the extrusion width has proven ineffective, this strategy will be abandoned.

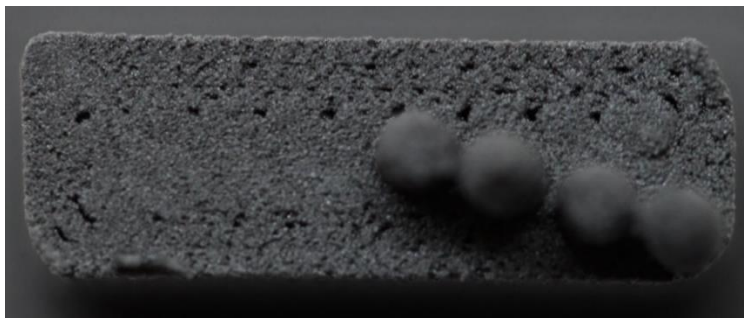


Figure 133. Ninth trial of optimization of the A-type specimen.

The next parameter that will be changed in order to solve the problem is the increase of the overlapping between the perimeter and the infill.

So far, the value of the overlapping was set on 35% but from now on it will be changed to 40%.

Trial 10 (Type-A)

As shown in the Figure 134, the assumption about the influence of the overlapping setting on the presence of voids was right and, in this attempt, compared to the last print, the voids are smaller.



Figure 134. Tenth trial of optimization of the A-type specimen.

Given the effectiveness of this change, the overlapping parameter will be furtherly increased to 45% in the next attempt.

Trial 11 (Type-A)

The result of the eleventh test is reported in Figure 135 and it exhibits a slight enhance of the infill quality. This time the enhance is less marked but still not sufficient, thus the overlap parameter will be raised once again.

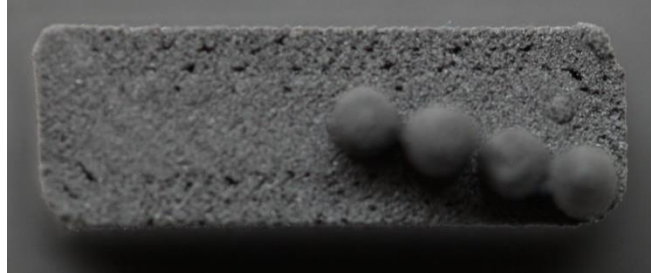


Figure 135. Eleventh trial of optimization of the A-type specimen.

In the next attempt, the overlapping will be increased to 50%. Plus, given that the retained voids are still plainly visible, the only left parameter that may solve the situation is the Extruder multiplier. The extruder multiplier is a parameter that and represents the performed flow rate compared to the nominal flow rate and is used to regulate the actual flow rate. In the next attempt, this parameter will be raised arbitrary from 1,0 to 1,3.

Trial 12 (Type-A)

During the print of the twelfth trial the nozzle clogged, and the filament had to be pushed manually to restart to print again. This is the reason why in the *Figure 136* the second to last layer is missing.

The layer printed after the nozzle clogging, shown in *Figure 136 (a)*, exhibited a good overlapping between the perimeter loops, but also voids at the interface between the infill and perimeter. Anyway, the presence of voids in the between of the infill and the perimeter loops is not a relevant and reliable information since usually the layer below, missing in this case, helps to fill the layer above.

The reason of the nozzle clogging is plausibly the high flow rate due to the change of the Extruder Multiplier, but at the same time it's possible to see in *Figure 136 (b)* that the lateral surface of the specimen benefits from the increased flow rate because is free from pores.

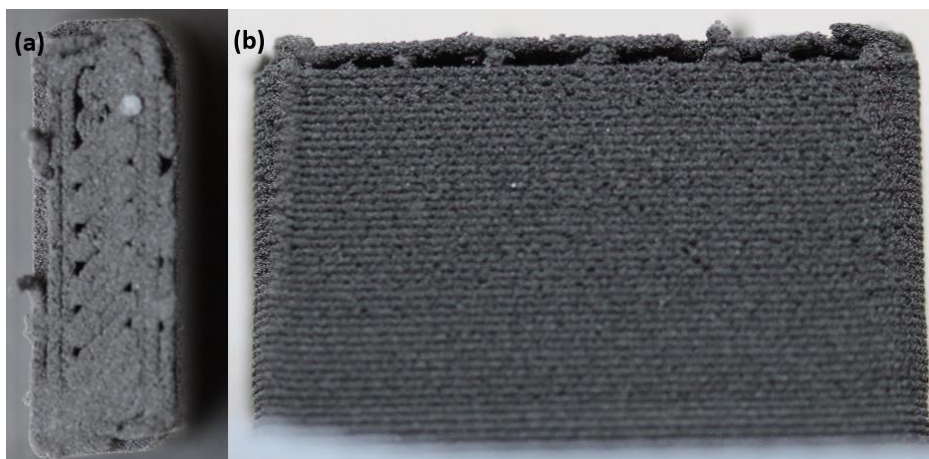


Figure 136. Twelfth trial of optimization of the A-type specimen: (a) Top View; (b) Lateral View.

The quality achieved in this print was satisfying, except for the problem related to the nozzle clogging. Thus, the new strategy will be the slight decrease of the extrusion width to preserve the quality achieved and at the same time prevent the nozzle clogging. In this case the Extruder Multiplier will be decreased from 1,3 to 1,2.

Trial 13 (Type-A)

The increasing of the Extruder Multiplier was a correct and effective solution. In the *Figure 137(a)* voids are not detected. In the lateral view of the specimen, in *Figure 137(b)*, the raster quality is good, and the presence of voids is very limited. In the *Figure 137(c)*, the thinner part of the specimen also unveils a good quality of the surface because the presence of voids was not detected.

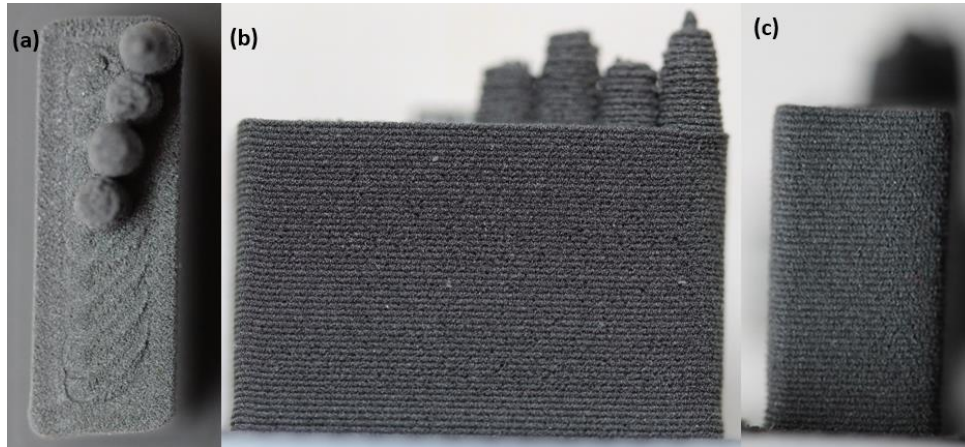


Figure 137. Thirteenth trial of optimization of the A-type specimen: (a) Top View; (b) Lateral View; (c) Behind View.

Trial 1 (Type-B)

The printing parameters found for the specimen Type-A, applied to perform the specimen Type-B, as visible in the *Figure 138(a)*, resulted in a successful print free from pores and holes. The main drawback of this combination is the poor geometrical accuracy exhibited in the lateral surfaces of the specimen. In the *Figure 138(b)*, it's possible to see that the lower part of the print suffers of the so called “elephant foot” defect, due to the temperature effect. Plus, the right side shows a domed face due to the printing of a

slender structure. A remarkable aspect in the specimen is the total absence of pores in the raster when is viewed from the sides.

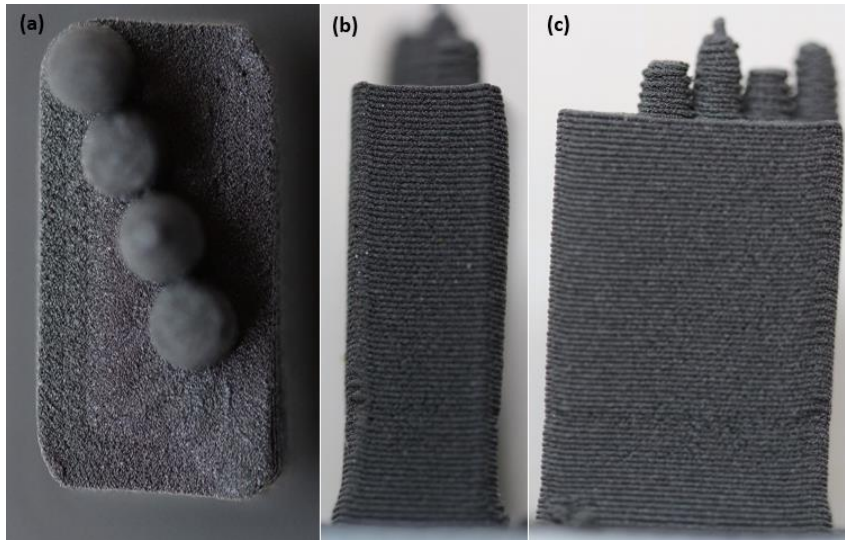


Figure 138. First trial of optimization of the B-type specimen: (a) Top View; (b) Behind View; (c) Lateral View.

Again, in the Figure 138(c) is visible that the surface quality is acceptable also on the lateral surface, free of voids and pores.

Trial 1 (Type-C)

In the Figure 139, the first attempt to print the Type-C specimen was successful achieved. In the Figure 139(a), no voids and pores are detected. Furthermore, a consistent superposition between infill and perimeter loops. In the Figure 139(b) and Figure 139(c) some pores are visible in the raster. The pores may be due to the length of the side to be deposited, long enough to cause the stretching of the deposited material.

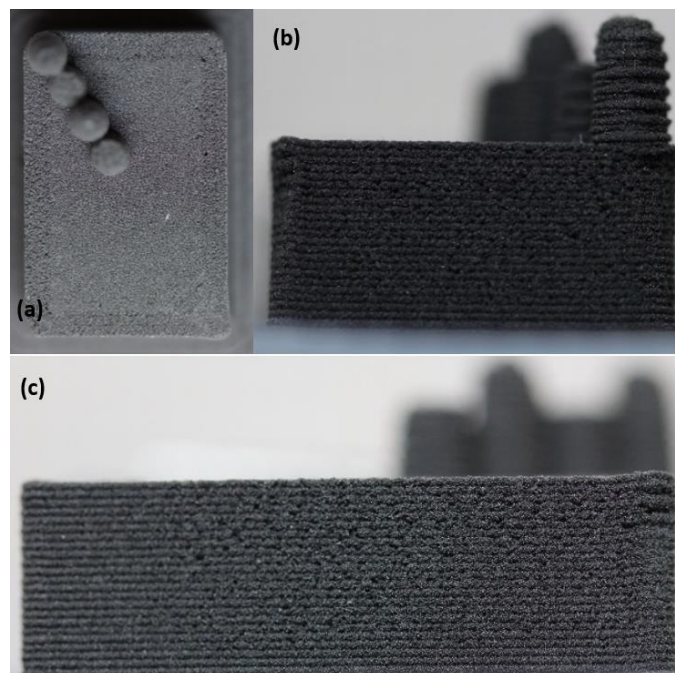


Figure 139. First trial of optimization of the C-type specimen: (a) Top View; (b) Lateral View; (c) Behind View.

However, the quality obtained is reputed good enough to proceed with the batch printing.

5.3.3.2. Batch print

The first approach tried consisted in printing samples one at a time, to avoid oozing problems during the travelling among the components. This observation led to the decision to print all specimens according to the layout shown in Figure 140 that provides a sufficient spacing to avoid already mentioned problem. This way to print the components is called the “object-by-object” strategy.

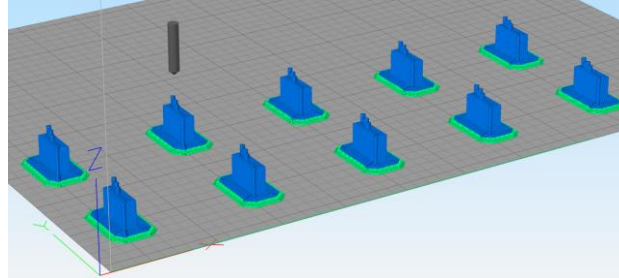


Figure 140. Preview of the first layout tried to print A-type specimens.

This layout was not successful because not all components have been printed. As displayed in the *Figure 141(a)*, the extrusion got worse and worse at every specimen until the clogging of the nozzle. The clogging of the nozzle was a critical problem caused by the grinding of the filament, depicted in *Figure 141(b)*, with consequent stop of the print.

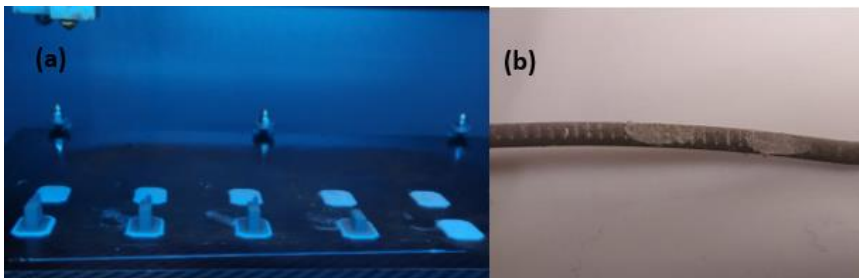


Figure 141. Bad layer strategy: (a) failed print; (b) grinded filament.

This problem remarks how, even after the parameter optimization, some effect due to the increase of the path of deposition may lead to new and unpredicted effects.

The second layout, depicted in *Figure 142*, consists in a common raft base with all components nearby. The adopted deposition strategy is called the “layer-by-layer” strategy.

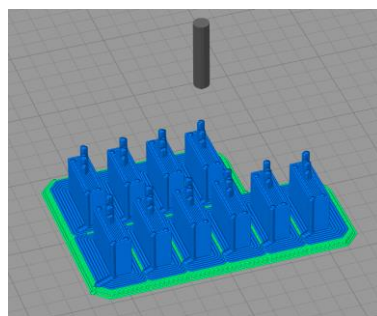


Figure 142. Preview of the second layout tried to print A-type specimens.

The result of this choice is depicted in *Figure 143* and shows clearly that no problems were experienced in the printing of the batch of the specimens Type A and B without the need to change the parameters.

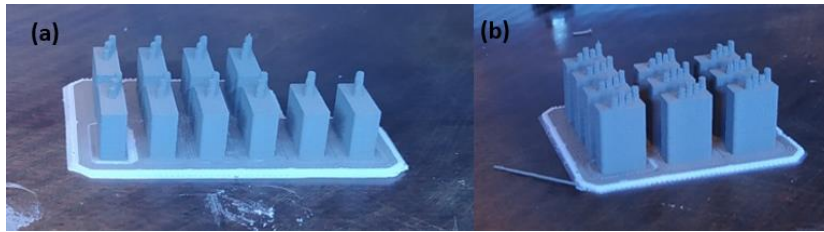


Figure 143. Batch printing: (a) A-type specimens; (b) B-type specimens.

Some issue was found during the printing on the batch of type-C specimens. As depicted in the *Figure 144*, the failure occurred during the deposition of the first layer of part material. An interpretation that justifies the fail of the current print and justifies the success of the print of the previous batches is the amount of material deposited in the first layer. In the printing of the batches of specimens type-A and type-B, the material deposited in the first layer was less than the material required in this case. The result of this problem is an increased risk of nozzle clogging that led to the print failure.



Figure 144. Failed print of the batch of C-type specimen.

This problem makes it necessary to perform another search for parameters that allows to print the whole batch. This new search is summed in the change of the parameters listed in *Table 25*.

Feature	Previous Value	New Value	How it is involved
Start Point	Closest to the point (0, 0)	Optimize for fastest printing speed	The optimized of the start point decrease the travelling distance helping to keep the nozzle-pressure more stable.
Ooze Shield Outlines	6	3	A smaller number of outlines decrease the risk of nozzle clogging due to the excess of material.
Raft Separation Distance	0,18 mm	0,26 mm	The increase of the raft separation distance help to reduce the risk of nozzle clogging due to the poor gap available to deposit the material.

Table 25. Changing of the printing parameters to solve the problem related to the nozzle clogging.

The optimization succeeded and, as shown in *Figure 145*, the print of the type-C specimens with respective pins was achieved.



Figure 145. Batch printing of C-type specimens.

5.3.3.3. Post-process

The post-process includes the operations of the removal of the brim structure and the dissolution of the raft structure.

The first step is the removal of the raft structure made in HIPS. The removal of the support material, whose evolution in time is shown in *Figure 146*, is performed through the immersion of the batch in a tank full of d-limonene.

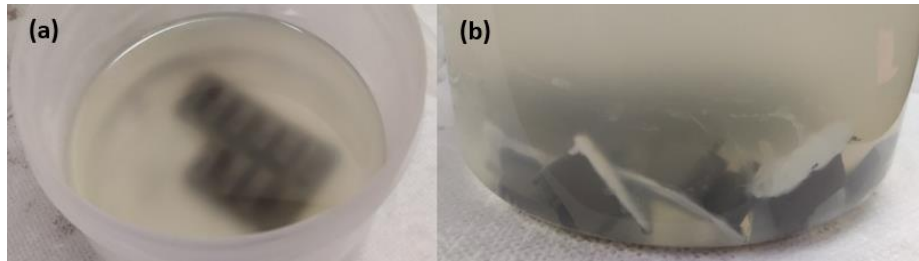


Figure 146. HIPS removal process: (a) batch status after the immersion; (b) batch status after 4 hours in the tank.

After around eight hours, the HIPS is completely vanished and the brim structure results so weak that is easy to remove it without excessive efforts.

When the HIPS is no more visible, all samples are removed from the tank and left on a napkin under hood, as shown in *Figure 147*, for one hour in order to let the retained solvent evaporate.



Figure 147. Drying process after the HIPS removal.

In the end, the assignment of the identification number is performed by breaking all unnecessary pins with a plier. The order by which to execute the breaking of the pin and the removal of the raft is irrelevant, in

fact, in the *Figure 148* is shown that the pins removal process for the type-C specimen batch was performed before the removal of the HIPS-made raft.



Figure 148. *Type-C specimens after the pins removal process.*

5.4. Challenges encountered in the study

5.4.1. Adhesion of the first layer

Some materials may have adhesion problems with the bed because of several reasons. One of the explanations behind this can be the bed temperature or sometimes it may depend on the nature and chemical compatibility between the filament and the bed material.

Often, this problem is correlated to the calibration of the bed that consists in the bed levelling. When the bed is not perfectly horizontal, the result is a non-constant gap between the nozzle and the bed. The immediate result of this is a non-constant first layer height with consequent poor control on the dimensional accuracy.

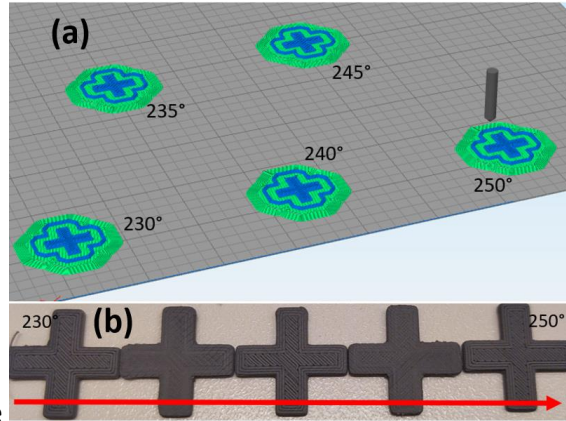
Moreover, high metal powder loaded filaments shows higher thermal shrinkages compared to the thermoplastics. This problem is exacerbated by larger prints, which increases the likelihood of the first layer being detached during printing and, therefore, the task failure.

The solution adopted to overcome all those problems consists in printing a raft structure, an auxiliary structure, with the support material. The support material, as said before, is the HIPS and during the test campaign has shown good adhesion properties with the ULTRAFUSE 316L and the Ti64-5 Filamet filaments.

Levelling of the printing bed

A correct levelling of the printing bed should be done in a manner that allows a good adhesion of the first layer regardless the use of the part material or the support material.

Several trials have been done with a spirit level, but this tool was not accurate enough to allow a correct



calibration. As depicted in the

Figure 149, a print was run after the levelling with the spirit level. There were evident differences in the resulting print because the raster-to-raster gap air was depending on the local position of the component on the printing bed.

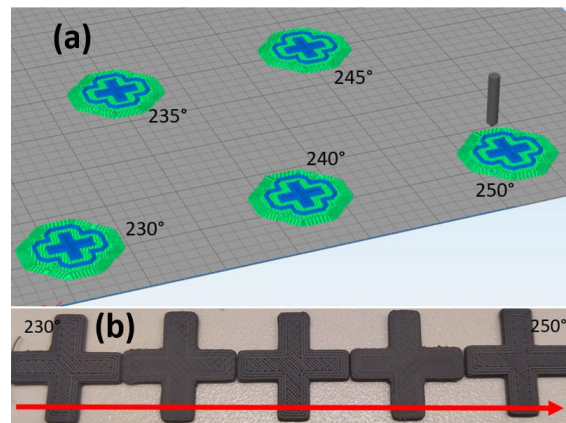


Figure 149. A print run that shows the effect of a non-levelled bed: (a) local position on the printing bed, (b) result of the print.

The solution to level the bed consists in printing some squares at the corners of the printing bed, depicted in Figure 150, and during the deposition adjusting the gap between the nozzle and the bed, time by time by means of the screws under the bed until we reach a good adhesion of the support material.

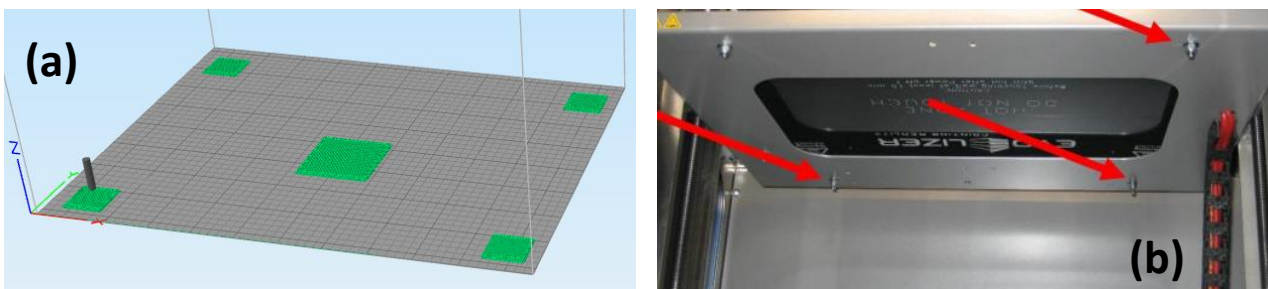


Figure 150. Bed adjustment procedure: (a) a view of the gcode file performed, (b) a view of the bottom part of the bed with adjustment screws.

At the end of the adjustment procedure, the quality of the material deposition performed in all the squares printed should be homogeneous and as close as the one depicted in Figure 151.



Figure 151. Square printed during the adjustment of the plate.

Gap between the nozzle tip and printing bed

The printer is not provided with probes or systems that can detect the real gap standing between the nozzle and the bed, hence it's difficult to measure the absolute distance between the bed and the gap. Nevertheless, this setting is important because it heavily affects the quality of the first layer and influences the quality of sequent layers. In manner to better understand the importance of this parameter, we can compare the result of two prints, depicted in *Figure 152*, in which the gap was modified by 0,1 mm.



Figure 152. Effect of the gap between the nozzle tip and the bed during the deposition of the first layer.

In the picture, the print marked with “-0,1” is the one whose gap is shorter while the one marked with “+0,1” shows a gap 0,1 mm larger.

In the “-0,1” sample the first layer is more compact, and the ink used to mark it is not able to seep through the raster air gaps while in the “+0,1” sample the ink can seep in the gaps resulting in several black lines. The practical consequence of this is an enhancement of the adhesion of the first layer since the “-0,1” sample was more difficult remove.

This consideration is useful for correctly choosing the look that a proper bottom layer should have.

5.4.2. Print exposure to the solvent agent

During the preliminary prints with the ASA material, the exposure of the polymer to the solvent agent have shown an interesting delamination effect and furthermore, the component depicted in *Figure 153* was quite softened. The exposure time was about 48 hours. This effect was not predicted but this event

underlined that even though the component doesn't chemically react with the solvent it doesn't mean that the solvent won't affect the component in any way.



Figure 153. ASA tensile test specimen exposed to the d-limonene for 48 hours.

This observation led to the need to understand the effect of a long exposure of different materials to the limonene agent, a test has been ran on the ULTRAFUSE 316L and on the Titanium 64-5 Filament.

After the exposure of some waste component in the solvent for 48 hours, as depicted in *Figure 154*, sign of delamination or softening were not detected. The rough surface shown by the ULTRAFUSE 316L component was not chargeable to the solvent exposure, but it was due to bad setting of parameters.

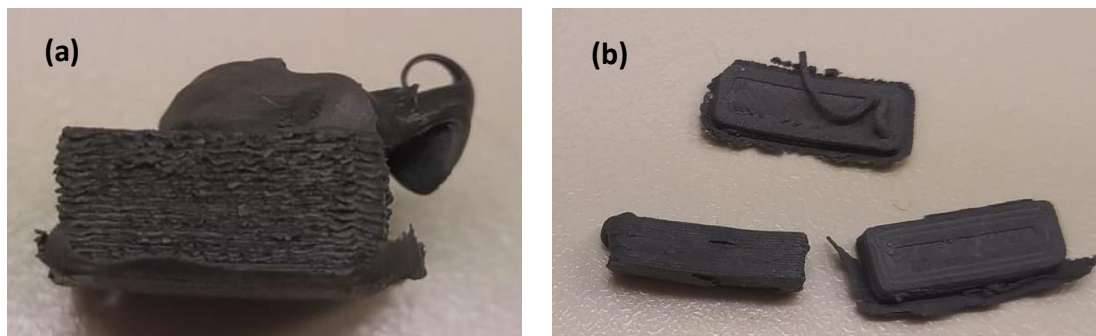


Figure 154. Samples exposed for a long period to the solvent agent: (a) ULTRAFUSE 316L, (b) Titanium 64-5 Filamet.

This test confirmed the compatibility between the used material and the solvent agent but in other cases where delamination-correlated problems do happen, the long exposure to the solvent should be avoided.

A possible solution to overcome this problem consists in adopting an ultrasonic cleaner to speed-up the dissolution reaction decreasing the overall time of exposure with the solvent.

5.4.3. Pressure of the nozzle

In the Bowden extruders, the feeding system is very far from the extrusion site and the section of filament in the between tend to be compressed. The elasticity of this section of filament led to a variation in the pressure present in the melting chamber, especially in the preliminary stage of the print. If no countermeasures are taken, the final effect of this is a non-constant extrusion width or sometimes a bad adhesion problem.

The solution proposed for this problem consists in the reduction of the length of the Bowden tube when it is possible and the adoption of the so-called skirts or brims. Skirts and brims consist in printing loops surrounding the print in the first layer. The adoption of those additions structures helps to reach the steady in-service pressure. The difference between skirts and rafts, as depicted in *Figure 155*, is that brims are connected to the first layer while skirts keep a constant offset from the component. The brims are employed especially in the print small components to enhance the cross section of the first layer when the existing one is insufficient.

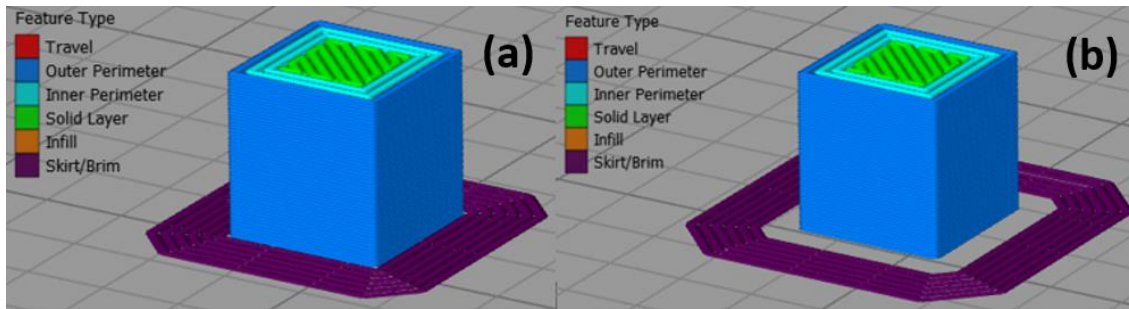


Figure 155. Auxiliary structures applied on a cube: (a) brim and (b) skirt.

5.4.4. Equalization of nozzles position

Some cutting-edge double-extruder printers are provided with systems that move alternatively the position of the two nozzles up and down so that the resting nozzle does not interfere with the deposition process.

In this case, the nozzle carrier embedded in the EVO Lizer 11 is provided with screws that fasten the nozzles in a fixed position by means of some screws, as depicted in *Figure 156*.



Figure 156. Detail picture of the nozzle unit with fixing screws circled in red [46].

The equalization of the nozzles position needs proper care because if neglected, could lead to scars on the print and in some case even to the failure of the print. It may happen that the position of the nozzle at rest is lower than the one that is running resulting in grooves like the one shown in *Figure 157*. In severe cases the misalignment can lead to the removal of the deposited material and destruction of just built layer.

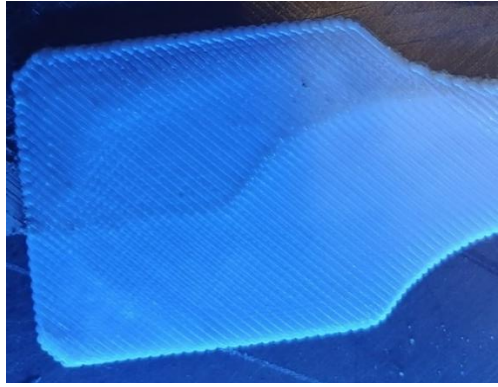


Figure 157. Groove due to a bad equalization of the nozzles position.

The matured strategy consists in an initial adjustment of the support material extruder, as if the printer is a mono-extruder printer. The choice of starting the procedure by adjusting the support material is because once adjusted, the height of the nozzle won't be re-adjusted anymore. Contrary, different part materials need different nozzles and every time that we substitute it, we must re-calibrate the extruder height.

Given the problems mentioned, the proposed solution consists in a tailored calibration device, depicted in *Figure 158*.

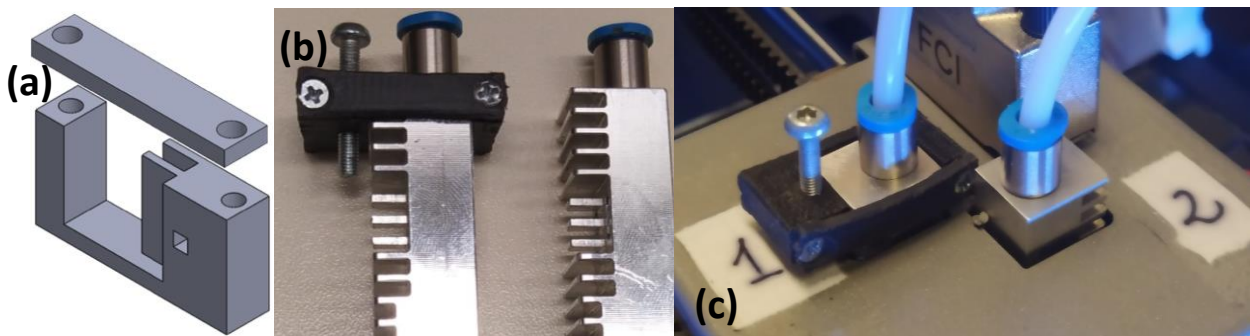


Figure 158. Gap-adjuster device: (a) CAD drawing, (b) Installation on the nozzle unit, (c) Installation on the carrier extruder.

The working principle is hereafter described. First, the fixing screws are loosened to make the nozzle slide in its seat. During the calibration, the nozzle temperature of both the nozzles must be the operating temperature so we can include the effect of the actual thermal elongation. The starting position of the part material nozzle should be sufficiently far from the plate and should be ensured thanks to the screw of the adjusting device, shown in the *Figure 158* (b).

Following, a parallelepiped must be printed with the support material. Once the parallelepiped is printed, the part material nozzle comes slowly closer to that last layer deposited, by loosening the screw shown in *Figure 158*. (c). During the descent of the nozzle, the extruder carrier should be drifted manually back and forth. If the part material nozzle is too low, some scratches will be reported on the surface of the parallelepiped, suggesting that the nozzle should be slightly lifted. Once the adjustment has been done, we can tighten up all the screws.

Section 6

6. Economic characterization with a cost model

The economic characterization of the performed prints will consist in an estimation of costs to sustain to realize the prints assuming an industrial production.

The total cost of the print will be evaluated as sum of all contributions mentioned in the Eq. (3).

$$C_{Total} = C_M + C_{Energy} + C_{Solvent} + C_{D\&S} \quad (3)$$

Where:

- $C_{Total} \equiv$ Total cost [€]
- $C_M \equiv$ Cost of the material exploited in the deposition process [€]
- $C_{Energy} \equiv$ Cost due to the energy consumption [€]
- $C_{Solvent} \equiv$ Cost of the exploited solvent [€]
- $C_{D\&S} \equiv$ Cost of the debinding and sintering process [€]

In this characterization, direct labour costs and costs due to licenses of software are neglected. The motivation of this is the choice of simulate a real scenario in which the cost of the licenses is distributed in a consistent number of components and the time employed in the handling of the prints is so little that the associated direct labour cost is negligible.

6.1. Cost of the material exploited in the deposition process

The cost associated to the part material is the portion of material used during the process. This expense is connected to the cost of the whole spool.

The first information immediately available is the price of the spool (including all taxes) and the weight of the spool. Moreover, in the technical datasheet is possible to collect the density of the spool and the diameter of the filament.

Assuming to virtually uncoil the spool, the filament can be seen as an extremely slender cylinder whose length is computable with the Eq. (4), Eq. (5) and Eq. (6).

$$S_{Filament} = \frac{\pi \cdot d_{Filament}^2}{4} \quad (4)$$

$$V_{Tot} = \frac{W_{Total}}{\rho_{Filament}} \quad (5)$$

$$L_{Tot} = \frac{1000 \cdot V_{Tot}}{S_{Filament}} \quad (6)$$

With:

- $d_{Filament}$ \equiv Diameter of the filament [mm]
- $S_{Filament}$ \equiv Cross-section of the filament [mm²]
- W_{Total} \equiv Weight of the spool [g]
- $\rho_{Filament}$ \equiv Density of the filament [g/cm³]
- V_{Tot} \equiv Total volume of the coiled filament [cm³]
- L_{Tot} \equiv Total length of the coiled filament [mm]

The slicer software is capable to suggest the amount of filament that will be involved in the print by consulting it in the Preview Panel.

In case of double-extrusion process, it's possible to know the amount of both materials just by consulting the preview panel of the print in order to get the overall amount of filament (with no specification on the materials) and then re-consult it without the raft structure in order to get the total amount of part material used. Then, the support material will be evaluated according to the Eq. (7).

$$l_{S.M.} = l_{Overall} - l_{P.M.} \quad (7)$$

With:

- $l_{S.M.}$ \equiv Length of the deposited filament of support material [mm]
- $l_{Overall}$ \equiv Overall length of the deposited filament [mm]
- $l_{P.M.}$ \equiv Length of the deposited filament of part material [mm]

In our case the whole batch can't be manufactured in one print, also called "job". Thus, in order to compute the total length of the batch, it's recommended to adopt the Eq. (8) and the Eq. (9).

$$L_{P.M.} = l_{P.M.} \cdot \frac{n_{Batch}}{n_{Job}} \quad (8)$$

$$L_{S.M.} = l_{S.M.} \cdot \frac{n_{Batch}}{n_{Job}} \quad (9)$$

With:

- n_{Batch} \equiv Number of components planned in the batch [mm]
- n_{Job} \equiv Number of components that can be printed during a job [mm]
- $L_{P.M.}$ \equiv Total length of filament of part material required to print the batch [mm]
- $L_{S.M.}$ \equiv Total length of filament of support material required to print the batch [mm]

Once we have the length of the filament deposited, the cost associated to the part material and the support material respectively, is shown in the Eq. (10) and in Eq. (11).

$$C_{P.M.} = C_{P.M.Spool} \cdot \frac{L_{P.M.}}{L_{Tot}} \quad (10)$$

$$C_{S.M.} = C_{S.M.Spool} \cdot \frac{L_{P.M.}}{L_{Tot}} \quad (11)$$

With:

- $C_{P.M.}$ ≡ Overall cost of the deposited part material [€]
- $C_{S.M.}$ ≡ Overall cost of the deposited support material [€]
- $C_{P.M.Spool}$ ≡ Cost of the spool of part material [€]
- $C_{S.M.Spool}$ ≡ Cost of the spool of support material [€]

At the end, the cost of the material is given by the sum of the two contributions, as shown in the Eq. (12).

$$C_M = C_{P.M.} + C_{S.M.} \quad (12)$$

In the Table 26, Table 27 and in Table 28 are collected all pertinent information to perform the cost evaluation.

Information	Value	Source
$d_{Filament}$	1,75 mm	Technical data sheet
W_{Total} (Part material)	500 g	Technical data sheet
W_{Total} (Support material)	1000 g	Technical data sheet
$\rho_{Filament}$ (Part material)	2,46 g/cm ³	Technical data sheet
$\rho_{Filament}$ (Support material)	1,02 g/cm ³	Technical data sheet
$l_{Overall}$ (Type-A)	5167,8 mm	Preview on the slicer software
$l_{P.M.}$ (Type_A)	4025,5 mm	Preview on the slicer software
$l_{Overall}$ (Type-B)	4863,7 mm	Preview on the slicer software
$l_{P.M.}$ (Type_B)	3982,0 mm	Preview on the slicer software
$l_{Overall}$ (Type-C)	5132,3 mm	Preview on the slicer software
$l_{P.M.}$ (Type_C)	3729,8 mm	Preview on the slicer software
n_{Batch}	10	Preview on the slicer software
n_{Job}	10	Preview on the slicer software
$C_{P.M.Spool}$	784,00 €	Purchase receipt
$C_{S.M.Spool}$	199,50 €	Purchase receipt

Table 26. Data regarding the print of the titanium feedstock.

Information	Value	Source
d_{Filament}	1,75 mm	Technical data sheet
W_{Total} (Part material)	3000 g	Technical data sheet
W_{Total} (Support material)	1000 g	Technical data sheet
ρ_{Filament} (Part material)	4,98 g/cm ³	Technical data sheet
ρ_{Filament} (Support material)	1,02 g/cm ³	Technical data sheet
l_{Overall}	37175,4 mm	Preview on the slicer software
$l_{\text{P.M.}}$	26021,3 mm	Preview on the slicer software
n_{Batch}	7	Preview on the slicer software
n_{Job}	10	Preview on the slicer software
$C_{\text{P.M.Spool}}$	445,83 €	Purchase receipt
$C_{\text{S.M.Spool}}$	199,50 €	Purchase receipt

Table 27. Data regarding the print of the steel tensile test specimens on the XY plane.

Information	Value	Source
d_{Filament}	1,75 mm	Technical data sheet
W_{Total} (Part material)	3000 g	Technical data sheet
W_{Total} (Support material)	1000 g	Technical data sheet
ρ_{Filament} (Part material)	4,98 g/cm ³	Technical data sheet
ρ_{Filament} (Support material)	1,02 g/cm ³	Technical data sheet
l_{Overall}	22067,6 mm	Preview on the slicer software
$l_{\text{P.M.}}$	21389,4 mm	Preview on the slicer software
n_{Batch}	5	Preview on the slicer software
n_{Job}	10	Preview on the slicer software
$C_{\text{P.M.Spool}}$	445,83 €	Purchase receipt
$C_{\text{S.M.Spool}}$	199,50 €	Purchase receipt

Table 28. Data regarding the print of the steel tensile test specimens on the ZX plane.

6.2. Cost due to the energy consumption

This contribution of cost represents the energetic impact of the technology. The time of the print can be estimated in the Preview Panel but often is not realistic value. Hence, the considered value will be the time displayed in the Web Interface at the end of the job.

Therefore, the overall time spent to print the batch will be computed with the Eq. (13).

$$t_{\text{Batch}} = t_{\text{Job}} \cdot \frac{n_{\text{Batch}}}{n_{\text{Job}}} \quad (13)$$

With:

- $t_{Job} \equiv$ Time spent to print a certain number of components in a single job [min]
- $t_{Batch} \equiv$ Overall time required to print all the batch [min]

Given the time of the print, the overall energy absorbed required to realize the batch is calculated with the Eq. (14).

$$E_{batch} = W_{avg} \cdot \frac{t_{Batch}}{60} \quad (14)$$

With:

- $W_{avg} \equiv$ Averaged power consumption of the printer [kW]
- $E_{batch} \equiv$ Overall energy consumption associated to the print of the batch [kWh]

In the end, the cost of the energy is based on the hourly energetic consumption as shown in the Eq. (15).

$$C_{Energy} = H_{Consumption} \cdot E_{batch} \quad (15)$$

With:

- $H_{Consumption} \equiv$ Hourly energetic consumption [€/kWh]

The Figure 159 shows that in the last times the energy cost is having an anormal trend, hence it will be kept under control by using the average cost on a period starting from the year 2020.

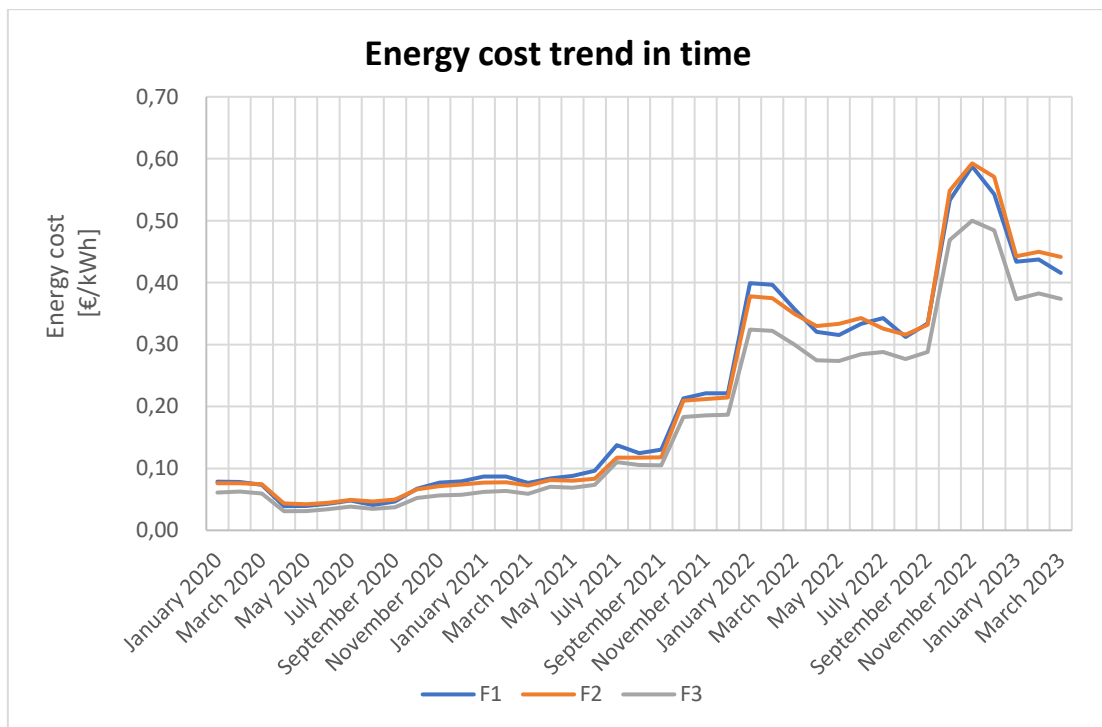


Figure 159. Energy cost trend in time domain: F1(Monday-Friday 8:00-19:00); F2(Monday-Friday 7:00-8:00); F3(Monday-Saturday 23:00-7:00, Sunday and Holidays).

By assuming the worst-case scenario, with the cost profile F1, the averaged energy price $H_{\text{Consumption}}$ is 0,214 €/kW.

In the *Table 29* are collected all pertinent information to perform the cost evaluation.

Information	Value	Source
t_{Job} (ULTRAFUSE 316L_XY)	873 min	Web interface of the 3D printer
n_{Batch} (ULTRAFUSE 316L_XY)	7	Preview on the slicer software
n_{Job} (ULTRAFUSE316L_ZX)	10	
t_{Job} (ULTRAFUSE 316L_ZX)	1433 min	Web interface of the 3D printer
n_{Batch} (ULTRAFUSE 316L_ZX)	5	Preview on the slicer software
n_{Job} (ULTRAFUSE316L_ZX)	10	
t_{Job} (Filamet Ti64-5)	210 min	Web interface of the 3D printer, equal for Type-A, Type-B and Type-C specimens
n_{Batch} (Filamet Ti64-5)	10	Preview on the slicer software
n_{Job} (Filamet Ti64-5)	10	
W_{avg}	250 W	Technical data sheet

Table 29. Electric consumption data.

6.3. Cost of the solvent

The cost of the solvent consists in the economic contribution resulting from the use of a certain part of the solvent agent during the removal of the raft structure.

This cost occurs in the manufacturing of the components made with the titanium feedstock because the components is small, and the manual removal of the raft structure may result risky. The tensile specimens printed with the steel filament do not need the solvent because the components are big enough to allow the manual peeling of the raft structure.

In the Eq. (16) is reported the calculation of the cost associated with the solvent employment.

$$C_{\text{Solvent}} = C_{\text{Tot_Solvent}} \cdot \frac{V_{\text{Employed}}}{V_{\text{Tot}}} \quad (16)$$

With:

- $V_{\text{Employed}} \equiv$ Volume of solvent employed in the raft removal [dm³]
- $V_{\text{Tot}} \equiv$ Volume of solvent contained in the purchased tank [dm³]
- $C_{\text{Tot_Solvent}} \equiv$ Cost of the solvent tank [€]

In the *Table 30* are collected all pertinent information to perform the cost evaluation.

Information	Value	Source
V_{Employed}	0,2 dm ³	
V_{Tot}	1 dm ³	[71]
$C_{\text{Tot_Solvent}}$	35,94 €	[71]

Table 30. Data regarding the solvent agent employed.

Since the same solvent portion is adopted in the raft removal of the three different batches, in the evaluation of the price we will assume just one third of the C_{Solvent} .

6.4. Cost of the debinding and sintering process

The cost due to the debinding and sintering process is directly reported as price demanded by the company to which the batch was entrusted.

In the *Table 31* are gathered the costs $C_{D\&S}$ required to perform the process for both the materials.

Information	Value	Note	Source
$C_{D\&S_UF316L}$	72 €	Maximum weight is 1 Kg	[72]
$C_{D\&S_Ti64-5}$	540 €	Maximum employable volume is (L x W x H) 200 x 70 x 70 mm	[73]

Table 31. Debinding and sintering information.

Thus, the total cost $C_{D\&S}$ for the ULTRAFUSE 316L, by assuming to pay just the quantity of weight used, will be evaluated with the Eq. (17).

$$C_{D\&S_UF316L} = c_{D\&S_UF316L} \cdot \frac{3 \cdot n_{\text{job}} \cdot w_{\text{specimen}}}{1000 \text{ g}} \quad (17)$$

With:

- $c_{D\&S_UF316L} \equiv$ Cost of a single D&S process for the ULTRAFUSE 316L prints
- $w_{\text{specimen}} \equiv$ Weight of a single specimen, equal to 43 g.
- $C_{D\&S_UF316L} \equiv$ Total cost of the process for the ULTRAFUSE 316L prints

For what concerns the $C_{D\&S_Ti64-5}$ the equation is different because given the little space available, the only constraint is about the space. Considering that the group of a specimens Type-A, B and C can be sorted so they occupy an area of 2 x 6 cm², we can fit all the specimens in the available space of the oven. In the end, the total cost $C_{D\&S}$ for the Titanium 64-5 Filamet is reported in the Eq. (18).

$$C_{D\&S_Ti64-5} = c_{D\&S_Ti64-5} \quad (18)$$

With:

- $c_{D\&S_UF316L} \equiv$ Cost of the D&S process for a batch of Titanium 64-5 Filamet prints
- $C_{D\&S_UF316L} \equiv$ Total cost of the process for the Titanium 64-5 Filamet prints

Section 7

7. Results

In this chapter are mentioned all the information gathered and elaborated during the study.

7.1. Dimensional characterization

7.1.1. ULTRAFUSE 316L green part tensile test specimens

All measurements concerning the length are performed with the calliper while the measure regarding the width and the thickness are performed with the micrometer. Thereby, the measurement uncertainty should be meant as the instrumental uncertainty of the respective instrument employed.

By referring to the ISO standard, the cross section was measured three times and in the *Figure 160* are pointed all areas of the measurement with the respective name associated.

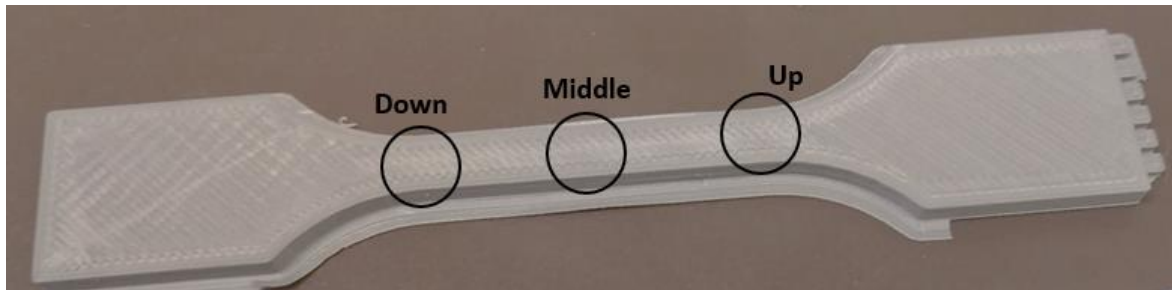


Figure 160. Spots of the acquisition of the cross section.

In the Table 32, Table 33 and in Table 34 are reported all acquisition regarding the three different orientations.

Direction of the component	Total length L [mm]	Up		Middle		Down	
		Width [mm]	Thickness [mm]	Width [mm]	Thickness [mm]	Width [mm]	Thickness [mm]
X1	137,64	7,681	3,911	7,668	3,940	7,662	3,904
X2	137,84	7,694	3,852	7,772	3,925	7,698	3,901
X3	137,64	7,652	3,904	7,595	3,967	7,663	3,878
X4	137,83	7,873	3,941	7,848	3,910	7,851	3,930
X5	137,64	7,350	3,794	7,319	3,777	7,346	3,771
X6	137,75	7,789	3,927	7,768	3,910	7,724	3,937
X7	137,71	7,623	3,940	7,749	3,977	7,668	3,967
X8	137,68	7,652	3,922	7,663	3,925	7,658	3,978
X9	137,86	7,633	3,960	7,636	3,903	7,686	3,943
X10	137,75	7,773	3,844	7,663	3,880	7,808	3,874

Table 32. X-axes oriented specimen measurements.

Direction of the component	Total length L [mm]	Up		Middle		Down	
		Width [mm]	Thickness [mm]	Width [mm]	Thickness [mm]	Width [mm]	Thickness [mm]
Y1	137,76	7,647	3,876	7,633	3,847	7,615	3,883
Y2	137,74	7,626	3,868	7,602	3,882	7,597	3,868
Y3	137,7	7,623	3,894	7,626	3,819	7,609	3,876
Y4	137,71	7,586	3,850	7,590	3,878	7,570	3,873
Y5	137,68	7,672	3,891	7,670	3,841	7,651	3,870
Y6	137,66	7,679	3,927	7,594	3,848	7,594	3,895
Y7	137,66	7,636	3,832	7,625	3,893	7,615	3,859
Y8	137,66	7,679	3,879	7,583	3,871	7,644	3,871
Y9	137,65	7,588	3,888	7,561	3,884	7,546	3,870
Y10	137,67	7,633	3,846	7,678	3,811	7,672	3,812

Table 33. Y-axes oriented specimen measurements.

*Specimen broken during the handling operations.

Direction of the component	Total length L [mm]	Up		Middle		Down	
		Width [mm]	Thickness [mm]	Width [mm]	Thickness [mm]	Width [mm]	Thickness [mm]
Z1	136,67	7,474	3,949	7,460	3,938	7,447	3,955
Z2	136,79	7,522	3,967	7,552	3,958	7,432	3,963
Z3	136,83	7,546	3,933	7,534	3,928	7,496	3,928
Z4*							
Z5	136,65	7,451	3,994	7,426	3,984	7,415	3,975
Z6	136,64	7,466	3,990	7,457	3,987	7,461	4,009
Z7	136,65	7,461	3,984	7,450	3,983	7,459	3,975
Z8	136,61	7,498	3,998	7,496	4,005	7,504	4,019
Z9	136,64	7,479	3,922	7,461	3,922	7,466	3,919
Z10	136,62	7,494	4,154	7,485	3,985	7,478	3,985

Table 34. Z-axes oriented specimen measurements

In the end, the elaboration and the comparison of the actual values with the theoretical values are listed in the Table 35.

	Length	Width	Thickness	
X-axes oriented specimens	Theoretical value [mm]	137,32	7,200	3,780
	Mean value [mm]	137,73	7,672	3,906
	Standard deviation [/]	0,086	0,134	0,054
	Relative error [%]	0,30%	6,56%	3,34%
Y-axes oriented specimens	Mean value [mm]	137,69	7,621	3,867
	Standard deviation [/]	0,038	0,037	0,026

Z-axes oriented specimens	Relative error [%]	0,27%	5,85%	2,29%
	Mean value [mm]	136,68	7,477	3,974
	Standard deviation [/]	0,078	0,034	0,046
	Relative error [%]	0,47%	3,84%	5,14%

Table 35. Comparison of actual values with theoretical values.

7.1.2. Filamet 64-5 green part shrinkage specimens

The dimensions of the Ti6Al4V specimens as the green part, measured with the KEYENCE VR-5000, are listed in the Table 36.

Specimen	Type-A			Type-B			Type-C		
	X [mm]	Y [mm]	Z [mm]	X [mm]	Y [mm]	Z [mm]	X [mm]	Y [mm]	Z [mm]
1	5,357	15,546	10,183	10,485	5,350	15,049	15,263	10,151	5,083
2	5,347	15,433	10,076	10,503	5,270	15,020	15,308	10,150	5,085
3	5,450	15,431	10,223	10,459	5,275	15,039	15,299	10,317	5,057
4	5,349	15,377	10,001	10,526	5,337	14,940	15,323	10,290	5,134
5	5,338	15,505	10,063	10,393	5,277	15,037	15,344	10,245	5,095
6	5,372	15,490	10,135	10,530	5,340	15,059	15,311	10,191	5,107
7	5,259	15,422	10,070	10,482	5,294	15,253	15,311	10,309	5,092
8	5,386	15,376	10,104	10,444	5,243	15,115	15,227	10,189	5,100
9	5,231	15,546	10,004	10,488	5,326	15,089	15,267	10,214	5,103
10	5,424	15,443	10,089	10,384	5,472	15,012	15,221	10,214	5,082

Table 36. Dimensions of the shrinkage specimens made with the Filamet 64-5.

7.2. Mechanical characterization

7.2.1. Ti6Al4V (L-PBF) tensile test results

The tensile test, anticipated in the paragraph “**Gripping area design**” (Page 68), was performed at the Department of Mechanical and Aerospace Engineering (DIMEAS) of the Politecnico di Torino (Polytechnical University of Turin).

The results of the tensile tests are reported in the *Figure 161* and in the *Table 37*. The test was performed keeping constant the strain rate at 1 mm/min.

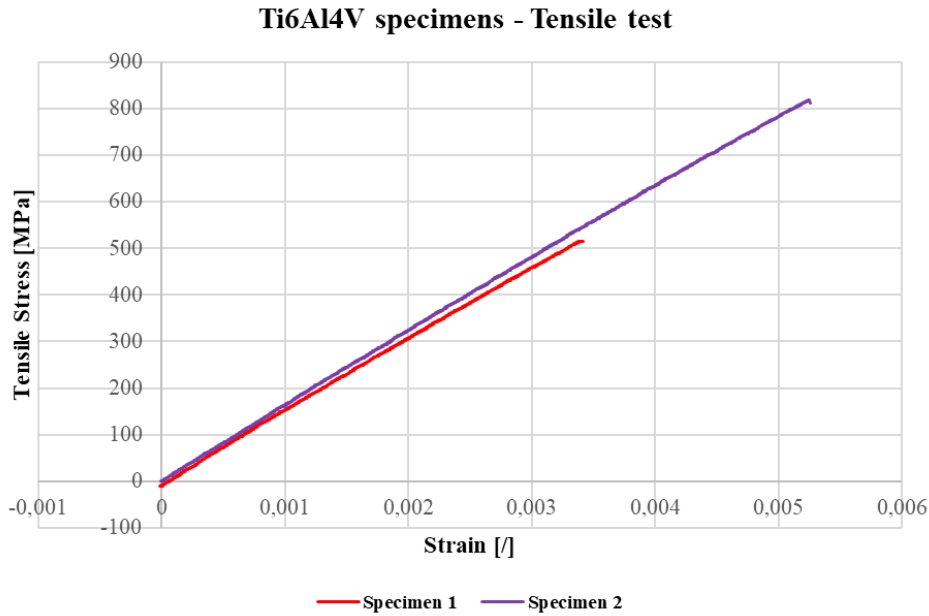


Figure 161. Stress-strain diagram of the two tensile specimens printed via L-PBF.

Specimen identification number	UTS [MPa]	E [MPa]	R²
1	516	156353	0,997
2	818	155170	0,997

Table 37. Ultimate Tensile Test (UTS) and estimated Elasticity Module (E) with relative coefficient of determination of the two tensile specimens.

7.3. Physical characterization

In this paragraph are shortly discussed two tests performed to evaluate qualitatively the electrical and magnetic nature of the two feedstocks in order to help the exploration of new applications.

7.3.1. Electrical characterization

The electrical conductivity was recorded with a multimeter. The result of the measurement shows that both the feedstocks are electrical insulants. An adjunctive measurement was performed with needle probes able to pierce the surface allowing the evaluation of possible shielding effects. The result of this test remarked again a non-conductive behaviour in both the feedstocks.

7.3.2. Magnetic characterization

The magnetic characterization, performed on the green parts, consists in a qualitative test to state the magnetic nature of the two feedstock adopted. In practice, the test consists in the putting the material in contact with a permanent magnet and see the reaction.

This simple test shows that the ULTRAFUSE 316L exhibits a paramagnetic behaviour since the magnet was weakly attracted from components while the Filamet Titanium 64-5 shows non-magnetic features since printed object made with the titanium feedstock didn't react to the exposure with the permanent magnet.

7.4. Economic characterization

In this paragraph are reported all the results about the evaluation of the costs regarding both the feedstocks.

7.4.1. Titanium 64-5 Filamet specimens

In the Figure 162, Figure 163 and Figure 164 are reported the pie charts with contribution of costs in relative and absolute value.

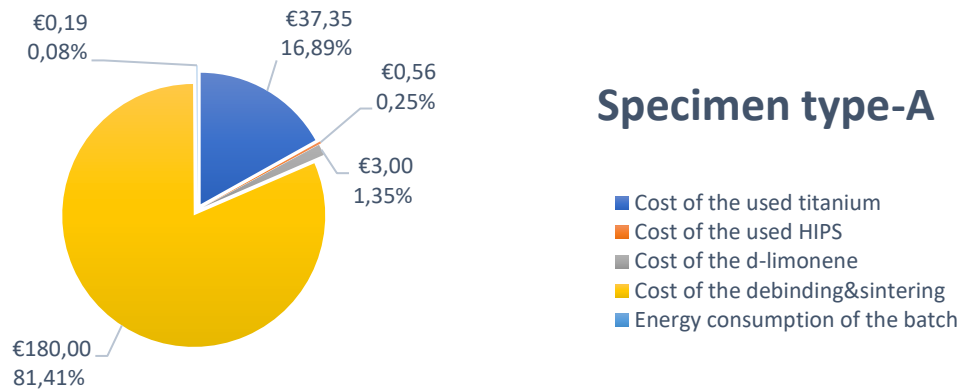


Figure 162. Pie chart of the total cost associated to production of the batch of specimens Type-A.

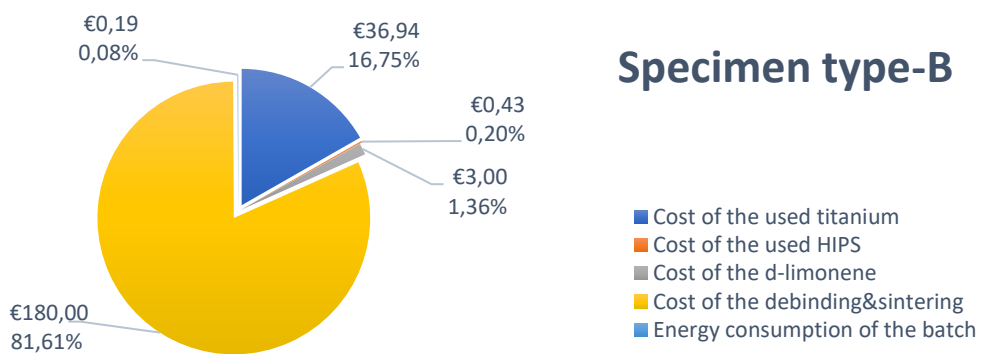


Figure 163. Pie chart of the total cost associated to production of the batch of specimens Type-B.

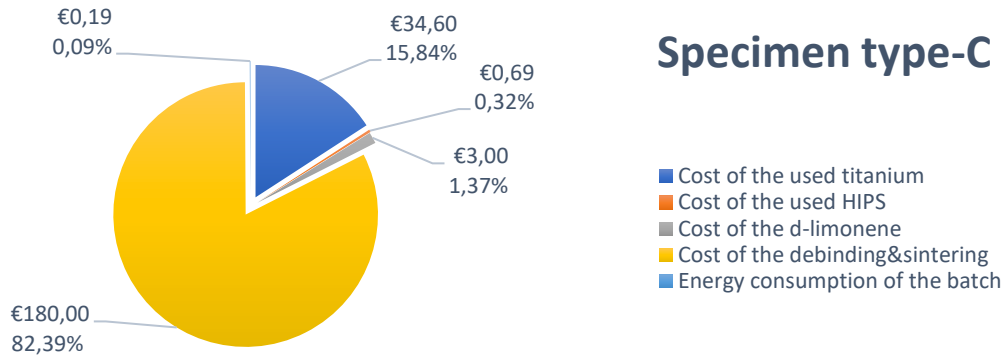


Figure 164. Pie chart of the total cost associated to production of the batch of specimens Type-C.

7.4.2. ULTRAFUSE 316L specimens

In the Figure 165, the pie charts report the contribution of costs in the relative and absolute value required to realize the ULTRAFUSE 316L specimens. X-axes oriented and Y-axes oriented specimens have the same pie chart since the material used and the time of the deposition is the equal.

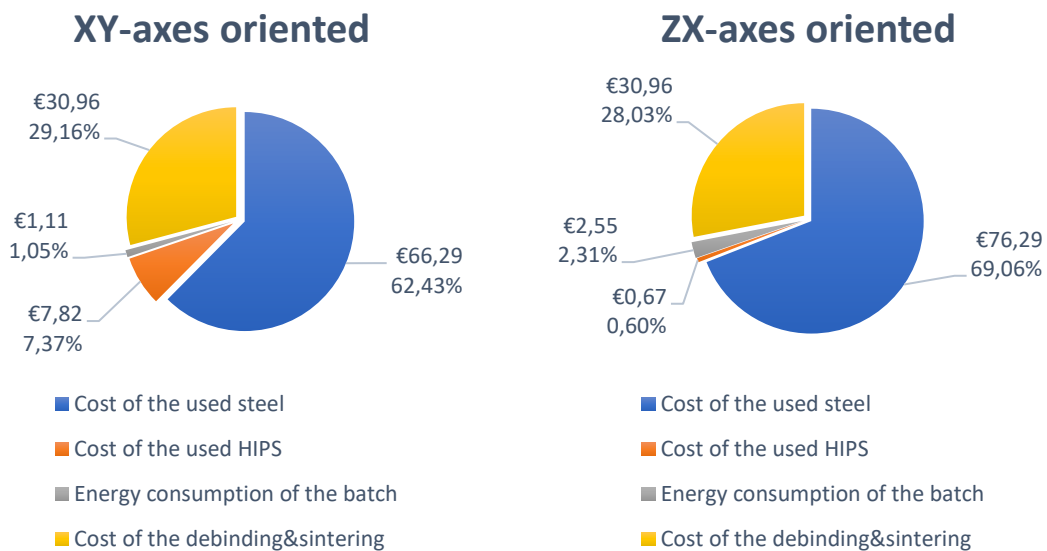


Figure 165. Pie charts of cost contributions associated to the production of the tensile specimens.

Section 8

8. Discussion

The result of the study shows that in the printing of the steel feedstock, the geometry was out of size of about 0,4 mm on the xy plane and about 0,1 mm on the z direction. The same trend is registered in the shrinkage specimens printed with the titanium feedstock.

The tensile test performed on the two specimens printed with the L-PBF were successful performed. The exhibited properties were lower than what expected and quite statistically disperse, although they showed a similar elasticity modulus.

The reason of this could be explained by the defects generated during the printing of the samples, shown in the Figure 166.



Figure 166. Localization of a defect due to the printing process during the tensile test.

This created a preferential failure site, and this may have potentially started the failure process because both the prints failed in the same point, as shown in the Figure 167.



Figure 167. *L-PBF-printed specimens after the tensile test.*

This result confirms that we can proceed with the manufacturing of the tensile specimens with the titanium. The original geometry can be used because the strength sustained for this test is not so intense to lead to slip problems.

The physical characterization has remarked that the green parts are electrically insulants. The metal powder contained in the feedstock keeps its properties, thus in the case of AISI 316L that manifests a weak paramagnetic behaviour.

In the end, the economic evaluation has highlighted that the most relevant contribution of costs is associated to the material and to the D&S process. The economic impact of the D&S process, especially for titanium specimens, demonstrates that this step in the process is the most critical and needs improvement. It's to be noticed that the energy consumption was less impactful than expected.

Section 9

9. Conclusions

The goal of performing the tensile test with titanium feedstock haven't been achieved mainly because of the lack of material and poor knowledge of D&S process. Thus, a model to evaluate the shrinkage associated to the D&S has been developed.

Thanks to the ULTRAFUSE 316L, a routine has been established for the printing and testing of tensile test specimens.

The results of the tensile tests and the shrinkage measurement haven't been extracted and will be reported when available. This is due to the complexity of the debinding and sintering process that shows to be a great limit of this process.

The registered dimensional accuracy of the prints, both with the steel and the titanium feedstock, remarks that there is a better dimensional control on the z-direction compared to the dimensions achieved in the xy-plane.

With this study, a technical expertise of the Metal FDM has been developed resulting in a workflow to adjust the most relevant printing parameters with the final goal to print some specimen. The objective of this guide is to help new scientists who are approaching this technology to begin.

Before beginning to print, it's fundamental to calibrate the bed planarity. Usually, the procedure advised consists in setting the gap with a sheet but according to my experience, the best practice is the adjustment of the bed screws while printing test squares at the corners of the bed.

If a dual extruder system is adopted, it's preferable to adopt auto adjusting height systems because any minimum deviation may affect the result of the print. When auto-adjusting systems are not available, it's recommended to pick one extruder as reference and during the print of a trial square, regulate the height of the other extruder.

Companies that supply the solvent agent often specify materials that the solvent is able to be dissolve. It may happen that some material can suffer softening, thus is advised to check the response of the material to the solvent exposure in anyway.

Regarding the optimization of the printing parameters, it came out that in agreement with other studies reported in literature, the decrease of the layer height can enhance the quality of the surface, but it also dramatically increases the printing time. Again, parameters like the Extruder Multiplier and the Extrusion Temperature demonstrate to be intensely involved in the determination of the actual infilling of the print and the Overlapping proved to be very useful to enhance it by plugging the holes in the infill.

The use of the glue at first, and the use of the support material as a bed layer then, were convenient and quick manner to solve the problem related to the adhesion of the first layer. However, in the absence of time, other approaches that could be more effective have not been considered.

Given the influence of the Extruder Multiplier, the Extrusion temperature and the Layer height, future possible studies may aim to find the best combination of those parameters that can result in the best mechanical properties for medical applications.

Appendix A - Statistical instruments

In this appendix will be introduced all the statistical instruments employed in the current study.

Arithmetic Mean Value

The arithmetic mean value is “the quantity commonly called “the” mean or the average” [74]. Given a set of samples $\{x_i\}$, the arithmetic mean is represented by the Eq. (19).

$$\bar{x} = \frac{1}{N} \sum_{i=1}^N x_i \quad (19)$$

With:

- $\bar{x} \equiv$ Arithmetic Mean Value
- $N \equiv$ Sample size

Standard Deviation of the Sample

The standard deviation is an important information that shows how the evaluated property of the sample is homogeneous. This homogeneity is also called “data dispersion” and when data aren’t homogeneous, we can say that the sample is statistically disperse.

The theoretical definition of the standard deviation, reported in Eq. (20) for a discrete population, uses information about the whole population [75].

$$\sigma = \sqrt{\frac{1}{N} \sum_{i=1}^N (x_i - \bar{x})^2} \quad (20)$$

With:

- $\sigma \equiv$ Standard Deviation of the population
- $N \equiv$ Population size
- $x_i \equiv$ i-th value of the population
- $\bar{x} \equiv$ Arithmetic Mean Value of the population

In cases where the population is very numerous, this definition cannot be applied, but we can estimate this value anyway. The most common estimate used to average the standard deviation is presented in the Eq. (21) [75].

$$s = \sqrt{\frac{1}{N-1} \sum_{i=1}^N (x_i - \bar{x})^2} \quad (21)$$

With:

- $S \equiv$ Standard Deviation of the sample
- $N \equiv$ Specimen size

- $x_i \equiv$ i-th value of the specimen
- $\bar{x} \equiv$ Arithmetic Mean Value of the specimen

The importance of the standard deviation is the ability to detect the presence of parameters whose influence was underrated.

Coefficient of Determination R^2

The coefficient of determination or R^2 is a parameter that helps to declare how much a regression model defined as “ f ” matches with experimental data defined as “ y ” [76].

The mathematical definition of the coefficient of determination is given in the Eq. (22).

$$R^2 = 1 - \frac{\sum_{i=1}^N (y_i - f_i)^2}{\sum_{i=1}^N (y_i - \bar{y})^2} \quad (22)$$

With:

- $f_i \equiv$ value assigned by the regression model for the i-th point
- $y_i \equiv$ experimental value assigned at the i-th point
- $\bar{y} \equiv$ mean value of the experimental values

List of Figures

Figure 1. Stages of the slicing process [3].	10
Figure 2. Comparison of key metal additive manufacturing methods in terms of part size and costs. SLM, EBM, WAAM, MBJT, and MF3 [10].	11
Figure 3. Schematic diagram of hard tissues in human body [11].	12
Figure 4. Blistering effect on a specimen with a low pore control [15].	13
Figure 5. Scheme of the L-PBF process [5].	15
Figure 6. Scheme of the EB-PBF process [2].	16
Figure 7. Scheme of the L-DED process [2].	17
Figure 8. Scheme of the EB-DED process [2].	17
Figure 9. Scheme of the GMA-DED process [2].	18
Figure 10. Scheme of the: (a) GTA-DED process; (b) PA-DED process [2].	19
Figure 11. Schematic diagram of the DIWP process [17].	19
Figure 12. SSMED extrusion system [18].	20
Figure 13. Scheme of the BJ process [19].	20
Figure 14. Scheme of the LOM process [20].	21
Figure 15. MIM process [28].	25
Figure 16. Mixer used to produce the feedstock: (a) z sigma blade mixer and (b) zx sigma mixer-extruder [32].	27
Figure 17. Material Extrusion with Plunger-based [3].	28
Figure 18. Material extrusion with filament-based [3].	29
Figure 19. Material extrusion with screw-based [3].	31
Figure 20. Extrusion systems: (a) Bowden extrusion; (b) Direct extrusion [28].	32
Figure 21. Different way to apply the support material [38].	33
Figure 22. FDM parameters [39].	33
Figure 23. Influence parameter in the FDM process [40].	33
Figure 24. Process diagram for thermal debinding [42].	35
Figure 25. Solvent debinding process [42].	35
Figure 26. Catalytic debinding process [42].	36
Figure 27. Relative density in function of: (a) Temperature; (b) Time [45].	37
Figure 28. Effect of different debinding rates on SS 316 L samples sintered at 1360 °C for 6 h [45].	37
Figure 29. Necking process during the sintering [9].	38
Figure 30. ASA filament spool by EVO-tech [46].	41
Figure 31. Ultrafuse 316L filament spool [47].	42
Figure 32. Titanium 64-5 Filamet™ spool [50].	43
Figure 33. HIPS spool by EVO-Tech [46].	44
Figure 34. Replacement solvent tank.	44
Figure 35. FilaWarmer [54].	45
Figure 36. Setup of the FilaWarmer.	45
Figure 37. EVO-lizer 11 printer [55].	46
Figure 38. EVO-lizer 11 printer head with nozzles [57].	47
Figure 39. Comparison of wear resistance between a brass and a steel nozzle [58].	47
Figure 40. Housing for the filaments.	47
Figure 41. Simplify3D User Interface.	48
Figure 42. Instron 8801 system [60].	49

Figure 43. Front and back view of the digital calliper.	50
Figure 44. Front and back view of the micrometer.....	51
Figure 45. KEYENCE VR-5000 microscope [62].....	51
Figure 46. L-PBF printer model SLM 125 by SLM Solutions [63].	52
Figure 47. Geometrical features of the cross.....	54
Figure 48. Preview of the print features of the cross.	55
Figure 49. The result of the print, whose brim and raft were removed, compared with a coin.	55
Figure 50. Preview of the print features of the cube.	55
Figure 51. The cube and cross compared with a coin.....	56
Figure 52. First layer quality comparison and dimensional comparison with a coin.....	56
Figure 53. Result of the hotend offset calibration test with remarkable misalignment of the consecutive prints.....	57
Figure 54. (a) Console in the web interface, (b) console response to the “M218” command.	57
Figure 55. Result of the hotend offset adjustment with lower misalignment.....	58
Figure 56. Preview of the adhesion test with a cube of 20 mm side.	58
Figure 57. Adhesion test result: (a) dimensional comparison with a coin, (b) oozing defect on lateral surface, (c), top face, (d) bottom face.....	58
Figure 58. Dual towers test model [65].....	59
Figure 59. Dual towers test previews: (a) without raft structure, (b) with raft structure.	59
Figure 60. Results of the test: (a) comparison of the dual towers test, (b) first layer of the dual tower test with raft, (c) first layer of the dual tower raft without raft.....	60
Figure 61. DIN 50125 E-type tensile specimen sizes.	60
Figure 62. Tensile test specimen with default parameters: (a) bottom view, (b) top view.....	60
Figure 63. Bottom layer parameters optimization process: (a) all trials, (b) comparison between the first and last trial.....	61
Figure 64. Print parameters optimization process: (a) top view of the trial 11, (b) top view of the trial 19..	62
Figure 65. Failed trials in the parameter optimization process of specimens oriented on the z-axis.	63
Figure 66. Eleventh trial: (a) cross-section of the preview of the print, (b) result of the print.	63
Figure 67. Bottom layer temperature test layout.....	64
Figure 68. Result of the first print.	64
Figure 69. Second attempt of the temperature bottom layer calibration.....	64
Figure 70. Temperature calibration with cube models: (a) lateral view; (b) top view.	65
Figure 71. Tower test: (a) preview with all processes marked; (b) print result.	65
Figure 72. Dual tower test print result.....	66
Figure 73. Geometrical dimensions of tensile test specimen identified by letters [67].	67
Figure 74. Geometrical features of the tensile test specimen.....	68
Figure 75. Increase of gripping area highlighted in red.	69
Figure 76. First identification pin system.	71
Figure 77. Identification system in tensile test samples: (a) a view of the identification system, (b) meaning of each pin.	71
Figure 78. Example of identity assignation.	71
Figure 79. Orientation examined during the tensile test.....	72
Figure 80. Optimization trials of the non-rescaled geometry.....	73
Figure 81. Lateral surface of the fourth trial with visible stripes due to the deadhesion of the first layer....	73
Figure 82. Damage on the filament caused by the feeding system gear.....	73
Figure 83. Result of the print of the Z-oriented specimen.....	74
Figure 84. Failed print due to the bad planarity calibration.	74
Figure 85. Changeable texture of the brim structures due to the bad planarity calibration of the bed.	75

Figure 86. Print result after the planarity calibration: (a) lateral surface view; (b) warping effect due to the thermal shrinkage.....	75
Figure 87. Print result after the rescaling of the geometry: (a) lateral surface view; (b) warping effect due to the thermal shrinkage.	76
Figure 88. Print result after the removal of the glue from the bed: (a) lateral surface view; (b) warping effect due to the thermal shrinkage.	76
Figure 89. Preview of the print with demarcation of material deposited.	77
Figure 90. First layer with remarked raster air gaps.	77
Figure 91. Resulting print of the batch of tensile test specimens with the raft structure.....	78
Figure 92. View of the result of the print: (a) top and lateral surfaces; (b) piled specimens.	78
Figure 93. Warping effect of the raft structure due to the thermal shrinkage of the part material.	78
Figure 94. View of the bottom surface of the specimens with scars on the grips due to the part material nozzle.....	79
Figure 95. Preview of the print with the implementation of the lateral holder structures.....	79
Figure 96. Result of the print with lateral support structures.	80
Figure 97. Preview of the printing of the "Trial 9" specimen.....	80
Figure 98. Result of the printing of the "Trial 9" specimen.....	80
Figure 99. Retraction effect on the print: (a) retraction points in the preview mode; (b) retraction effect on the print.....	81
Figure 100. Preview of the "Trial 10" specimen whose the starting points of each layer are circled in red. .	81
Figure 101. Result of the printing of the "Trial 10" specimen.....	82
Figure 102. Bad quality caused by the retraction: (a) lateral edge of the grip; (b) corner of the grip.	82
Figure 103. Lateral view of the "Trial 10" specimen.	82
Figure 104. Grip of the "Trial 11" specimen with focus on the lateral surface.....	83
Figure 105. Preview of the "Trial 12" specimen whose the starting points of each layer are circled in red. .	83
Figure 106. Top view of the "Trial 12" specimen.	83
Figure 107. Detail view of the clamp of the specimen "Trial 12".....	84
Figure 108. Preview of the "Trial 13" specimen.....	84
Figure 109. Top view of the "Trial 12" specimen.	84
Figure 110. Detail view of the clamp of the specimen "Trial 13".....	85
Figure 111. Spacing of components: (a) preview of the print of two components too close; (b) ineffective brim structure.....	85
Figure 112. Print failure due to the setting a shared bed layer.	86
Figure 113. Mono-process printing strategy sequence.	86
Figure 114. Independent processes strategy sequence.....	87
Figure 115. Bed layer peeling: (a) during the procedure; (b) after the procedure.	87
Figure 116. Brim removal process.....	87
Figure 117. Identification assignation process: (a) during the removal of pins; (b) after the process.	88
Figure 118. Geometrical features of the identification system of the Specimen Type B.	90
Figure 119. Value associated to every pins.	90
Figure 120. Layout of specimens on the printing bed.....	90
Figure 121. Ineffective use of the skirt (a) and brim (b).....	91
Figure 122. Effect of the oozing shield on the print by setting single-process.	92
Figure 123. Depiction of (a) use of extruder and (b) process arrangement.	92
Figure 124. First trial of optimization of the A-type specimen.	93
Figure 125. Second trial of optimization of the A-type specimen.	93
Figure 126. Third trial of optimization of the A-type specimen.....	94
Figure 127. Fourth trial of optimization of the A-type specimen.	94
Figure 128. Extrusion width effect: (a) Auto width; (b) 0,3 mm manual setting.	95

Figure 129. Fifth trial of optimization of the A-type specimen.....	95
Figure 130. Sixth trial of optimization of the A-type specimen: (a) Top View; (b) Lateral View.....	96
Figure 131. Seventh trial of optimization of the A-type specimen: (a) Top View; (b) Lateral View.....	96
Figure 132. Eighth trial of optimization of the A-type specimen.....	97
Figure 133. Ninth trial of optimization of the A-type specimen.....	97
Figure 134. Tenth trial of optimization of the A-type specimen.....	97
Figure 135. Eleventh trial of optimization of the A-type specimen.....	98
Figure 136. Twelfth trial of optimization of the A-type specimen: (a) Top View; (b) Lateral View.....	98
Figure 137. Thirteenth trial of optimization of the A-type specimen: (a) Top View; (b) Lateral View; (c) Behind View.....	99
Figure 138. First trial of optimization of the B-type specimen: (a) Top View; (b) Behind View; (c) Lateral View.....	100
Figure 139. First trial of optimization of the C-type specimen: (a) Top View; (b) Lateral View; (c) Behind View.....	100
Figure 140. Preview of the first layout tried to print A-type specimens.....	101
Figure 141. Bad layer strategy: (a) failed print; (b) grinded filament.....	101
Figure 142. Preview of the second layout tried to print A-type specimens.....	101
Figure 143. Batch printing: (a) A-type specimens; (b) B-type specimens.....	102
Figure 144. Failed print of the batch of C-type specimen.....	102
Figure 145. Batch printing of C-type specimens.....	103
Figure 146. HIPS removal process: (a) batch status after the immersion; (b) batch status after 4 hours in the tank.....	103
Figure 147. Drying process after the HIPS removal.....	103
Figure 148. C-Type specimens after the pins removal process.....	104
Figure 149. A print run that shows the effect of a non-levelled bed: (a) local position on the printing bad, (b) result of the print.....	105
Figure 150. Bed adjustment procedure: (a) a view of the gcode file performed, (b) a view of the bottom part of the bed with adjustment screws.....	105
Figure 151. Square printed during the adjustment of the plate.....	106
Figure 152. Effect of the gap between the nozzle tip and the bed during the deposition of the first layer.....	106
Figure 153. ASA tensile test specimen exposed to the d-limonene for 48 hours.....	107
Figure 154. Samples exposed for a long period to the solvent agent: (a) ULTRAFUSE 316L, (b) Titanium 64-5 Filamet.....	107
Figure 155. Auxiliary structures applied on a cube: (a) brim and (b) skirt.....	108
Figure 156. Detail picture of the nozzle unit with fixing screws circled in red [46].....	108
Figure 157. Groove due to a bad equalization of the nozzles position.....	109
Figure 158. Gap-adjuster device: (a) CAD drawing, (b) Installation on the nozzle unit, (c) Installation on the carrier extruder.....	109
Figure 159. Energy cost trend in time domain: F1(Monday-Friday 8:00-19:00); F2(Monday-Friday 7:00-8:00); F3(Monday-Saturday 23:00-7:00, Sunday and Holidays).....	114
Figure 160. Spots of the acquisition of the cross section.....	118
Figure 161. Stress-strain diagram of the two tensile specimens printed via L-PBF.....	121
Figure 162. Pie chart of the total cost associated to production of the batch of specimens Type-A.....	122
Figure 163. Pie chart of the total cost associated to production of the batch of specimens Type-B.....	122
Figure 164. Pie chart of the total cost associated to production of the batch of specimens Type-C.....	123
Figure 165. Pie charts of cost contributions associated to the production of the tensile specimens.....	123
Figure 166. Localization of a defect due to the printing process during the tensile test.....	124
Figure 167. L-PBF-printed specimens after the tensile test.....	125

List of Tables

Table 1. Overview of powder characterisation techniques commonly used in AM [31].	26
Table 2. Examples of binder system compositions used in PIM [34].	29
Table 3. Examples of binder system compositions used in filament shaped feedstocks [29][34].	30
Table 4. Examples of binder system compositions used in pellet feedstocks [29] [34].	31
Table 5. Main parameters of influence in every step of the metal FDM process [9].	34
Table 6. Mechanical properties of ASA material by EVO-tech [46].	41
Table 7. Recommended ASA print setting [46].	42
Table 8. Recommended 3D-Print processing parameters [48] [49].	42
Table 9. Mechanical properties of the ULTRAFUSE 316L [48].	43
Table 10. Printing and sintering parameters for Titanium 64-5 Filamet™ recommended by The Virtual Foundry [51].	43
Table 11. Technical data of the EVO lizer 11 [56].	46
Table 12. Instron 8801 features [60].	49
Table 13. 2743-401 grips features [61].	50
Table 14. Technical specifications of the SLM 125 printer [64].	52
Table 15. Changed print parameters to maximization of the bottom layer infill.	62
Table 16. Changed print parameters to maximization of the top layer quality surface.	62
Table 17. ASTM E8/E8M-22 constraints.	67
Table 18. ISO 6892-1 Annex B constraints.	68
Table 19. List of all considered constraints.	68
Table 20. Identification of all ULTRAFUSE 316L samples.	72
Table 21. Parameters involved in the optimization process of the non-rescaled geometry.	74
Table 22. Geometrical features of shrinkage specimens.	88
Table 23. Comparison of material required with different DoE.	89
Table 24. Raft settings.	91
Table 25. Changing of the printing parameters to solve the problem related to the nozzle clogging.	102
Table 26. Data regarding the print of the titanium feedstock.	112
Table 27. Data regarding the print of the steel tensile test specimens on the XY plane.	113
Table 28. Data regarding the print of the steel tensile test specimens on the ZX plane.	113
Table 29. Electric consumption data.	115
Table 30. Data regarding the solvent agent employed.	116
Table 31. Debinding and sintering information.	116
Table 32. X-axes oriented specimen measurements.	118
Table 33. Y-axes oriented specimen measurements.	119
Table 34. Z-axes oriented specimen measurements	119
Table 35. Comparison of actual values with theoretical values.	120
Table 36. Dimensions of the shrinkage specimens made with the Filamet 64-5.	120
Table 37. Ultimate Tensile Test (UTS) and estimated Elasticity Module (E) with relative coefficient of determination of the two tensile specimens.	121

Bibliography

- [1] D. Godec, S. Cano, C. Holzer, and J. Gonzalez-Gutierrez, "materials Optimization of the 3D Printing Parameters for Tensile Properties of Specimens Produced by Fused Filament Fabrication of 17-4PH Stainless Steel", doi: 10.3390/ma13030774.
- [2] M. Harris, J. Potgieter, R. Archer, and K. M. Arif, "materials Effect of Material and Process Specific Factors on the Strength of Printed Parts in Fused Filament Fabrication: A Review of Recent Developments," 2019, doi: 10.3390/ma12101664.
- [3] A. I. Nurhuda, S. Supriadi, Y. Whulanza, and A. S. Saragih, "Additive manufacturing of metallic based on extrusion process: A review," *J. Manuf. Process.*, vol. 66, pp. 228–237, Jun. 2021, doi: 10.1016/J.JMAPRO.2021.04.018.
- [4] B. A. Praveena, N. Lokesh, A. Buradi, N. Santhosh, B. L. Praveena, and R. Vignesh, "A comprehensive review of emerging additive manufacturing (3D printing technology): Methods, materials, applications, challenges, trends and future potential," *Mater. Today Proc.*, vol. 52, pp. 1309–1313, Jan. 2022, doi: 10.1016/J.MATPR.2021.11.059.
- [5] J. P. M. Pragana, R. F. V. Sampaio, I. M. F. Bragança, C. M. A. Silva, and P. A. F. Martins, "Hybrid metal additive manufacturing: A state-of-the-art review," *Adv. Ind. Manuf. Eng.*, vol. 2, p. 100032, May 2021, doi: 10.1016/J.AIME.2021.100032.
- [6] J. Zhang, B. Song, Q. Wei, D. Bourell, and Y. Shi, "A review of selective laser melting of aluminum alloys: Processing, microstructure, property and developing trends," *J. Mater. Sci. Technol.*, vol. 35, no. 2, pp. 270–284, Feb. 2019, doi: 10.1016/J.JMST.2018.09.004.
- [7] A. Salmi, F. Calignano, M. Galati, and E. Atzeni, "An integrated design methodology for components produced by laser powder bed fusion (L-PBF) process," <https://doi.org/10.1080/17452759.2018.1442229>, vol. 13, no. 3, pp. 191–202, Jul. 2018, doi: 10.1080/17452759.2018.1442229.
- [8] L. Papadakis, D. Chantzis, and K. Salonitis, "On the energy efficiency of pre-heating methods in SLM/SLS processes," *Int. J. Adv. Manuf. Technol.*, vol. 95, no. 1–4, pp. 1325–1338, Mar. 2018, doi: 10.1007/S00170-017-1287-9/METRICS.
- [9] H. Ramazani and A. Kami, "Metal FDM, a new extrusion-based additive manufacturing technology for manufacturing of metallic parts: a review," vol. 7, pp. 609–626, 2022, doi: 10.1007/s40964-021-00250-x.
- [10] Y. Thompson *et al.*, "Fused Filament Fabrication-Based Additive Manufacturing of Commercially Pure Titanium," *Adv. Eng. Mater.*, vol. 23, no. 12, Dec. 2021, doi: 10.1002/ADEM.202100380.
- [11] X. Liu, P. K. Chu, and C. Ding, "Surface modification of titanium, titanium alloys, and related materials for biomedical applications," *Mater. Sci. Eng. R Reports*, vol. 47, no. 3–4, pp. 49–121, Dec. 2004, doi: 10.1016/J.MSER.2004.11.001.
- [12] P. Singh, V. K. Balla, A. Tofangchi, S. V. Atre, and K. H. Kate, "Printability studies of Ti-6Al-4V by metal fused filament fabrication (MF3)," *Int. J. Refract. Met. Hard Mater.*, vol. 91, p. 105249, Sep. 2020, doi: 10.1016/J.IJRMHM.2020.105249.
- [13] Y. Zhang, S. Bai, M. Riede, E. Garratt, and A. Roch, "A comprehensive study on fused filament fabrication of Ti-6Al-4V structures," *Addit. Manuf.*, vol. 34, p. 101256, Aug. 2020, doi: 10.1016/J.ADDMA.2020.101256.

- [14] "Materiali di stampa 3D | Markforged." <https://markforged.com/it/materials> (accessed Apr. 01, 2023).
- [15] Y. Thompson, J. Gonzalez-Gutierrez, C. Kukla, and P. Felfer, "Fused filament fabrication, debinding and sintering as a low cost additive manufacturing method of 316L stainless steel," *Addit. Manuf.*, vol. 30, 2019, doi: 10.1016/j.addma.2019.100861.
- [16] M. Yakout, M. A. Elbestawi, and S. C. Veldhuis, "A Review of Metal Additive Manufacturing Technologies," *Solid State Phenom.*, vol. 278, pp. 1–14, 2018, doi: 10.4028/WWW.SCIENTIFIC.NET/SSP.278.1.
- [17] H. Elsayed *et al.*, "Direct ink writing of porous titanium (Ti6Al4V) lattice structures," *Mater. Sci. Eng. C*, vol. 103, p. 109794, Oct. 2019, doi: 10.1016/J.MSEC.2019.109794.
- [18] P. Mendez, C. Rice, and S. Brown, "Comments on 'Solid freeform fabrication by extrusion and deposition of semi-solid alloys'".
- [19] "Binder Jetting | Additive Manufacturing Research Group | Loughborough University." <https://www.lboro.ac.uk/research/amrg/about/the7categoriesofadditivemanufacturing/binderjetting/> (accessed Apr. 02, 2023).
- [20] A. Razavykia, E. Brusa, C. Delprete, and R. Yavari, "An overview of additive manufacturing technologies-A review to technical synthesis in numerical study of selective laser melting," *Materials (Basel)*, vol. 13, no. 17, Sep. 2020, doi: 10.3390/MA13173895.
- [21] M. Q. Shaikh *et al.*, "Investigation of patient-specific maxillofacial implant prototype development by metal fused filament fabrication (Mf3) of ti-6al-4v," *Dent. J.*, vol. 9, no. 10, 2021, doi: 10.3390/dj9100109.
- [22] C. Kukla, J. Gonzalez-Gutierrez, S. Hampel, C. Burkhardt, and C. Holzer, "The SDS process: A viable way for the production of metal parts." Apr. 24, 2017. Accessed: Dec. 22, 2022. [Online]. Available: [https://pure.unileoben.ac.at/portal/en/publications/the-sds-process-a-viable-way-for-the-production-of-metal-parts\(5c3bf547-8859-4a29-ada8-4cacb9928c4b\)/export.html](https://pure.unileoben.ac.at/portal/en/publications/the-sds-process-a-viable-way-for-the-production-of-metal-parts(5c3bf547-8859-4a29-ada8-4cacb9928c4b)/export.html)
- [23] "(PDF) Preparation and Properties of Extrusion-Based 3D-Printed Hardmetal and Cermet Parts." https://www.researchgate.net/publication/328486512_Preparation_and_Properties_of_Extrusion-Based_3D-Printed_Hardmetal_and_Cermet_Parts (accessed Dec. 22, 2022).
- [24] A. Watson, J. Belding, and B. D. Ellis, "Characterization of 17-4 PH Processed via Bound Metal Deposition (BMD)," *Miner. Met. Mater. Ser.*, pp. 205–216, 2020, doi: 10.1007/978-3-030-36296-6_19.
- [25] M. Galati and P. Minetola, "materials Analysis of Density, Roughness, and Accuracy of the Atomic Diffusion Additive Manufacturing (ADAM) Process for Metal Parts", doi: 10.3390/ma12244122.
- [26] T. Kurose *et al.*, "Influence of the Layer Directions on the Properties of 316L Stainless Steel Parts Fabricated through Fused Deposition of Metals," *Mater. 2020, Vol. 13, Page 2493*, vol. 13, no. 11, p. 2493, May 2020, doi: 10.3390/MA13112493.
- [27] P. Singh, V. K. Balla, A. Gokce, S. V. Atre, and K. H. Kate, "Additive manufacturing of Ti-6Al-4V alloy by metal fused filament fabrication (MF3): producing parts comparable to that of metal injection molding," *Prog. Addit. Manuf.*, vol. 6, no. 4, 2021, doi: 10.1007/s40964-021-00167-5.
- [28] V. E. Kuznetsov, A. G. Tavitov, O. D. Urzhumtsev, M. V. Mikhailin, and A. I. Moiseev, "Hardware Factors Influencing Strength of Parts Obtained by Fused Filament Fabrication," *Polym. 2019, Vol. 11, Page 1870*, vol. 11, no. 11, p. 1870, Nov. 2019, doi: 10.3390/POLYM11111870.
- [29] A. Y. Korotchenko, D. E. Khilkov, M. V. Tverskoy, and A. A. Khilkova, "Use of additive technologies for

metal injection molding," *Eng. Solid Mech.*, vol. 8, no. 2, pp. 143–150, 2020, doi: 10.5267/J.ESM.2019.10.001.

- [30] G. Wu, N. A. Langrana, R. Sadanji, and S. Danforth, "Solid freeform fabrication of metal components using fused deposition of metals," *Mater. Des.*, vol. 23, no. 1, pp. 97–105, Feb. 2002, doi: 10.1016/S0261-3069(01)00079-6.
- [31] A. T. Sutton, C. S. Kriewall, M. C. Leu, and J. W. Newkirk, "Powder characterisation techniques and effects of powder characteristics on part properties in powder-bed fusion processes," <http://dx.doi.org/10.1080/17452759.2016.1250605>, vol. 12, no. 1, pp. 3–29, Jan. 2016, doi: 10.1080/17452759.2016.1250605.
- [32] K. Rane and M. Strano, "A comprehensive review of extrusion-based additive manufacturing processes for rapid production of metallic and ceramic parts," *Adv. Manuf.*, vol. 7, no. 2, pp. 155–173, Jun. 2019, doi: 10.1007/S40436-019-00253-6/FIGURES/15.
- [33] M. K. Agarwala, R. Van Weeren, A. Bandyopadhyay, A. Safari, S. C. Danforth, and W. R. Priedeman, "Filament Feed Materials for Fused Deposition Processing of Ceramics and Metals".
- [34] J. Gonzalez-Gutierrez, S. Cano, S. Schuschnigg, C. Kukla, J. Sapkota, and C. Holzer, "Additive Manufacturing of Metallic and Ceramic Components by the Material Extrusion of Highly-Filled Polymers: A Review and Future Perspectives," *Mater. (Basel, Switzerland)*, vol. 11, no. 5, May 2018, doi: 10.3390/MA11050840.
- [35] Y. Tlegenov, G. S. Hong, and W. F. Lu, "Nozzle condition monitoring in 3D printing," *Robot. Comput. Integr. Manuf.*, vol. 54, pp. 45–55, Dec. 2018, doi: 10.1016/J.RCIM.2018.05.010.
- [36] J. Go, S. N. Schiffres, A. G. Stevens, and A. J. Hart, "Rate limits of additive manufacturing by fused filament fabrication and guidelines for high-throughput system design," *Addit. Manuf.*, vol. 16, pp. 1–11, Aug. 2017, doi: 10.1016/J.ADDMA.2017.03.007.
- [37] J. Hiemenz and I. Stratasys, "3D PRINTING WITH FDM: How it Works".
- [38] K. Rajaguru, T. Karthikeyan, and V. Vijayan, "Additive manufacturing – State of art," *Mater. Today Proc.*, vol. 21, pp. 628–633, Jan. 2020, doi: 10.1016/J.MATPR.2019.06.728.
- [39] M. S. Hossain, D. Espalin, J. Ramos, M. Perez, and R. Wicker, "Improved Mechanical Properties of Fused Deposition Modeling-Manufactured Parts Through Build Parameter Modifications," *J. Manuf. Sci. Eng. Trans. ASME*, vol. 136, no. 6, Dec. 2014, doi: 10.1115/1.4028538/377600.
- [40] A. Dey and N. Yodo, "Manufacturing and Materials Processing A Systematic Survey of FDM Process Parameter Optimization and Their Influence on Part Characteristics," 2019, doi: 10.3390/jmmp3030064.
- [41] R. K. Enneti, S. J. Park, R. M. German, and S. V. Atre, "Review: Thermal Debinding Process in Particulate Materials Processing," <https://doi.org/10.1080/10426914.2011.560233>, vol. 27, no. 2, pp. 103–118, Feb. 2012, doi: 10.1080/10426914.2011.560233.
- [42] Z. Lotfizarei, A. Mostafapour, A. Barari, A. Jalili, and A. E. Patterson, "Overview of debinding methods for parts manufactured using powder material extrusion," *Addit. Manuf.*, vol. 61, p. 103335, Jan. 2023, doi: 10.1016/J.ADDMA.2022.103335.
- [43] H. Li, Y. Liu, Y. Liu, K. Hu, Z. Lu, and J. Liang, "Effects of solvent debinding on the microstructure and properties of 3D-printed alumina ceramics," *ACS Omega*, vol. 5, no. 42, pp. 27455–27462, Oct. 2020, doi: 10.1021/ACSOMEGA.0C03944/ASSET/IMAGES/LARGE/AOOC03944_0009.JPEG.
- [44] T. Rosnitschek, J. Glamsch, C. Lange, B. Alber-Laukant, and F. Rieg, "An Automated Open-Source Approach for Debinding Simulation in Metal Extrusion Additive Manufacturing," *Des. 2021, Vol. 5*,

- [45] M. Mousapour, M. Salmi, L. Klemettinen, and J. Partanen, "Feasibility study of producing multi-metal parts by Fused Filament Fabrication (FFF) technique," *J. Manuf. Process.*, vol. 67, pp. 438–446, 2021, doi: 10.1016/j.jmapro.2021.05.021.
- [46] "Datenblätter - EVO-tech 3D-Drucker | EVO-tech GmbH." <https://www.evo-tech.eu/kunden-area/material-datenblaetter/> (accessed Jan. 03, 2023).
- [47] "BASF Ultrafuse 316L | 3Kg." <https://www.crea3d.com/it/basf/643-736-basf-ultrafuse-316l-3kg.html> (accessed Jan. 03, 2023).
- [48] "BASF 3D Printing Solutions BV sales@basf-3dps.com www.forward-am.com General information", Accessed: Jan. 22, 2023. [Online]. Available: www.forward-am.com
- [49] "Ultrafuse 316L User Guidelines for 3D Printing Metal Parts", Accessed: Mar. 01, 2023. [Online]. Available: www.forward-am.com
- [50] "Titanium 64-5 Filamet™ | The Virtual Foundry." <https://shop.thevirtualfoundry.com/en-it/products/titanium-64-5-filamet?variant=29450259529811> (accessed Jan. 03, 2023).
- [51] "TDS - The Virtual Foundry, inc." <https://thevirtualfoundry.com/tds/> (accessed Jan. 23, 2023).
- [52] "Products - The Virtual Foundry, inc." <https://thevirtualfoundry.com/products/> (accessed Jan. 23, 2023).
- [53] "(R)-(+)-Limonene, 96%, Thermo Scientific Chemicals | Fisher Scientific." <https://www.fishersci.it/shop/products/r-limonene-96-thermo-scientific/11301697> (accessed Feb. 11, 2023).
- [54] "Filawarmer | The Virtual Foundry." <https://shop.thevirtualfoundry.com/products/filawarmer?variant=12228959993939> (accessed Jan. 04, 2023).
- [55] "3d Printer El-11 - Evolizer 3d Drucker Transparent PNG - 450x559 - Free Download on NicePNG." https://www.nicepng.com/ourpic/u2w7t4w7a9y3r5i1_3d-printer-el-11-evolizer-3d-drucker/ (accessed Jan. 02, 2023).
- [56] "Odo." <https://www.evo-tech.eu/document/share/53/a534a276-3bcb-45e5-8107-033c54052765> (accessed Mar. 21, 2023).
- [57] "Innovations in binder-based AM and advances in conformal cooling." <https://www.metal-am.com/articles/innovations-in-binder-based-3d-printing-and-advances-in-conformal-cooling/> (accessed Jan. 04, 2023).
- [58] "Ultrafuse 316L Video Tutorial Ultrafuse 316L User Guidelines for 3D Printing Metal Parts", Accessed: Jan. 31, 2023. [Online]. Available: www.basf-3dps.com
- [59] "Simplify - EVO-tech 3D-Drucker | EVO-tech GmbH." <https://www.evo-tech.eu/kunden-area/simplify/> (accessed Jan. 02, 2023).
- [60] "8801 SERVOHYDRAULIC FATIGUE TESTING SYSTEM Up to 100 kN," 2022, Accessed: Feb. 18, 2023. [Online]. Available: www.instron.com
- [61] Instron, "100 kN Universal Hydraulic Wedge Action Grips," 2013, Accessed: Feb. 24, 2023. [Online]. Available: www.instron.com
- [62] "Instant 3D Measurement Over a Wide Area | Wide-Area 3D Measurement System VR-5000 | KEYENCE America." <https://www.keyence.com/ss/products/measure-sys/vr/> (accessed Feb. 28, 2023).

- [63] "SLM SOLUTIONS - SLM 125 | Overmach." <https://www.overmach.it/prodotti/slm-solutions-slm-125/> (accessed Mar. 08, 2023).
- [64] "EQUIPMENT | High Power Laser in a Compact Footprint for Flexible Manufacturing Versatile Selective Laser Melting Selective Laser Melting Machine".
- [65] "Retraction Dual Tower Test by MakerBlock - Thingiverse." <https://www.thingiverse.com/thing:3340223> (accessed Feb. 20, 2023).
- [66] E. C. Harmanşah, E. Üniversitesi, Y. Havacılık, and M. Yüksekokulu, "HAVACILIK TEKNOLOJİSİ VE UYGULAMALARI KİTABI".
- [67] "Standard Test Methods for Tension Testing of Metallic Materials." https://www.astm.org/e0008_e0008m-22.html (accessed Jan. 07, 2023).
- [68] "ISO - ISO 6892-1:2019 - Metallic materials — Tensile testing — Part 1: Method of test at room temperature." <https://www.iso.org/standard/78322.html> (accessed Jan. 05, 2023).
- [69] P. J. Morais *et al.*, "Characterisation of a High-Performance Al–Zn–Mg–Cu Alloy Designed for Wire Arc Additive Manufacturing," *Mater. 2020, Vol. 13, Page 1610*, vol. 13, no. 7, p. 1610, Apr. 2020, doi: 10.3390/MA13071610.
- [70] "Metal filaments: Filamet and Ultrafuse." https://filament2print.com/gb/blog/119_metal-filaments-filamet-and-ultrafuse.html (accessed Jan. 31, 2023).
- [71] "D-Limonene | Filament2Print." <https://filament2print.com/gb/post-processing/652-d-limonene.html> (accessed Mar. 21, 2023).
- [72] "BASF debinding & sintering voucher (1 kg) | Filament2Print." <https://filament2print.com/gb/others/1304-bono-sinterizado-basf.html> (accessed Apr. 06, 2023).
- [73] "Nanoe Sintering Coupon | Filament2Print." https://filament2print.com/gb/post-processing/1667-nanoe-sintering-coupon.html#/1065-material-zetamix_h13 (accessed Apr. 06, 2023).
- [74] E. W. Weisstein, "Arithmetic Mean", Accessed: Apr. 02, 2023. [Online]. Available: <https://mathworld.wolfram.com/>
- [75] E. W. Weisstein, "Standard Deviation", Accessed: Apr. 03, 2023. [Online]. Available: <https://mathworld.wolfram.com/>
- [76] "Coefficient of determination | Interpretation & Equation | Britannica." <https://www.britannica.com/science/coefficient-of-determination> (accessed Apr. 06, 2023).

Acknowledgements

La realizzazione di questo studio non sarebbe mai stata possibile grazie alla supervisione del Prof. Giorgio De Pasquale, che mi ha introdotto a questo progetto con entusiasmo e guidato attraverso tutte le fasi dell'attività con grande attenzione, pazienza e interesse.

Un altro doveroso ringraziamento va al Prof. Francesco Moscato, Ewald Unger ed a tutta la squadra di ragazzi, o "shark tank guys and baby shark tank guys", che mi hanno offerto una calorosa accoglienza e prestato supporto di ogni tipo nel Center for Medical Physics and Biomedical Engineering della Medical University of Vienna.

I ringraziamenti più sentiti, quelli che aspettavo di fare da quando ho varcato le porte del Politecnico vanno alla mia famiglia in quanto i riconoscimenti conseguiti e la persona che sono oggi sono merito loro. Loro che mi hanno dato supporto di ogni tipo ed hanno creduto in me sin dall'inizio, prima ancora che fossi io a farlo.

A Sebastiano Ursi, il mio papà, la persona da cui ho preso tantissimo e a cui devo molto di più. A lui devo la perseveranza, la curiosità e l'ambizione trasmesse che hanno portato a raggiungere questo importante obiettivo.

A Rosa Miani, la mia mamma, che è sempre stata una fonte inesauribile d'affetto e che mi ha sempre ricordato, anche dopo lunghi periodi di lontananza, il significato della parola "casa".

A Giuliana Ursi, la sorella che mi ha insegnato che ci sono tanti modi di voler voglio bene ad una persona, ognuno con il suo fascino caratteristico.

A Marianna Ursi, la sorella che è stata per un modello da seguire sin da piccolo e che con l'aiuto di Nicola Cirulli lo sarà sicuramente anche per la piccola Giorgia.

Un ringraziamento di cuore va ad Emanuela Regano, la mia Emy, la persona preziosa che è stata al mio fianco da prima dell'inizio di questa avventura. A lei dico grazie perché mi ha fatto capire che nella vita bisogna lottare per le cose più belle e che alla fine l'impegno darà i suoi frutti. La ringrazio per essere sempre stata presente per me, anche con un semplice messaggio. Infine, grazie perché lei è la persona che è stata forte nei giorni di pioggia e a cui voglio portare mille giorni di sole.

Questo ringraziamento infine va ad un'altra famiglia, quella che ho scelto io: la famiglia dei miei amici.

Va a Riccardo Loconte, il doctor, un amico che stimo tantissimo e che c'è sempre stato per un ultimo saluto, spesso dato prima di salire sull'autobus in partenza per Torino. Oltre a lui ci sono altri super, anzi mitici amici della scuola elementare! Sono Luca Porro, Rosanna Apruzzese e Maria Stoykina, i "ragazzi della mitica H" che, ogni volta che ho modo di passarci del tempo assieme, tra una memoria perduta e una risata su qualche gossip riguardante quel periodo, mi hanno sempre aiutato a tenere a mente chi sono e chi voglio essere.

Va ad Antonio Pilato, detto Ponzietto, la persona con cui ho passato la gran parte della adolescenza e la cui amicizia e stima per lui sono inossidabili al tempo e alla distanza. Sicuramente una parte della persona che sono oggi è merito suo (tranne che per il calcio balilla).

Va ad Antonio Inchingolo, detto Inc , con cui ho un legame speciale paragonabile a quello che si ha con un fratello. Anche con lui l'amicizia sviluppata è inossidabile e anzi, sembra rafforzarsi con la distanza ed il tempo.

Va ai "Grigliavengers", il gruppo di amici strepitosi conosciuti durante il percorso e composto da Pierpaolo, Emanuele il colonnello, Savino, Tonio, Mauro e Alessia, Barbara, Agata e Graziana. Ogni volta che sono tornato nella mia città, sono stati sempre capaci di regalarmi allegria e spensieratezza liberandomi dalle incertezze e dalle paure che a volte mi attanagliano.

Va a Valentino e Pietro, i coinquilini d'oro che mi hanno fatto compagnia in questi ultimi anni d'università. Con loro ho condiviso tanto tempo e grazie a loro le ore di studio sono sempre state più leggere. Mi hanno trasmesso tanto affetto e soprattutto tanta allegria.

Un ringraziamento finale va infine a tutti i fantastici amici conosciuti a Torino tra i banchi di università, a Francesco, Pierpaolo, Andrea, Erica e Clara che mi hanno regalato tantissime emozioni e avventure ma allo stesso tempo anche una enorme crescita personale. Grazie a loro la mia esperienza universitaria è stata stupenda, cosa per cui non li ringrazierò mai abbastanza.

Colgo questo momento per chiedere anche scusa a tutti quanti per tutte le volte in cui la necessità di studiare mi ha richiesto di sacrificare tempo prezioso da spendere con voi. Quel tempo rubato si è trasformato in questo grande risultato che ora voglio dedicare a tutti voi, voi a cui devo la persona che sono oggi!

Purtroppo, non ho abbastanza spazio per citare tutte le persone che ho incontrato durante il mio percorso e che vorrei ringraziare, anche per semplici e piccoli gesti che mi hanno aiutato nel cammino. Il cammino però non è terminato, anzi prosegue con nuovi obiettivi e ambizioni e per questo voglio concludere con

Un grazie dal profondo del mio cuore a chiunque in me abbia mai creduto, crede o crederà